Varying shading in vehicle-integrated PV for different public transport case studies

A simulation-based model

Sanne van den Broek

Delft University of Technology

TU Delft

Varying shading in vehicle-integrated PV for different public transport case studies

A simulation-based model

by

Sanne van den Broek

to obtain the degree of Master of Science
at the Delft University of Technology,
to be defended publicly on Wednesday November 22, 2023 at 3:00 PM.

Student number:	4580257	
Degree:	MSc Sustainable Energy Technology	
Track:	Autonomous Systems	
Faculty:	EEMCS	
Project duration:	April 1, 2023 – November 22, 2023	
Thesis committee:	Prof. dr. Arthur (A.W.) Weeber,	[TU Delft daily thesis supervisor]
	Dr. ir. Rudi (R.) Santbergen,	[TU Delft committee member]
	Dr. Kees (C.) Maat,	[TU Delft committee member]
	Dr. Lenneke (L.H.) Slooff-Hoek,	[TNO external expert]

Cover: Sono Motors image source [1]
An electronic version of this thesis is available at http://repository.tudelft.nl/

TU Delft Delft University of Technology

PVMD

TNO innovation for life

Preface

This thesis concludes my master's program in Sustainable Energy Technology at Delft University of Technology. I have gained new insights into the solar mobility industry, conducted (literature) research and, most importantly, experienced the learning process that comes with a thesis as a whole. It turned out to be more than just a cliché, as the hours, days, and months of research, (re)writing, (bi-)weekly meetings, discussions with external researchers, facing challenges, or gaining new perspectives have indeed translated into valuable learning experiences. The result is a piece of work that I am very proud of.

A special thanks goes to my supervisor, Arthur Weeber. Your continuous guidance, motivation, speedy responses to my e-mails, and effective meetings were invaluable. I value our conversations and enjoyed gaining new insights into the solar industry through your expertise. Your enthusiasm about solar-related topics or personal interests like running and cycling has been very much appreciated. Secondly, I would like to thank Rudi Santbergen and Kees Maat for insightful meetings and sharing your expertise on solar modelling and topographical maps.

Additionally, I want to express my appreciation to TNO for granting me the opportunity to conduct this thesis with TNO. Nine months ago, I approached Lenneke Slooff-Hoek with a question for researching shading in vehicle-integrated PV, driven by my passion for mobility and a keen interest in solar energy. I believe that, as a result of the last couple of months, my research has provided valuable insights. I especially want to thank Lenneke for her support, and her effective guidance during my research. Furthermore, I would like to thank Anna Carr and Ashish Binani, as you both took the time to provide advice and modelling support during my thesis.

Furthermore, I would like to thank external researchers and experts in the field who have taken the time to provide me with a more in-depth understanding of their research studies. Sharing their knowledge has boosted my enthusiasm for this thesis and project. A special thanks to Hesan Ziar, Pirouz Nourian, Kenji Araki, Mohanrajan Rajendran, Carlotta Ferri, Jieun Baek, and others who provided information through their papers and expertise.

Moreover, I want to thank all my friends I met during my academic career. They have made my years in Delft unforgettable and always supported me along the way. I especially want to thank my dad and friends, who have proofread my thesis and provided valuable feedback on my work. This gave me constructive perspectives and good discussions on relevant topics, which I highly appreciate. Most importantly, I want to express my gratitude to my parents and sister for their unconditional support throughout my studies.

For now, I hope you enjoy reading this thesis and that the concept of vehicle-integrated PV brings the same excitement as it does to me!

Sanne van den Broek
Amsterdam, November 2023

Abstract

With advancements in the photovoltaics (PV) market, involving increased PV module efficiency and reduced costs, the logical progression is the integration of PV into various surfaces, including vehicles (VIPV). For a driving VIPV, the constant change in irradiance presents a significant challenge. The location, weather, and time are key factors that affect the irradiance prediction. An accurate prediction of solar energy generation is crucial for realizing the full potential of VIPV. In this study, the incident irradiance loss is referred to as shading loss.

This thesis is conducted in collaboration with Delft University of Technology (TU Delft) and the Netherlands Organisation for Applied Scientific Research (TNO). TNO has an existing shading loss model that accounts for the surrounding obstructions and weather effects using a fixed value, where the only variable input is the day of the year. On average, it assumes 27% shading losses yearly. This study has improved TNO's VIPV shading assessment by incorporating more variables into a new model, thereby contributing to a better estimation of the VIPV energy yield. The inputs of the new model are based on key factors causing irradiance loss, where location data is obtained using a Digital Surface Model (DSM). The new contribution to the DSM-based approach is the Web Coverage Service (WCS), which retrieves height data directly through a URL, eliminating the need for the previous manual operations and building upon the model's scalability. The improved model determines shading losses along a route using two varying shading indicators: Sky View Factor (SVF) and Shading Factor (SF). It can input various irradiance datasets, including or excluding weather effects, and precisely determines the Sun's position based on the time and day of the year.

The DSM-based approach is validated using a dynamic and static validation dataset, with a SVF$\leq$1. The accurate representation of surrounding obstructions during validation contributes to a good-quality model. Both validation studies differ in inputs based on location, time, and weather conditions. The differences in measured and simulated irradiance values are larger in the dynamic dataset than in the static dataset. Deviations are caused by uncertainties and errors, such as local weather effects, sensor inaccuracies, traffic shading, and LiDAR discrepancies, which is the inability to simulate open or changing structures. Weather variability is the primary factor affecting model quality in this validation study, resulting in no fixed inaccuracy factor for model validity. The validated model can accurately represent the environment, but weather variability should be minimized when comparing measured and simulated irradiance. Therefore, averaging is chosen to compare results in this work as it removes unknown or untraceable data points.

Beyond previous research studies, this work focuses on two public transport case studies, given the systematic routing with a fixed timetable. The first case study includes a car and a bus, and the second, more extensive case study focuses solely on buses. The choice of inputs in both case studies centres on key factors influencing VIPV irradiance loss. In the Bus 40 study, simulations under clear sky conditions and a fixed time around solar noon resulted in shading losses of 22.7% for the bus and 27.7% for the car. Moreover, the simulated shading loss shows a 2.6% relative difference compared to the yearly average TNO value. For the case study considering 27 bus routes in Amsterdam, simulations are performed using averaged KNMI irradiance and all hours a day, where the annual average shading loss resulted in 24.8%. The SF and clear sky irradiance correlate in the first case study and the SVF and average KNMI irradiance correlate in the second case study. However, using clear sky conditions and uniform overcast conditions does not represent realistic weather conditions and leads to a bias in the correlation. Moreover, classified terrain types do not correlate with SVF, in contrast to the reversed approach by Araki et al.

Finally, the model can effectively characterize the shading losses on the route level. However, this methodology falls short when reaching finer resolution, such as when examining smaller route segments or partial shading. The determination of shading losses at the route level can be of further benefit to various stakeholders, such as bus operators who want to determine the optimal bus routes for maximum solar energy generation. In addition, this model can be helpful for policymakers, to predict the required charging infrastructure in a scenario when vehicles are equipped with solar panels. Moreover, this model improves shading loss estimation by accepting a range of datasets instead of TNO's current approach. By inputting irradiance data for clear skies to complete overcast skies, the shading losses can be predicted in a safer range instead of over- or underestimation based on one shading value.

Contents

Preface i

Summary ii

Nomenclature ix

1 Introduction 1
- 1.1 Research objective . . . 2
- 1.2 Scope . . . 2
- 1.3 Report outline . . . 3

2 Background and literature review 4
- 2.1 Introduction in VIPV . . . 4
  - 2.1.1 VIPV technologies . . . 5
  - 2.1.2 Working principle of a VIPV system . . . 5
- 2.2 TNO's State-of-the-Art Model . . . 6
- 2.3 Varying shading in VIPV . . . 6
  - 2.3.1 Position of the Sun . . . 7
  - 2.3.2 Solar irradiance models . . . 8
  - 2.3.3 Computation of solar irradiance . . . 9
  - 2.3.4 Irradiance databases . . . 11
  - 2.3.5 Sky View Factor (SVF) for a non-free horizon . . . 12
  - 2.3.6 Changing environment . . . 14
  - 2.3.7 Categorized environments . . . 15
- 2.4 State-of-the-art approaches and values . . . 17
- 2.5 Research questions . . . 17

3 Methodology 19
- 3.1 Evaluation of approaches . . . 19
  - 3.1.1 Multi-Criteria Analysis (MCA) . . . 19
- 3.2 Chosen approach . . . 20
- 3.3 Modelling input data . . . 20
  - 3.3.1 Study area . . . 20
  - 3.3.2 Digital Surface Model (DSM) . . . 21
  - 3.3.3 Time and day of the year . . . 22
  - 3.3.4 Irradiance . . . 22
- 3.4 Modelling methodology . . . 22
  - 3.4.1 Horizon scanning algorithm . . . 22
  - 3.4.2 2D view factor (VF) model for SVF determination . . . 24
  - 3.4.3 Sun position calculation for SF determination . . . 25
  - 3.4.4 Irradiance model . . . 25
- 3.5 Varying shading indicators . . . 25
  - 3.5.1 Discrete Shading Factor (SF) . . . 26
- 3.6 Determination of the terrain types . . . 26
- 3.7 Workflow . . . 27
- 3.8 Conclusion . . . 28

4 Model Validation and Sensitivity Analyses 29
- 4.1 Validation datasets . . . 29
- 4.2 Dynamic dataset . . . 29
- 4.3 Uncertainty analysis of dynamic data . . . 33
  - 4.3.1 Sensor inaccuracy . . . 33
  - 4.3.2 Time- and distance-based road survey points . . . 33
  - 4.3.3 GPS offset errors . . . 34
- 4.4 Static dataset . . . 35

4.5 Uncertainty analysis of static data . . . 37
4.6 Deviations in measured and simulated irradiance . . . 37
4.7 Sensitivity analysis of terrain types . . . 38
4.8 Conclusion . . . 39

5 Case Studies **40**
5.1 Bus routes . . . 40
5.1.1 Bus 40: Rotterdam-Delft . . . 40
5.1.2 Bus routes of Amsterdam . . . 40
5.2 Partial shading . . . 42
5.2.1 MPPT losses in literature . . . 44
5.3 Conclusion . . . 45

6 Results **46**
6.1 Bus 40 route: Rotterdam-Delft . . . 46
6.2 Bus routes of Amsterdam . . . 49
6.3 Conclusion . . . 52

7 Discussion **53**
7.1 Literature comparison . . . 53
7.2 Discussion of the results . . . 53
7.2.1 Validation studies . . . 54
7.2.2 Case studies . . . 54
7.3 Contribution to beyond state of the art . . . 56
7.4 Limitations . . . 56
7.5 Outlook . . . 58
7.6 Conclusion . . . 59

8 Conclusions **60**

References **61**

A Conversion of Local Clock Time (LCT) to Julian Date (JD) **66**

B Solar position calculation **67**

C Perez component calculations **69**

D ArcGIS workflow manual **70**

E Algemene Hoogtekaart Nederland (AHN) **72**

F Clear sky irradiance model **73**

G Horizon scanner **75**
G.1 Web Coverage Service (WCS) request . . . 75
G.2 Horizon scanner code explanation . . . 75

H Verification of the Web Coverage Service (WCS) **78**

I Measurement uncertainty calculation **81**
I.1 Sensor specifications . . . 81
I.1.1 Dynamic validation dataset specifications . . . 81
I.1.2 Static validation dataset specifications . . . 81
I.2 Determination of the combined uncertainty . . . 81

J Characteristics and results for all bus routes of Amsterdam **83**

List of Figures

1.1 The increase in EV charging points from 2015-2022, where the Net Zero Scenario projects 17 million chargers needed by 2030 [2]. . . . 1
1.2 The two chosen vehicle categories differing in vehicle height, a passenger car and public transport bus with integrated PV, from Sono Motors [23]. . . . 3

2.1 Lightyear One (2020) [32] . . . 4
2.2 A schematic overview of a standard type of solar panel integrated in a car roof, after [39]. . . . 5
2.3 Workflow showing the conversion from sunlight into energy to supply for the VIPV battery, after [11]. . . . 6
2.4 The sky dome indicating the position of the Sun relative to the observer's point of view, which is the PV panel, using the altitude a_s, azimuth A_s & zenith angle θ_z, after [40]. . . . 7
2.5 Flow chart for determining the position of the Sun, after [43]. . . . 8
2.6 The sky dome (with an azimuth of 360° and altitude of 90°) projected on a circular plane, known as the polar projection, and vertical plane, known as the orthographic projection, after [44]. . . . 8
2.7 The three diffuse irradiance components (G_{iso}, G_{cir} & $_{hor}$) visualized in a sky dome, after [51]. . . . 10
2.8 Visualization of the view factor from the PV panel to the differential sky patch $d\Omega_{sky}$, after [58]. 12
2.9 Sky patch, where the position is indicated by ij, visualized on the sky dome and the relation between the angles is: θ_1 + $a_s{}^{ij}$ = $\frac{\pi}{2}$. . . . 13
2.10 An orthographic projection of a discretized sky dome indicating the different sky patch weights. 14
2.11 An original fisheye image in grey-scale (left) and a filtered fisheye image indicating obstructions in black and the sky in white (right) [15]. . . . 15
2.12 For a specified observer point within a building environment (right), a skyline graph in polar projection is generated using GIS software (left) [60]. . . . 15
2.13 Typical fisheye images of the three categorized environments: (1) open, (2) residential, and (3) urban [15]. . . . 16
2.14 The fraction of incident irradiance indicated as a ratio to GHI (on the y-axis) given as a function of the latitude on Earth (on the x-axis), for all three categorized shaded zones [64]. . . . 16

3.1 Topographical maps containing different information and data for analysis purposes [61]. . . . 21
3.2 Schematic visualization of the LiDAR scanning approach, after [75]. . . . 22
3.3 Left: top view of a height map in a grid format with the XY observer point indicated in orange, Right: side view of a scanned maximum altitude from the observer point, after [65]. . . . 23
3.4 An example of an orthographic skyline profile for a road survey point in the residential area of Echt, The Netherlands. . . . 24
3.5 An example of an orthographic skyline profile combined with sky patch weights for calculating the SVF value. . . . 24
3.6 A binarized shadow map from the skyline profile in Figure 3.4, where the angular resolution is enlarged for illustrative purposes< after [46]. . . . 24
3.7 The relation between the skyline profile, which quantifies the obstruction density, and the varying shading indicators: SF (left) and SVF (right). . . . 26
3.8 Bestand Bodemgebruik (BBG) map for the area of Amsterdam, indicated with the eight terrain categories in the legend (right) [78]. . . . 27
3.9 Workflow presenting the modelling methodology for obtaining the simulated irradiance, which is used to determine the shading loss. . . . 28

4.1 Vehicle Irradiance Test System (VITS) with four irradiance sensors mounted on each corner of the setup [12]. . . . 29
4.2 Comparison between measured, KNMI and clear sky irradiance datasets for the test route of the 9th of October 2019, including the time ranges of the vehicle being parked and driving. . . . 30
4.3 Midday route from the test data obtained on the 9th of October 2019 used for model validation. 30
4.4 Measured, simulated and KNMI irradiance for the midday test route in the dynamic validation dataset. . . . 31

4.5 Linear trend lines for each dataset indicated in the irradiance comparison graph illustrate the underlying trends for the midday test route in the dynamic validation dataset. 32
4.6 The correlation between temporal points and chosen spatial points based on the difference in average SVF, given in percentage (%). 33
4.7 A visible GPS offset in the dynamic dataset in a residential area in Echt, The Netherlands. . . . 34
4.8 Skyline comparison of the data point with a GPS offset of 5 meters (left) and the corrected data point (right), including the Google Street View verification. 35
4.9 The simulated skyline profile (left) and verification using a 360-degree Google Street View image (right) of the static pyranometer location in Den Bosch, The Netherlands. 35
4.10 Measured, clear sky & simulated irradiance for a near-clear sky day on the 11th of October 2015. 36
4.11 Normal distribution of the dynamic and static validation data, where the x-axis indicates the difference in measured and simulated irradiance and y-axis the probability density. 37
4.12 Two different approaches for extracting terrain types, where (a) intersects all surrounding polygons, and (b) intersects only the largest overlapping polygon. 38
4.13 Comparison of terrain type distribution intersecting all terrains (left) and only the largest overlapping terrain (right). 39

5.1 Bus 40 route, starting from Rotterdam Central (at 12:05) and arriving at Delft Station (at 12:43). 41
5.2 Averaging of hourly KNMI irradiance data into one respective day for June, where the 31 daily irradiance graphs (in blue) and averaged irradiance graph (in orange) are shown. 42
5.3 Bus routes in and around Amsterdam, categorized by surrounding terrain types from the land use (BBG2017) map [78]. 43
5.4 Roadway indicating the four sensors which measured irradiance with a frequency 1 Hz (left),and a close-up view of the four sensors in every corner of the vehicle (right). 43
5.5 Partial shading caused by a solid object, Viaduct Sterrenlaan in Eindhoven, plotted for the four irradiance sensors in the dynamic validation dataset. 44
5.6 Viaduct Sterrenlaan in Eindhoven, where the vehicle route is indicated in yellow and the underpass in red. 44
5.7 Partial shading caused by an irregular and complex object, plotted for the four irradiance sensors in the dynamic validation dataset. 44

6.1 Box plot illustrating the SVF ranges for both a car and bus along Bus route 40, with average SVF values of 0.74 for a car and 0.79 for a bus. 46
6.2 The annual shading loss curve for a passenger car (green) and public transport bus (yellow) driving the Bus 40 route. 47
6.3 Difference in visibility angle (ϕ) for the passenger car and public transport bus for the same obstruction. 47
6.4 Annual shading loss curves showing the difference between the TNO shading assessment (in blue), based on the Cobbenhagen case study [11], and the simulated irradiance (in green) for both a passenger car. 47
6.5 Discrete shading factor (SF) values for the months June (left) and December (right) in the Bus 40 case study, travelling from Rotterdam Central to Delft Station. 48
6.6 Correlation between average SF and monthly average irradiance (in W/m^2) for the Bus 40 case study, where R^2=0.972. 48
6.7 Monthly average irradiance for the 27 bus routes of Amsterdam, using averaged KNMI weather data, where the irradiance values (in W/m^2) deviate for different bus routes. 49
6.8 Annual average irradiation for the 27 bus routes of Amsterdam, shown on the geographical map. 50
6.9 Correlation between SVF and annual irradiation for each road survey point, in the case study for the 27 bus routes of Amsterdam, where R^2=0.896. 50
6.10 Correlation between SVF and built terrain covered (%) for each road survey point in the bus routes of Amsterdam case study. 51

7.1 Illustrative example of two skyline profiles with a similar SVF value and the same position of the Sun, resulting in a different SF value and portion of built terrain (%) 55
7.2 Illustrative example of a route discrepancy in one of the bus routes of Amsterdam, leading to an erroneous skyline. 55
7.3 Differences in skylines along a route for different spatial starting points, resulting in differences in the SVF. 57

B.1 The Earth revolving around the Sun for a full year, indicating the equatorial plane, orbital plane and axial tilt (δ), after [104]. 68

D.1 Illustration of the ArcGIS Tabulate Intersect tool, where 'zone' refers to each buffer, and 'class features' refers to the land use (BBG) map, including different colors which represent terrain types, after [105]. 71

E.1 AHN3 map of The Netherlands indicating the division into different map sheets [73]. 72
E.2 AHN3 map of The Netherlands indicating the division of the different years in which LiDAR data is collected [73]. 72

F.1 The clear sky irradiance simulated for the 11^{th} of October for the static pyranometer in Den Bosch, The Netherlands, through the usage of PVlib [54]. 74

G.1 An illustrative example of a slice not enclosing a height data point, where the solution is the red, dashed line illustrating the close wall effect using the angle correction range (ACR) [65]. 76

H.1 The verification of the horizon scanning approach using an example data point with GPS coordinates (51.10534, 5.874985) in Echt, The Netherlands, where ArcGIS is used to (1) scan the surroundings using a radius of 100 meters and (2) obtain the distance and direction to a visible obstruction. . 78
H.2 Horizon scanning geometry relation. 79
H.3 Google Street View image, where a (seasonally) varying obstruction is shown, a tree, in front of a house in Echt, The Netherlands. 79
H.4 (1) Distance and direction from the example data point to a nearby obstruction, (2) Point of view from the data point to the obstruction using Google Street View. 79
H.5 Clipped skyline representation to identify the maximum altitude (40°) for an azimuth of 285°, for verification of the horizon scanning approach. 80

List of Tables

1.1 The two case studies researched to determine the shading losses in VIPV using an improved shading assessment. . . . 3

2.1 Typical SVF values for open, residential and urban zones [15]. . . . 17

3.1 Comparison of three modelling approaches using multi-criteria analysis. . . . 20

4.1 Average irradiance, SVF and SF values for three irradiance datasets including the shading losses relative to KNMI irradiance for the midday route in the dynamic validation dataset. . . . 32
4.2 Average irradiance, SVF, and SF values for three datasets with the relative percentage difference between measured and simulated irradiance in the static validation dataset. . . . 36
4.3 Different inputs for the validation studies based on the significant irradiance loss factors in VIPV: irradiance data, specific time frame, and surrounding environment. . . . 39

5.1 The route characteristics and modelling inputs for the Bus 40 case study [89]. . . . 41
5.2 The route characteristics and modelling inputs for the buses of Amsterdam case study [91]. . . . 42
5.3 Different inputs for the case studies based on the significant irradiance loss factors in VIPV: irradiance data, specific time frame, and surrounding environment. . . . 45

6.1 Average varying shading indicators, SVF and SF, for both vehicle categories and the annual average shading loss values for Bus route 40 46
6.2 Key results of the two performed case studies, based on the annual average irradiation and investigated correlations, where X indicates it has not been investigated. . . . 52

7.1 Values for the two skyline profiles in the illustrative example 55
7.2 Summary of input datasets for validation and case studies 59

C.1 Sky clearness categories for each bin [47]. . . . 69
C.2 Perez coefficients for irradiance modelling [47]. . . . 69

F.1 Inputs for the Ineichen-Perez Clear Sky irradiance model [54]. . . . 73

G.1 The WCS GetCoverage request URL and settings for obtaining AHN3 DSM data from PDOK [73]. . . . 75

I.1 Measurement uncertainties from the irradiance sensor, data logger and GPS specification sheets [84, 86, 97], for the dynamic dataset. . . . 81
I.2 Error analysis and the combined standard uncertainty computation for the irradiance sensor and data logger used in the dynamic VITS data, using the procedures given by R.R. Cook [83]. 82

J.1 Summary of characteristics and annual average irradiation results for the 27 bus routes of Amsterdam, given as a color scale [91, 107, 108]. . . . 83

Nomenclature

Abbreviations

Abbreviation	Definition
2D	Two-Dimensional
ACR	Angle Correction Range
AHN	Actueel Hoogtebestand Nederland
AOI	Angle of Irradiance
BBG	Bestand Bodemgebruik
BEV	Battery Electric Vehilce
BIGEYE	Bifacial Gain and Energy Yield
BIPV	Building integrated PV
CBS	Centraal Bureau voor Statistiek
c-Si	crystalline Silicon
DHI	Diffuse Horizontal Irradiance
DNI	Direct Normal Irradiance
DOY	Day of the Year
DSM	Digital Surface Model
EDR	Extended Driving Range
EFM	Energy Flow Model
EU	European Union
EV	Electric Vehicle
GHI	Global Horizontal Irradiance
GIS	Geographic Information System
GMST	Greenwich Mean Sidereal Time
GPS	Global Positioning System
GTFS	General Transit Feed Specification
HV	High Voltage
IEA	International Energy Agency
JD	Julian Date
KNMI	Royal Netherlands Meteorology Institute
LCT	Local Clock Time
LiDAR	Light Imaging Detection And Ranging
LMST	Local Mean Sidereal Time
MPPT	Maximum Power Point Tracker
NWB	Nationaal Wegenbestand
NZE	Net Zero Emissions
PV	Photovoltaic
PVPS	Photovoltaic Power Systems
R&D	Research & Development
RWS	Rijkswaterstaak
SAM	System Advisor Model
SC	Shading Coefficient
SF	Shading Factor
SoC	State-of-Charge
STC	Standard Test Conditions
SVF	Sky View Factor
TRY	Test Reference Year
TNO	Netherlands Organisation for Applied Scientific Research
UAV	Unmanned Aerial Vehicle
UTC	Coordinated Universal Time

Abbreviation	Definition
VF	View Factor
VIPV	Vehicle Integrated Photovoltaics
VITS	Vehicle Irradiance Test System
WCS	Web Coverage Service
Wp	Watt peak

Symbols

Symbol	Definition	Unit
θ_Z	solar zenith angle	°
θ_L	Local Mean Sidereal Time	°
θ_M	PV module tilt	°
ϕ_0	latitude of the observer	°
λ_0	longitude of the observer	°
λ_s	longitude of the Sun	°
α	albedo	-
δ	axial tilt of the Earth	°
μ	mean	-
σ	standard deviation	-
ϕ	visibility angle	°
a	equatorial coordinate	°
a_S	solar altitude angle	°
A_S	solar azimuth angle	°
A_M	azimuth angle of the PV panel	°
f	sampling frequency	Hz
H	height	m
L	length	m
g	mean anomaly of the Sun	°
q	mean longitude of the Sun	°
t	time of data point	s
T	time interval	s
W	width	m
x	ecliptic coordinate	°
I	irradiance	W/m^2

1 Introduction

The International Energy Agency (IEA) emphasizes the expected electric vehicle (EV) growth in numbers [2]. The global EV fleet, which stood at approximately 30 million in 2022, is projected to reach about 240 million in 2030 [2]. As the number of EVs increases, the dependency on charging from the electricity grid increases [2]. Public chargers are becoming more necessary to match the convenience of traditional refuelling [2]. The IEA's Net Zero Emissions by 2050 scenario (NZE) presents a clear path for the global energy sector to achieve net zero CO_2 emissions by the year 2050. In the NZE, it is projected that by 2030 there will be 17 million publicly accessible charging stations, representing a substantial rise compared to the previous years [2]. Recently, the members of the European Parliament agreed that there should be at least one car-recharging station every 60 kilometres along the main EU roadways by 2026 [3]. This newly adopted regulation supports the IEA's NZE scenario. Figure 1.1 illustrates the projected increase in EV charging points for the NZE scenario, where the expected dependency on the grid is growing [2].

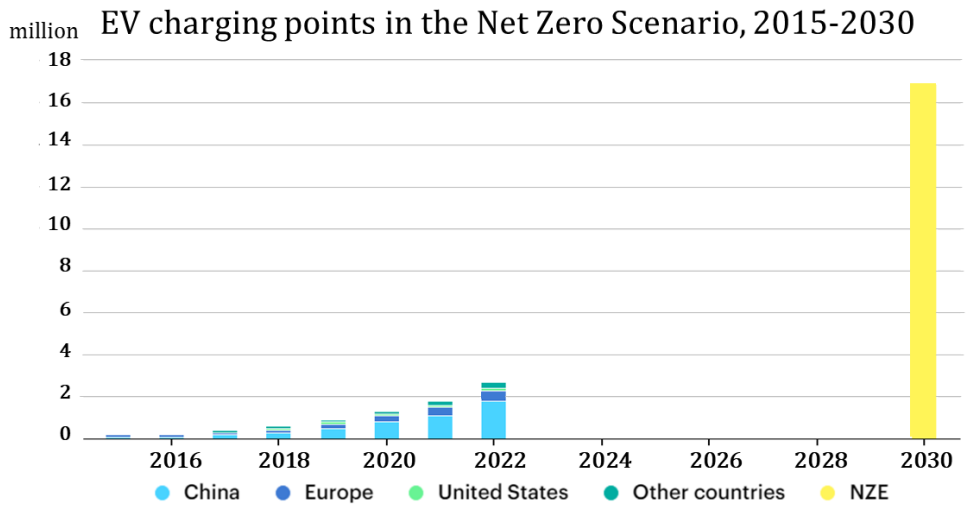

Figure 1.1: The increase in EV charging points from 2015-2022, where the Net Zero Scenario projects 17 million chargers needed by 2030 [2].

Grid resilience is necessary to overcome power outages as the local grid experiences growing congestion levels [4]. To be less dependent on the charging infrastructure, there is an increasing interest in innovative technical solutions that enhance the driving range of EVs without the need for grid charging. For example, by directly charging using electricity generated by renewable energy sources. The growth of solar energy stands unparalleled among other renewable energy generation technologies [5]. The solar industry has witnessed substantial growth in recent years and led to significant technological advancements. In 2022, a global solar capacity of over 1 TW has been achieved [5]. In the coming years, a potential for an annual TW-scale market is expected [6]. The growing solar industry, alongside the expanding EV fleet, presents an opportunity for solar installations to directly facilitate charge to EVs, resulting in an increased autonomy [7].
Vehicle-integrated photovoltaic (VIPV) technology incorporates solar panels into the exterior of EVs (such as the roof, rear sides, car hood, and windows), enabling direct solar energy generation on the vehicle's surface. According to research conducted by PwC Strategy&, it is projected that achieving a 20 percent adoption rate of hyper-efficient vehicles with integrated PV (VIPVs) could result in a €2.2 billion reduction in electricity infrastructure investments in The Netherlands between 2022 and 2040 [8]. This translates into fewer and less powerful EV chargers needed, as part of the electricity can be supplied using VIPV-generated solar energy.

Solar panels in vehicles prioritize driver convenience over optimal solar energy capture, unlike static PV installations designed to maximize the amount of irradiance that can be captured [9]. For a moving vehicle with

integrated PV (VIPV), the generated solar energy is more difficult to predict. The constant change in incident irradiance, leading to reduced solar energy generation, presents a significant challenge [4]. The key factors that cause a reduction in irradiance include shading from the surrounding environment (such as buildings and trees), weather effects (such as overpassing clouds), and the varying position of the Sun, which changes with the time and day of the year [10]. For instance, a nearby building can obstruct the Sun's rays from reaching the solar panel, resulting in a shaded panel where the incident irradiance is reduced. The fraction of incident irradiance lost is referred to as shading loss in this thesis.

This thesis is conducted in collaboration with Delft University of Technology (TU Delft) and the Netherlands Organisation for Applied Scientific Research (TNO). TNO's current VIPV shading assessment uses a fixed value to account for the surrounding obstructions and weather effects, where the only variable input is the day of the year (DOY). The values are based on a simulated case study performed by Cobbenhagen in 2016 [11]. The required location data is based on the Eindhoven suburb Woensel in The Netherlands and includes a historical irradiance dataset obtained from a nearby location. The shading loss values vary in a simplified sinusoidal relation, which is assumed to be similar for all routes in The Netherlands. In a TNO research study by Carr et al. [12], the VIPV-generated solar energy contribution to the total vehicle energy requirement was assessed for various locations. This study emphasizes the importance of the location and amount of sunlight exposure in evaluating VIPV's solar energy potential, supported by several studies which emphasize this significance for VIPV as well [13, 14, 15]. Different studies have approached different methods to estimate the incident irradiance for a specific vehicle or route more accurately; these include experimental as well as simulation modelling approaches [16, 17, 18, 19]. The current state-of-the-art studies include different vehicles and environments, mainly focused on one particular case study.

1.1. Research objective

The research objective of this study is to improve TNO's current VIPV shading assessment by incorporating more variables into a new model and thereby contributing to a better estimation of the VIPV energy yield. Given that TNO's current shading assessment varies based on the DOY, this thesis aims to develop a location- and time-specific shading model that can input various irradiance datasets. The goal of this research is to apply the improved shading model to two case studies, where one includes both a car and bus and the other more extensive one focuses solely on buses. By inputting different datasets focusing on the key factors for both case studies, the differences in irradiance loss can be quantified using the improved model. This contrasts with current studies focusing on one input dataset [14, 17, 16, 18]. In the subsequent Chapters of this report, three research questions are addressed that focus on the foundation of this research: the methodology, quality, and key results of the improved shading model. The specific research questions will be stated in Section 2.5 in Chapter 2.

The necessity of a location- and time-specific shading model extends to various stakeholders. The enhanced model has a valuable application within the SolarMoves project [20], which TNO is part of. This project focuses on VIPV's potential and offers policy recommendations to the European Commission [20]. For policymakers, the focus lies on determining optimal locations for charging stations and their distribution within certain areas. A location- and time-specific shading model for VIPV enables irradiance loss assessment for specific routes to estimate the solar energy generation and determine the dependency on the charging infrastructure. Additionally, for bus operators, a location- and time-specific shading model can be useful for determining the most suitable bus routes that allow for the highest solar energy generation when integrating solar panels on buses.

Araki et al. categorized different areas and surroundings into three distinct shading environments—open, residential, and urban—based on land roughness indicators, used for giving an approximation of the shading losses [21]. This study takes a different approach by using a topographical map to classify various areas into terrain types. The goal is to explore whether these terrain types can approximate VIPV shading loss. The scope and case studies of this research are outlined in the next Section 1.2.

1.2. Scope

The scope of this work is limited to a simplified situation of a vehicle fitted with a flat and horizontal (0° tilt) solar panel on the vehicle roof. This approach does not consider integrating solar panels on different parts of the vehicle body. Studies show that vertically integrated PV panels, such as those on vehicle doors, receive about half the incident irradiance compared to a horizontal PV panel on the vehicle roof [7, 22]. Therefore, only a horizontal solar panel is considered for this work. This approach leaves the complexities encountered by curved PV panels out of scope and simplifies the integrated PV as a flat PV panel. In addition, TNO provides data from horizontal irradiance sensors on a moving vehicle, supporting the validation of the model [12]. Furthermore, this work focuses on one point on the panel, which does not account for partial shading

losses or the optimization of cell interconnection, as these aspects are beyond its scope. This leads to the assumption that the solar panel is uniformly shaded.
Beyond previous research studies focusing on one vehicle type, this research examines two different vehicle categories to determine the irradiance losses in VIPV [14, 16, 18, 17]. A systematic route with a fixed timetable is suitable for identifying the shading losses. As many public transport systems operate on predetermined routes, which do not change regularly, it is chosen to focus both case studies on public transport routes. The case studies in this research focus on Bus 40 routing from Rotterdam to Delft, including two vehicle categories (a public transport bus and a passenger car), followed by a more extensive case study that focuses on all 27 bus routes of Amsterdam (using only a public transport bus). Figure 1.2 shows the two chosen VIPV categories, which differ in vehicle height.

Figure 1.2: The two chosen vehicle categories differing in vehicle height, a passenger car and public transport bus with integrated PV, from Sono Motors [23].

The integrated photovoltaic (PV) area varies considerably depending on the type of vehicle. For cars, the PV area typically ranges from 2-9 m^2, whereas, for buses, it can extend up to 30 square meters [24]. Differences in vehicle dimensions and vehicle energy consumption make it complicated to compare or evaluate them [25]. This study specifically concentrates on modelling the incident irradiance and excludes PV energy yield estimation, which involves thermal and electrical models [26]. To determine shading losses, various irradiance datasets are considered, including historical weather data and empirical weather models.

Summarizing, this research study is scoped to a flat and horizontal PV system homogeneously irradiated without considering partial shading on a PV panel. Furthermore, this thesis excludes the PV energy yield estimation and only focuses on the irradiance losses, referred to as shading losses. The improved shading model, with the intended scope, is applied to two case studies based on public transport routes. Finally, surrounding environments are categorized to assess the feasibility of approximating the shading effect using these classified terrain types. The two case studies in this thesis are presented in Table 1.1.

Case studies	**Number of bus routes**	**Vehicle catergories**		**Terrain type classification**
		Passenger car	Public transport bus	
Bus route 40: Rotterdam to Delft	1	X	X	
All bus routes of Amsterdam	27		X	X

Table 1.1: The two case studies researched to determine the shading losses in VIPV using an improved shading assessment.

1.3. Report outline

To fulfil the research objective and sub-questions, which will be stated in Section 2.5 in Chapter 2, this work is structured as follows. In Chapter 2, the literature review and background knowledge of the project is explained, followed by the research questions addressed in this work. Chapter 3 performs a multi-criteria analysis for different modelling approaches and describes the necessary input data for the chosen model, the improved methodology, and the workflow. This is followed by Chapter 4, which focuses on the validation and associated sensitivity analyses of the model. The chosen public transport case studies are presented in Chapter 5. In Chapter 6, the key results are given for the case studies. Consequently, Chapter 7 discusses the key findings, and contribution to the research field and presents the limitations followed by how they can be improved in the outlook. Chapter 8 states the conclusions.

2
Background and literature review

This Chapter elaborates on the concept of vehicle-integrated PV (VIPV) in Section 2.1, which includes the history, state-of-the-art developments, and working principle of the technology. The TNO shading assessment is presented in Section 2.2, and the key factors contributing to irradiance loss are explained in Section 2.3. This is followed by the determination of the Sun's position in Section 2.3.1, irradiance datasets and calculations in Section 2.3.2-2.3.5, and the identification of the surrounding environment in Section 2.3.6. Section 2.4 summarizes the state-of-the-art models and elaborates on the current level of knowledge in this field. Finally, the research questions related to this work are laid out in Section 2.5.

2.1. Introduction in VIPV

The history of vehicle-integrated photovoltaic (PV) panels can be traced back to the 1980s, marked by the construction of the first solar-powered car [27]. In 1977, an American engineer named Ed Passerini pioneered the development of a solar-powered vehicle named "Bluebird," which featured the integration of photovoltaic panels into its body structure. The car relied on a battery pack charged by solar panels mounted on its roof, enabling it to achieve a range of approximately 80 kilometres [27]. In the following years, several universities and research institutions built cars with integrated PV panels, with increasing ranges and new technologies, for participating in competitions such as the World Solar Challenge in Australia. Nowadays, solar panels have been integrated into a range of vehicles, which include passenger cars, buses, trains, planes, and even unmanned aerial vehicles (UAVs) such as drones [17, 28, 29]. The increasing deployment of VIPVs is due to the increased efficiencies in PV solar cells leading to higher energy generation densities at lower costs [30]. VIPV systems can effectively provide auxiliary power and even extend the range of vehicles [15].
Car manufacturers, such as Mercedes, Audi, and Hyundai, have incorporated solar panels into the exterior of some of their electric vehicles (EVs) [31]. On top of traditional companies, Lightyear and Sono Motors were developing PV-powered passenger cars and were known as pioneer manufacturers within the VIPV industry [7]. Lightyear One, given as an example in Figure 2.1, has proven to be around 50 percent more efficient than the average EV in the current market [8]. This translates into a range of up to 70 kilometres per day, depending on the driving conditions and circumstances, resulting in fewer charging moments [32]. While both companies had taken steps to develop hyper-efficient VIPVs, they have now declared bankruptcy. However, this illustrative scenario does demonstrate the high potential of the technology.

Figure 2.1: Lightyear One (2020) [32]

In a research study by Carr et al. [12], the VIPV system's contribution to the total vehicle energy requirement was assessed for The Netherlands. This research assumes a 800 Wp PV panel and energy consumption data from EV-database.org [33]. For a Tesla car driving 13,000 km in Amsterdam, The Netherlands, the PV contribution is calculated to be 26.1% [12]. According to a research study by NEDO [13], PV technology that is currently available can enable vehicles to cover 10% to 20% of their annual average distance, with a peak daily contribution of more than 20% during summer and approximately 10% during winter. Moreover, a study

by Heinrich et al. shows that the VIPV driving range can be extended by 13-23% of a yearly distance of 15,000 km in Germany, assuming the generated solar energy can be fully supplied [34]. The factors which affect solar energy supply vary and these studies emphasize the need for further investigation.

2.1.1. VIPV technologies

Initially, the generated solar energy was used as an auxiliary energy source providing power for the secondary systems in a vehicle, such as air-conditioning and lighting [15]. Following the improvements within the PV market where the PV module efficiency is increasing and the cost is decreasing [6], the solar energy generated by integrated PV can supply a significant amount of electricity to the vehicle battery system, naturally depending on various factors such as vehicle efficiency and location [13]. The limited space available on a vehicle imposes a significant emphasis on the efficiency of photovoltaic (PV) cells [7]. Silicon-based PV cells have a market share of about 95% and are the most dominant technology, as of their high efficiency and low cost [35]. Sono Motors and Lightyear were both pioneers in manufacturing PV-driven vehicles in Europe and were equipped with crystalline silicon (c-Si) cells [36].
A PV module contains interconnected solar cells. The amount of electricity generated at any given time depends on the series and parallel electrical connections between them, as well as the quantity of PV cells and bypass diodes [37]. As a result, the energy produced will vary based on the size, connectivity, and incident irradiance of the cells [38]. Considering requirements for automotive applications, such as maximum temperatures, crashes and vibrations, a typical VIPV module is covered in glass, which is the most favourable [13]. In Figure 2.2, TNO constructed a schematic representation of the integrated PV panel. The setup generally consists of a cell layer encapsulated by the encapsulant, indicated in red in the Figure, and a front- and backsheet [39].

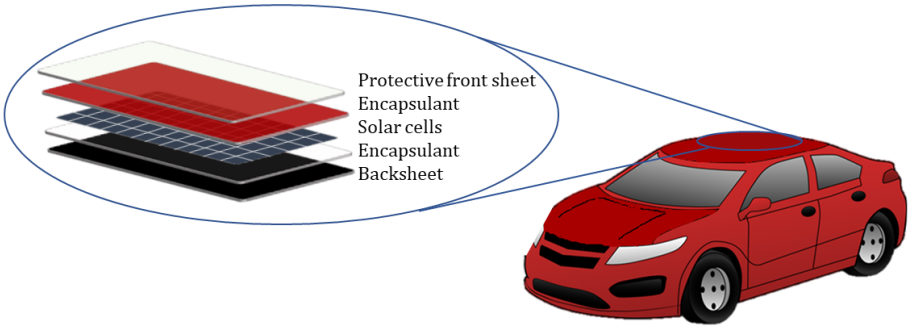

Figure 2.2: A schematic overview of a standard type of solar panel integrated in a car roof, after [39].

Lightyear One, the first vehicle from Lightyear, featured a 5 m^2 PV area, with its c-Si solar modules achieving a peak power of approximately 215 Wp/m^2 under Standard Test Conditions (STC) [32]. Another PV technology which can be applied in VIPV is III-V thin film solar cells due to very high power conversion efficiencies [36, 13]. Even though III-V thin film solar cells have the highest efficiency, they also have the highest cost. The techno-economic analysis shows that the accounting costs are too high for VIPV applications with this type of PV installed. However, capacity costs below 1 USD/Wp can make it economically feasible by wafer reuse or inexpensive silicon substrates [7]. Therefore, costs are also an essential aspect of VIPV, similar to other PV applications and installations.

2.1.2. Working principle of a VIPV system

When converting sunlight into electrical energy, a solar module utilizes the photovoltaic (PV) effect. Each solar module comprises several interconnected cells. To convert electrical energy provided by solar cells to the battery of the vehicle, each PV system has a maximum power point tracker (MPPT), DC/DC converter, high voltage (HV) bus, and the required power electronics before directing this energy into the vehicle battery [40]. The MPPT maximizes the electrical output from solar panels by continuously tracking the point at which the panels produce the most power under varying conditions [40]. A maximum power point tracker (MPPT) implemented in VIPV potentially has to handle fast changes in PV output power due to frequent and irregular shading on the PV panel [41]. Furthermore, the DC/DC converter converts the electrical power from the solar cells to the HV bus, where the HV bus of the vehicle ensures the distribution of the current and voltage [11]. An overview of the workflow from solar energy to the battery of a VIPV is shown in Figure 2.3.
Each electrical component has necessary parameters that need to be specified to determine the solar energy supply for a VIPV. Examples of these parameters are the area of the integrated solar panel and the associated efficiencies of the components. Within TNO, an in-house model is developed which relates the vehicle energy consumption with the annual VIPV energy yield [12].

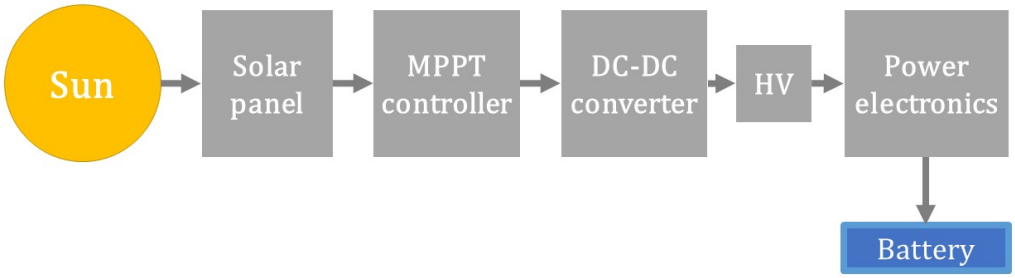

Figure 2.3: Workflow showing the conversion from sunlight into energy to supply for the VIPV battery, after [11].

However, as stated in Section 1.2, this work excludes the PV energy yield estimation and only focuses on the irradiance loss. The amount of incident irradiance received by the solar panel relates to the first and second block in the workflow diagram presented in Figure 2.3. In the TNO's state-of-the-art model, a VIPV shading assessment is used to account for the irradiance losses in VIPV, which will be elaborated upon in more detail in the following Section 2.2.

2.2. TNO's State-of-the-Art Model

TNO has developed the Energy Flow Model (EFM), which is a time-series-based model and relates the vehicle energy consumption with the annual VIPV energy yield [12]. The EFM simulates the charging and discharging of an electric vehicle (EV) battery and assesses how vehicle specifications and charging approach affect the overall photovoltaic (PV) contribution [12]. It considers different inputs, ranging from other driving profiles up to various vehicle and PV specifications. Within this model, the VIPV shading losses of a car in motion are assumed to be 27% on average and adjusted for a specific day in the year (DOY) [25]. The shading loss values are assumed to be similar for the entire area of The Netherlands, based on a case study conducted by Cobbenhagen [11]. This case study includes an averaged factor for shading resulting from the surrounding environment by only using location data from Woensel, The Netherlands. In addition, Cobbenhagen includes one averaged historical irradiance dataset obtained from a nearby KNMI weather station. The only variable input for determining the irradiance loss is the DOY, where the relation is given as a simplified sinusoidal formula [11]. The formula in Equation (2.1) shows the VIPV shading assessment currently used by TNO in the EFM model.

$$SC = \frac{0.23 + 0.54}{2} - \frac{1}{2} \cdot (0.23 - 0.54) \cdot cos(2 \cdot \pi \cdot \frac{DOY + 10}{365}) \tag{2.1}$$

where the outcome is the shading coefficient (SC). The decimal numbers 0.23 and 0.54 are the shading fractions for June and December, and DOY is the day of the year. This indicates shading losses of 54% in December and 23% in June obtained from the simplified sinusoidal relation [11]. The yearly average shading loss obtained in the study of Cobbenhagen equals 27% [11]. In Equation 2.1, the factor '+10' indicates the astronomical winter, where a value of 10 is added to the 22nd of December (depending on the December solstice) to get back to day one, which is the 1st of January [40]. Furthermore, the factor $2 \cdot \pi$ is multiplied by the fraction $\frac{DOY+10}{365}$, where DOY is converted into radians for the computation. By inserting the DOY value, the shading loss can be estimated using this simple relation. To enhance the current shading assessment, Section 2.3 delves into factors which cause varying shading losses.

2.3. Varying shading in VIPV

The position of the Sun is crucial for calculating the irradiance incident on a solar panel, concerning how high or low the Sun is on the horizon, and varies for each location and time [42]. The determination of the Sun's position is explained in Section 2.3.1. Direct sunlight reaches the PV panel when the Sun is high in the sky on a sunny day. On the other hand, on a cloudy day, the Sun rays might not directly reach the PV panel, resulting in a decrease in direct sunlight and an increase in diffuse light [40]. This highlights the significance of weather conditions, as they influence the amount of incident solar irradiance [40]. The key concepts relevant for computing solar irradiance, related to direct, diffuse and reflected irradiance, are discussed in Section 2.3.3.

In the case of integrated PV systems, such as those in vehicles (VIPV), obstructions surrounding the solar panel can lead to the Sun being obstructed, causing shading on the solar panels [10]. Ultimately, a moving VIPV experiences changing environments leading to different irradiance levels and is discussed in Section 2.3.6. The change in different factors causing a PV panel to be shaded, in this work assumed to be uniformly shaded, is referred to as varying shading loss in this study. As introduced in Chapter 1, the varying shading is

influenced by three key factors: the time (for the position of the Sun), weather (including different conditions, such as clouds), and the location (related to the surrounding environment and obstructions). The key factors contributing to shading losses in VIPV will be discussed in the following Sections.

2.3.1. Position of the Sun

As the position of the Sun is dependent on the location of the Earth and the time of the day in the year, the concept of the celestial sphere is used. The apparent motion of the Sun across the sky, seen from the observer, can be described using this concept [42]. The sky dome represents the visible portion of this celestial sphere as observed from a specific location on Earth. The Sun's position can be determined using the concept of the sky dome [40].

Sky dome

The relative position of every celestial object, seen from the observer point, is described using two angles in the horizontal coordinate system [40]. The first is the angular elevation, known as the altitude angle (a_s). The angular range is from -90° up to 90°, where below 0° the object is below the horizon and therefore not visible from the observer's point of view. At 90°, a celestial object reaches its zenith, which is the point in the sky where the vertical intersects the celestial sphere. The celestial sphere is known as the sky dome, which can be seen as half of a sphere in Figure 2.4. The altitude and zenith angle are related as $\theta_z = 90° - a_s$, which can be seen in the sky dome representation in Figure 2.4. The second angle in the coordinate system is known as the azimuth angle (A_s) and represents the angle formed by the projected line of sight on the horizontal plane, as explained in Smets et al. [40]. The angular range is from 0° up to 360°, starting at North for $A = 0°$, and followed by East, South, and West for the azimuth being 90°, 180° and 270°. The sky dome refers to the entire sky from horizon to zenith for all azimuthal directions.

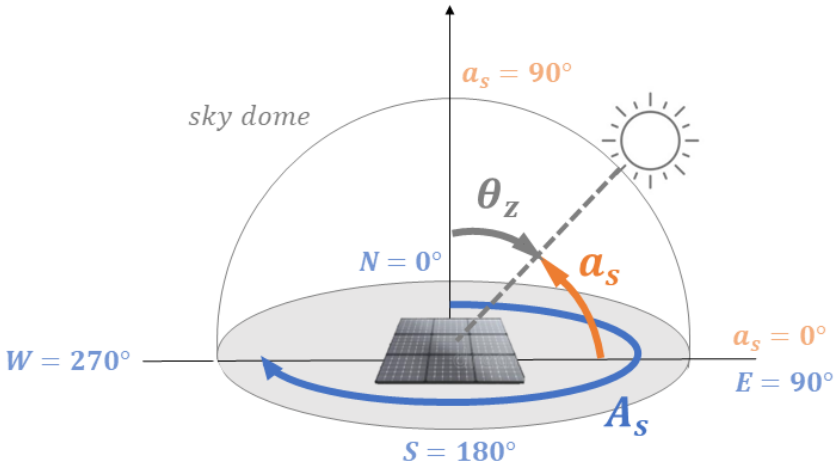

Figure 2.4: The sky dome indicating the position of the Sun relative to the observer's point of view, which is the PV panel, using the altitude a_s, azimuth A_s & zenith angle θ_z, after [40].

Sun angles

The position of the Sun is defined by the altitude and azimuth angles, known as the sun angles. The sun angles are computed at a time and location of interest. The time daily used, also known as Local Clock Time (LCT), is not suitable for accurately describing the position of the Sun. It does not encounter the adjustments made by humans, such as time zones and variations in the Earth's orbit [11]. Therefore, the LCT needs to be converted into the effective time, which can be done using the Julian dating system [42]. The conversion of the Local Clock Time (LCT) to Julian date (JD) is given in Appendix A, where the relevant concepts for the conversion are explained in more detail. After having obtained the JD, the sidereal time can be computed. This is a measure of time used in astronomy and celestial navigation to determine the position of the Sun by observing the celestial objects in the sky [42]. In this work, the celestial object of interest is the Sun. Using the Equations and variables provided in Appendix B, the position of the Sun can be calculated [40, 42]. The inputs for determining the solar angles are given in degrees. The solar altitude and azimuth angles given in Equations (B.7) and (B.8) can be used to determine the position of the Sun [40].

$$a_S = \sin^{-1}\left(\cos(\phi_0)\cdot\cos(\theta_L)\cdot\cos(\lambda_s) + (\cos(\phi_0)\cdot\sin(\theta_L)\cdot\cos(\delta) + \sin(\phi_0)\cdot\sin(\delta))\cdot\sin(\lambda_s)\right) \tag{2.2}$$

$$A_S = \tan^{-1}\left(\frac{-\sin(\theta_L)\cdot\cos(\lambda_s) + \cos(\theta_L)\cdot\cos(\delta)\cdot\sin(\lambda_s)}{-\sin(\phi_0)\cdot\cos(\theta_L)\cdot\cos(\lambda_s) - (\sin(\phi_0)\cdot\sin(\theta_L)\cdot\cos(\delta) - \cos(\phi_0)\cdot\sin(\delta))\cdot\sin(\lambda_s)}\right) \tag{2.3}$$

The flow chart for determining the Sun's position with the inputs presented in Appendix B, is shown in Figure 2.5 [43].

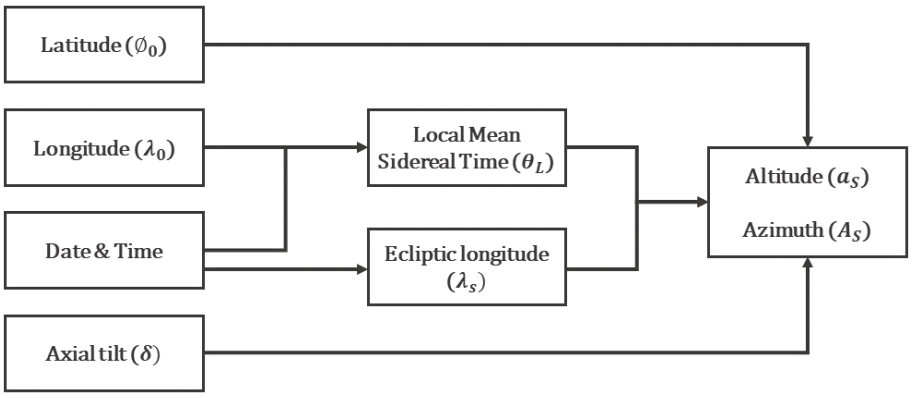

Figure 2.5: Flow chart for determining the position of the Sun, after [43].

After having obtained the position of the Sun for a specific time and day of the year, the solar position can be visualized in the sky dome using the obtained sun angles, a_s and A_s. A sky dome, visualized as a three-dimensional representation in Figure 2.4, can be converted into a two-dimensional projection for analysis of shading and sky component behaviour, which is known as an orthographic projection [44]. For an orthographic projection, the altitude and azimuth values are extended outward onto a surrounding vertical cylinder. In contrast, the polar projection entails the downward projection of these values onto a circular plane. Figure 2.6 illustrates both projections for a free horizon.

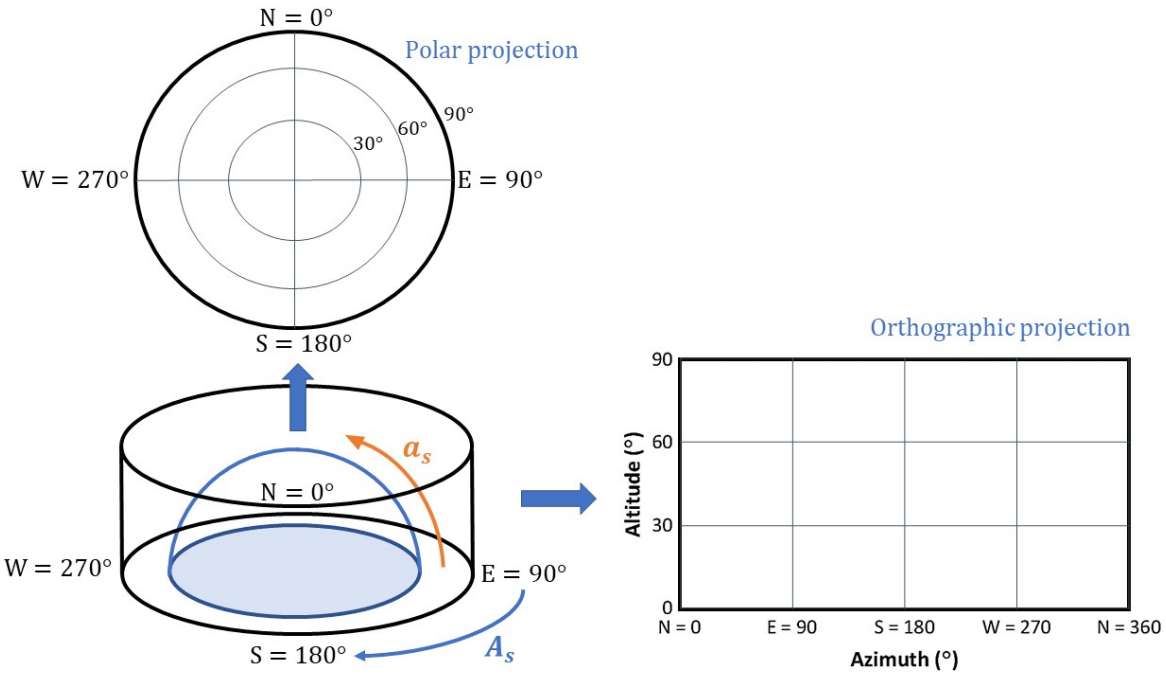

Figure 2.6: The sky dome (with an azimuth of 360° and altitude of 90°) projected on a circular plane, known as the polar projection, and vertical plane, known as the orthographic projection, after [44].

A free horizon implies no obstructions are visible in the surrounding environment. The conversion from 3D to 2D yields a difference in shape, which introduces errors due to the differences in perspective projection between the two representations. In a research conducted by Calcabrini [45], the variations in the problem geometry are considered acceptable. Furthermore, a weighted View Factor (VF) approach corrects the discretization of the projection, which is explained in more detail in Section 2.3.5.

2.3.2. Solar irradiance models

The position of the Sun directly influences the amount of solar energy received at a particular location on Earth [40]. Solar irradiance models can be applied to determine the amount of solar irradiance incident on a solar

panel. Different irradiance models assess the amount of incident solar irradiance on a PV panel. This can be done using (optical) irradiance modelling techniques [46]. The three most common irradiance models used are transposition models, view factor models, and ray-tracing models [46].

- ***Transposition models*** calculate the amount of solar radiation incident on a surface at a specific location based on direct, diffuse, and reflected irradiance values [40]. The Perez Sky model is an example, as it uses empirical and statistical models to estimate radiation that reaches a surface [47].
- ***View factor models*** determine the amount of radiation exchanged between two surfaces in space, where this can either be a random sampling (using a Monte Carlo simulation) or finite element analysis (using numerical methods) [46]. In a study by Sönmez et al. [48], a fast and accurate view factor estimation method was developed based on ray-casting, also known as backward ray-tracing, which implies rays emitted from the PV panel back to the sky using evenly distributed rays in all directions.
  - *BIGEYE* (BI-facial Gain and Energy Yield) is TNO's in-house developed modelling software whcih can accurately predict the incident light and intensity resulting in the calculated energy yield for bi-facial PV systems [49]. The BIGEYE application is used for static PV systems and utilizes a 3D view factor approach to determine the amount of irradiance. It considers a triangular mesh refinement required to accurately compute the view factors between the ground or diffuse reflector and the PV sheds [49].
- ***Ray-tracing models*** simulate the behaviour of light rays in a virtual environment. In most cases, this is the most computationally intensive yet most accurate approach. In a research study by Santbergen et al. [50], a 2-phase ray-tracing modelling method was created for a PV panel that has a complex geometry or is partially shaded using sky and sensitivity maps. To determine the PV cell's sensitivity to light, it uses the ray-tracing simulation software LightTools, which is based on a Monte Carlo approach. This approach is computationally efficient as it effectively disentangles the weather and irradiance data stored in the sky map from the information concerning the geometry and optical properties of the PV panel and its surroundings, which is preserved in the sensitivity map [50].

The decision for the most suitable irradiance model used in this work is further elaborated in Section 3.4.4 in Chapter 3.

2.3.3. Computation of solar irradiance

The solar irradiance incident on a PV panel is divided into three components: direct, diffuse and reflected [40]. By combining these three components, the total incident irradiance (G_{tot}) can be computed.

Direct irradiance G_{dir}

The direct irradiance component (G_{dir}) represents the beam element of solar radiation directly derived from the Sun. Direct irradiance on a PV panel is given by the following Equation (2.4) and the angle of irradiance (AOI) is defined in (2.5):

$$G_{\text{dir}} = DNI \cdot \cos(AOI) \cdot SF \tag{2.4}$$

$$\cos(AOI) = \sin(\theta_M)\cos(a_S)\cos(A_M - A_S) + \cos(\theta_M)\sin(a_S) \tag{2.5}$$

Where DNI is the Direct Normal Irradiance and AOI is the angle of irradiance, which is the angle between the normal of the PV panel and the direct component of the sunlight, given in radians. In this work, a horizontal PV panel is assumed, where the module tilt is $\theta_M = 0°$. Substituting this into the Equation above, the remaining factor for the computation is reduced to cos(AOI) = sin(a_s), where only the altitude of the Sun is relevant. The azimuth of the Sun (A_S) and solar panel (A_M) do not make a difference as the PV panel is assumed flat. Furthermore, the SF is the Shading Factor, which is a time-dependent binary function defined in Equation 2.6:

$$SF(t) = \begin{cases} 1 & \text{if the sun is visible,} \\ 0 & \text{if the sun is blocked,} \end{cases} \tag{2.6}$$

where the blockage of the Sun can be a result of the Sun being below the horizon ($a_S < 0$) or due to a nearby obstruction.

Diffuse irradiance G_{diff}

As sunlight travels through the atmosphere, it undergoes partial scattering, resulting in the reduction of the intensity of the direct beam component [40]. On the other hand, scattered light will reach the Earth's surface as diffuse light. This relates to the second component, which represents the diffuse irradiance (G_{diff}) and arises from the surrounding sky. In this work, a uniform diffuse model assumes incoming diffuse radiation

comes equally from all directions in the sky. To determine the diffuse irradiance component, different types of irradiance models use three components, which are the isotropic, circumsolar, and horizon brightening light components [51]. Several irradiance models estimate the diffuse irradiance with each approach, ranging from the Hay and Davies diffuse model to the Perez sky diffuse model [52]. In this work, the Perez model is employed to compute the diffuse solar irradiance component. This model is selected as it is more advanced by encompassing additional input variables such as the angle of irradiance (AOI) and air mass (AM), setting it apart from models such as Sandia and Hay and Davies [47]. The diffuse irradiance is computed using Equation 2.7:

$$G_{\text{diff}} = G_{\text{iso}} + G_{\text{cir}} + G_{\text{hor}} \tag{2.7}$$

Where the isotropic, circumsolar and horizon brightening light components are given as follows:

$$G_{iso} = DHI \cdot SVF \cdot (1 - F1) \tag{2.8}$$

$$G_{cir} = DHI \cdot F1 \cdot (A/B) \cdot SF$$
$$A/B = max(0, cos(AOI))/max\,(cos(85), \sin\,(a_s)) \tag{2.9}$$

$$G_{hor} = DHI \cdot F2 \cdot \sin\,(\theta_m) \tag{2.10}$$

Where DHI is the Diffuse Horizontal Irradiance, SVF is the Sky View Factor, and F1, A, and B are the empirically determined Perez coefficients where the calculation steps for these components are given in Appendix C. The A/B ratio represents the ratio between the non-uniformly distributed diffuse radiation across the sky (A) and the isotropic portion, which is the uniformly distributed radiation from all directions in the sky (B) [47]. The time and distance with respect to the Sun are included in this calculation. The three diffuse components are visualized in a sky dome, which is shown in Figure 2.7

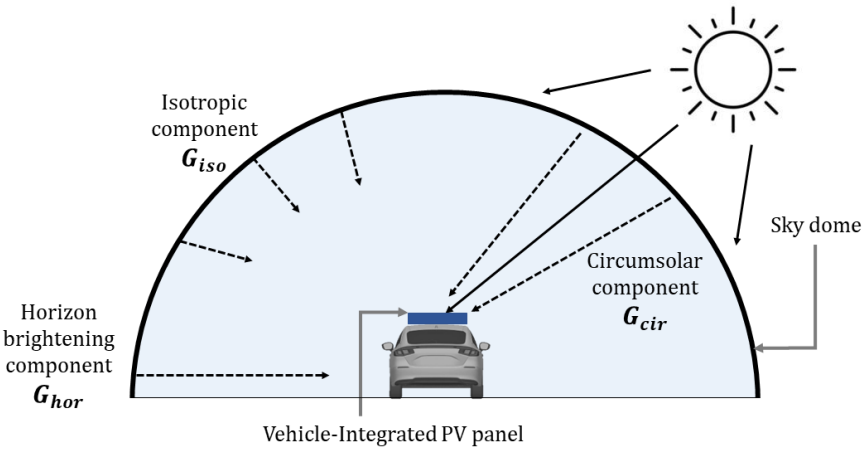

Figure 2.7: The three diffuse irradiance components (G_{iso}, G_{cir} & $_{hor}$) visualized in a sky dome, after [51].

The horizon brightening component, visualized in Figure 2.7 and given in Equation (2.10), only has a slight effect when the obstructions that constitute the horizon profile are very low and distant from the PV panel. As for a more obstruction-dense environment, such as an urban area, the buildings are closer to the PV panel, and therefore, the horizontal brightening effect is assumed to be negligible [45].

Reflected irradiance G_{refl}

The final component, which describes the irradiance on the PV panel, is the so-called reflected component, which is not to be confused with the reflected light from the PV panel itself. The reflected irradiance, G_{alb}, originates from the Earth's surfaces surrounding the solar panel, as expressed in Equation 2.11:

$$G_{refl} = GHI \cdot \alpha \cdot (1 - SVF) \tag{2.11}$$

where GHI is the Global Horizontal Irradiance, α is the albedo, which is the fraction of the GHI reflected by the ground, building facades, windows, and other obstructions, and the Sky View Factor (SVF) is the fraction of visible sky from which the module can receive diffuse radiation. In this work, the albedo value for computing the reflected irradiance is chosen as a fixed value based on the albedo for a medium building density in The Netherlands [11]. The SVF for a free horizon is computed as:

$$SVF = \frac{1 + cos(\theta_M)}{2} \tag{2.12}$$

Where θ_M indicates the module tilt. For a low SVF value, more reflected light from the environment is visible, whereas less diffuse light is incident on the PV panel.

Total incident irradiance G_{tot}
By combining the three irradiance components, namely direct, diffuse, and reflected irradiance, the total incident irradiance (G_{tot}) on the PV panel can be determined. The total incident irradiance is given by the Equation (2.13):

$$G_{tot} = G_{dir} + G_{diff} + G_{refl} \tag{2.13}$$

$$G_{tot} = DNI \cdot \cos(AOI) \cdot SF + DHI \cdot (SVF \cdot (1 - F1) + F1 \cdot (A/B) \cdot SF) + GHI \cdot \alpha \cdot (1 - SVF) \tag{2.14}$$

Where all irradiance parameters, GHI, DNI and DHI, are inputted in units of W/m^2.

Decomposition models. To determine the total incident irradiance and assess the reduction or increase in irradiance on solar panels, the DHI and DNI are necessary input variables. As most pyranometers or irradiance sensors measure only the Global Horizontal Irradiance (GHI), decomposition models can obtain the required DHI and DNI for irradiance calculations. There are different decomposition models which differ in complexity and accuracy. As the irradiance modelling software developed by TNO, BIGEYE, has incorporated Erbs [53], this decomposition model is applied in this research for conformity with the model and techniques. The Erbs decomposition model converts the GHI to DHI through empirical relationships between the global and direct clearness indices. The DHI is used as an input in the Perez Sky diffuse model in Equation (2.7) in Section 2.3.3. The DNI can be obtained by inputting the corresponding solar zenith angle (θ_z), GHI, and DHI values. Equation 2.15 shows the relation between these parameters [54].

$$GHI = DNI \cdot cos(\theta_z) + DHI \tag{2.15}$$

To obtain the required Global Horizontal Irradiance (GHI), different irradiance databases can be used to retrieve this data, which will be described in the following Section 2.3.4.

2.3.4. Irradiance databases

Different databases contain irradiance data and can be used to compute the total incident solar irradiance, given in Equation (2.14). Different databases include various sources, such as measured irradiance and irradiance data obtained through empirical models. The different irradiance databases used are outlined below.

- ***Measured irradiance data:*** Measured irradiance datasets consist of both historical irradiance, such as ground-based measurements obtained at meteorological weather stations, as well as experimental irradiance, collected from measurements such as irradiance sensors on a moving VIPV. Irradiance data is typically collected using irradiance sensors or pyranometers and consists of all-weather effects that have occurred in the past or during an experiment, such as rain, clouds, and clear sky days, which cause different irradiance values [12, 55]. Historical irradiance data is obtained at meteorological weather stations, such as Royal Netherlands Meteorology Institute (KNMI) in The Netherlands, where the global radiation is the measured component and given in J/cm^2 [55]. These datasets can be extracted and provide historical data on irradiance for a specific location and time, starting from every 10 minutes [55]. Moreover, experimental data consists of an experimental setup equipped with sensors to capture the irradiance levels. An example of an experimental irradiance dataset is from TNO, which provides data from horizontal irradiance sensors on a moving passenger car [12]. Both databases can be used as input to compute incident irradiance on a solar panel.

- ***Empirical model for irradiance data:*** Empirical weather models use historical weather and climate data, along with other relevant variables, to predict solar radiation levels [54]. Clear sky irradiance data can be used to estimate the incident radiation on the Earth's surface, assuming a cloudless condition across the entire sky dome. This estimation can be obtained using an empirically derived model and can provide a reasonably accurate result for a location without manually obtaining historical datasets [54]. The Ineichen and Perez clear sky model determines solar irradiation in clear sky conditions. The Ineichen and Perez empirical model parameterizes irradiance in terms of Linke climatological turbidity, which serves as a useful approximation for modelling the atmospheric absorption and scattering of solar radiation in cloudless atmospheric conditions [56]. The inputs necessary for this function are the set of coordinates (latitude and longitude), the time zone, and elevation above sea level. The stated inputs and empirical relations captured in the Ineichen and Perez function are used for the determination of the solar irradiance given as GHI, DNI, and DHI. This empirical model is used for comparison in this work, where the extraction is explained in Appendix F.

Free horizon. Ground-based meteorological weather stations, such as KNMI, and empirical models, such as the Ineichen-Perez clear sky model, both provide irradiance datasets for an unobstructed horizon [55]. A free horizon has a sky view factor (SVF) of 1, where Figure 2.6 in Section 2.3.1 shows an illustrative example. This contrasts with the experimental irradiance data collected by TNO, which involves irradiance measured on a moving passenger car surrounded by buildings and other obstructions. When surrounding obstructions block the visible area of the sky, it is indicated as a non-free horizon. As a result, the SVF value is equal to $\leq$1. To determine the exact SVF value for a non-free horizon, the following Section 2.3.5 introduces a weighted View Factor (VF) approach, which can determine the SVF value.

2.3.5. Sky View Factor (SVF) for a non-free horizon

The Sky View Factor equation, which was introduced in Section 2.3.3 by Equation (2.12), indicates the visible part of the sky dome for a horizon that is free of obstructions. This theoretical formula only depends on the module's tilt angle, θ_M. The module tilt (θ_M) is assumed to be 0° in this work, and therefore the SVF would imply to be 1. For a non-free horizon, this is not the case, and thus, a more complex approach introduced by Steyn is used to include surrounding obstructions [57].

View Factor (VF)

To determine the sky view factor (SVF), an understanding of the basic principles of the view factor (VF) is preferred. The VF is a geometrical factor that describes the amount of radiation exchanged between two surfaces in space [57]. This work describes the view factor from the PV panel to a point on the sky dome. To determine the view factor, the sky dome is discretized into several sky patches, which together form the surrounding sky. The angles are given in radians, given the use of trigonometric functions for radiation geometry [57]. In the VF Equation (2.16), this specific point on the sky dome can be seen as the differential sky patch, $d\Omega_{sky}$.

$$dF_{\text{PV}\rightarrow d\Omega_{sky}} = \frac{\cos\theta_1 \cdot \cos\theta_2}{\pi r^2} d\Omega_{sky} \tag{2.16}$$

where θ_1 and θ_2 describe the angles between two surfaces (in radians) and their corresponding normal vectors, and r is the radius between the surfaces. The variables are visualized in Figure 2.8. This visualization shows how the direction and length of the normal vectors relate to each other, formulated in Equation (2.16).

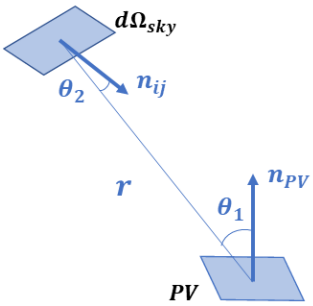

Figure 2.8: Visualization of the view factor from the PV panel to the differential sky patch $d\Omega_{sky}$, after [58].

By multiplying the VF with the radiant flux emitted by the differential sky patch, the contributed irradiance by the respective sky patch can be determined. The total diffuse irradiance (d_{diff}) on the PV panel can be obtained by repeating this for each sky patch on the sky dome. In the case of diffuse radiation, the Sun's position is not essential. The direct irradiance is calculated separately, as the DNI is not distributed over the sky dome but determines the amount of radiation from the concentrated point-like source, indicated as the Sun.
To define the mathematical Equation for the VF, an imaginary hemisphere with r=1 is considered around a point of interest, which in this work is the vehicle-integrated PV panel. The angle θ_2, between the normal of the sky patch and the vector that connects the center of the sky patch and solar panel, is always zero as the sphere is centered around the solar panel. For this case, $\theta_1 = \theta_Z$ is the angle between the normal vector to the PV panel and the vector that points to the sky patch. Taking this into account, the Equation 2.16 can be simplified to Equation 2.17:

$$dF_{\text{PV}\rightarrow d\Omega_{sky}} = \frac{\cos\theta_1}{\pi} d\Omega_{sky} \tag{2.17}$$

When comparing the VF values for different sky patches, it can be seen that the zenith region (higher altitude angles, where the zenith is $a_s = \frac{\pi}{2}$ rad) is of more importance than the horizon region (lower altitude angles, where a_s=0 rad). In Figure 2.9, this is shown, where the sky patches in the dedicated regions are given as orange dots, and the normal vectors indicate that for a sky patch on the horizon, the normal vectors are

perpendicular and therefore 0. Whereas for a sky patch at the zenith, the dot product equals 1. In summary, the relation between θ_1 and $a_s{}^{ij}$ is given as: $\theta_1 = \frac{\pi}{2} - a_s{}^{ij}$, in radians.

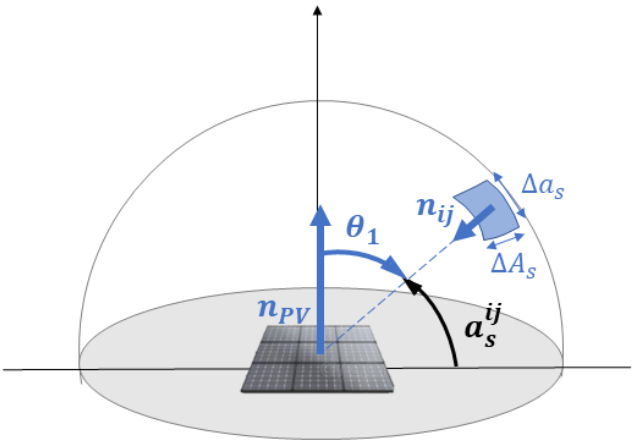

Figure 2.9: Sky patch, where the position is indicated by ij, visualized on the sky dome and the relation between the angles is: θ_1 + $a_s{}^{ij}$ = $\frac{\pi}{2}$.

When looking into the solid angle of a differential sky patch ($d\Omega_{sky}$), it can be given in spherical coordinates and is determined using the following Equation (2.18).

$$d\Omega_{sky} = \cos(a_S) da_S dA_S \tag{2.18}$$

Where a_s is the altitude angle, referred to as the angle starting from the horizon, and A_s is the azimuth. This demonstrates that the solid angle of the sky patch is independent of the orientation of the PV panel [58]. In the previous Equations, the differential solid angle was used. Whereas for creating a computational model, finite areas need to be used. To achieve finite areas, the sky dome is discretized into sky patches. Using the discretizations for the sky dome, Equation (2.18) can be represented mathematically as the following Equation (2.19).

$$\Delta\Omega_{sky} = \cos(a_S^{ij}) \Delta A_S \Delta a_S \tag{2.19}$$

In this Equation, the sky patch has a measurable size and is no longer a differential or infinitesimal area. The altitude angle to a specific sky patch, indicated as a_s^{ij}, is measured from the centre of the sky patch. The area of the sky patch is visualized in blue in Figure 2.9 at an altitude angle of a_S^{ij}.
For an orthographic projection of the sky dome, the area of each discretized sky patch is assumed to have the same dimensions given by ΔA_S and Δa_S. The dimensions are assumed constant for all sky patches, however, the solid angle changes depending on the altitude. It can be seen that for an increasing altitude, the $\Delta\Omega_{sky}$ value gradually decreases towards the zenith where it tends to be zero: $\cos(a_S^{ij} = \frac{\pi}{2}) = 0$ rad. This implies that the change in $\Delta\Omega_{sky}$ depends on the altitude angle (starting from the horizon). For the same altitude angle, the VF values will be similar for each sky patch in the same angular span, also known as the annulus [57]. The difference in VF values refers to the weight of each sky patch.
Using finite areas for the sky patches, indicated by position ij, the Equation (2.17) can be converted into Equation (2.20).

$$VF_{PV \to ij} = \frac{\cos\theta_1}{\pi} \cdot \Delta\Omega_{sky} \tag{2.20}$$

By combining Equation (2.19) with (2.20), the computation of the view factor from the PV panel to the sky patch with position *ij* ($VF_{PV \to ij}$) can be given and is presented in Equation 2.21.

$$VF_{PV \to ij} = \frac{\cos\theta_1}{\pi} \cdot \cos(a_S^{ij}) \Delta A_S \Delta a_S = \frac{\cos\theta_1 \cdot \cos(a_S^{ij})}{\pi} \cdot \Delta A_S \Delta a_S \tag{2.21}$$

where the first cosine in the formula, $\cos(\theta_1)$, has a maximum at the zenith and a minimum at the horizon. The second cosine, $\cos(a_s)$, is the opposite: a minimum is given at the zenith and a maximum at the horizon. The relation for the weighted view factors is obtained by multiplying these two factors. This can be visually interpreted as two cosines, where one is out of phase by $\frac{\pi}{2}$ (=$90°$), and the maximum for both is at $\frac{\pi}{4}$ (=$45°$). When computing all the view factors for a discretized sky dome, the view factor in each sky patch will have a different value. The weight of each view factor, where the position is indicated by ij, is in a range of 8E-7 up to 5E-5. The sky dome is discretized into sky patches for 90° altitude angles by 360° azimuth angles. This

results in a total of ($90° \cdot 360°$=) 32400 discretized sky patches, where the position is indicated by ij. Figure 2.10 shows an orthographic projection of a discretized sky dome with differing sky patch weights, indicating the range of values in the colour scale. It can be seen that around an altitude of 45°, the sky patch value reaches its maximum, regardless of the orientation of the solar panel. The explanation for this is the cosine of θ_1 goes to 0 when it is nearing the horizon (as $\cos(\theta_1 = \frac{\pi}{2}) = 0$), and the cosine of θ_1 goes to 1 when nearing the horizon (as $\cos(\theta_1 = 0) = 1$). When multiplying these factors together, as done in Equation (2.21), it can be seen that the two cosine functions are out of phase by $\frac{\pi}{2}$ rad, giving a maximum at $\frac{\pi}{4}$ rad. Figure 2.10 shows the representation of the weighted sky patch values, which have been determined using Equation (2.21). This value has been calculated using Equation (2.21) for each sky patch. The initial method introduced by Steyn in 1980 focuses on conventional fisheye photographs in polar projection and the SVF is computed based on the obstruction angle in each angular ring [57]. The methodology has been more recently refined in the work of Calcabrini et al. [46], where it used a two-dimensional view factor (2D VF) approach for an orthographic projection.

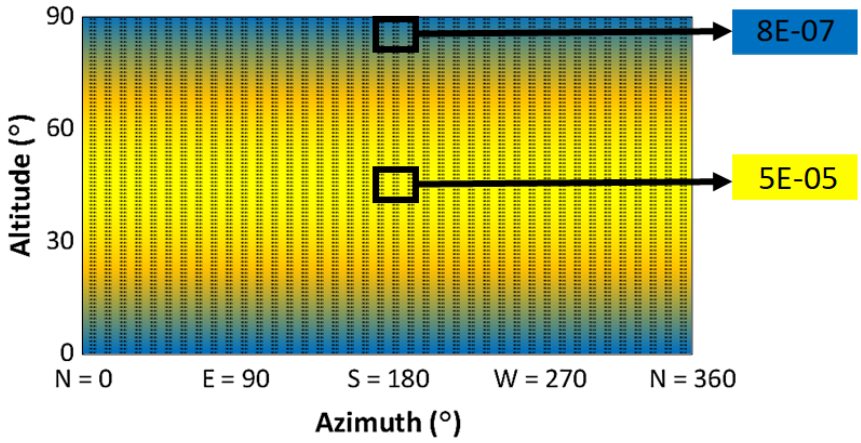

Figure 2.10: An orthographic projection of a discretized sky dome indicating the different sky patch weights.

Computation of the SVF

The sky view factor (SVF) is related to the view factor (VF) as it adds all the individually computed VFs to obtain one value that determines the amount of radiation a surface receives from the entire hemispheric environment. Equation (2.22) presents this relation.

$$SVF = \sum_i \sum_j VF_{\text{pv}\rightarrow ij} \tag{2.22}$$

The result is a SVF in the range of 0 and 1, where a SVF of 0 indicates the entire sky is blocked by its surroundings whereas a SVF of 1 implies a free horizon where all the sky patches are visible. The value for the SVF in a non-free horizon is applied to the irradiance calculation Equations (2.8) and (2.11) for the determination of the isotropic diffuse and reflected irradiance contributing to the calculated horizontal irradiance.

2.3.6. Changing environment

The surrounding environment changes throughout a route for a vehicle in motion. To estimate solar energy generation for VIPV, the prediction of incident irradiance is necessary [30]. The obstructions in the surrounding environment can cause the VIPV panel to be shaded, where the obstructions can be identified using different approaches. Ultimately, to extend and improve the shading loss assessment in EFM currently used within TNO.

BIGEYE, TNO's developed irradiance modelling tool, can consider the complex geometry surrounding the PV system [49]. However, manually plotting the surroundings is necessary, and due to the constant changes in the obstructions surrounding the PV system in VIPV, manually creating obstructions along a route is highly inefficient. Therefore, BIGEYE is not deemed suitable for mapping the surrounding environment. In this study, focusing on a moving VIPV context, a scalable approach is required to incorporate route-specific shading caused by obstructions.

Different approaches are commonly used to estimate solar irradiance for complex environments by considering the shading losses caused by obstructions. The two methodologies which consider the shading identification by surrounding obstructions are divided into two categories: (1) measurement approaches and (2) simulation modelling approaches.

Measurement approach

For experimentally analyzing the shading geometry for VIPV, solar irradiance sensors and a solar pathfinder are used. Solar irradiance sensors determine the incident irradiance on the VIPV panels while driving a specific route. By coupling a GPS receiver to the experimental setup, it is possible to collect accurate solar radiation data that includes the necessary location information. A solar pathfinder device captures a 360-degree fisheye image of the sky. It displays the fisheye images in polar coordinates and represents a hemisphere around a specific point in 2D, and all obstructions above and around that point are stored in pixels [16]. By filtering the captured image, the part of the sky that is visible and blocked by obstructions can be determined. This is visualized in Figure 2.11, where the Sun positioned in the white area indicates a SF of 1 and in the black area, a SF of 0. The approach of using fisheye images, where the images have been captured from the PV system's point of view, is common in different research studies [10, 16, 59].

Figure 2.11: An original fisheye image in grey-scale (left) and a filtered fisheye image indicating obstructions in black and the sky in white (right) [15].

To obtain the SVF, the fisheye images need to be decomposed into different colour scales for filtering through binarization of the acquired image. In Figure 2.11, the comparison between an original and binarized fisheye image is shown [15].

Simulation modelling approach

The second category refers to simulation modelling techniques enabling visualization of the surrounding environment. These modelling approaches involve simulating surrounding obstructions to determine which part of the sky is blocked, using available software and tools. Tools and software can extract building and height data from different databases. An example of useful software is the Geographical Information System (GIS), in which real-world geographic information can be modelled and reflected using spatial analysis tools which determine the solar irradiance based on the surroundings [17, 30]. Figure 2.12 shows a skyline graph in polar projection for a specified observer point within a building environment using GIS software [60].

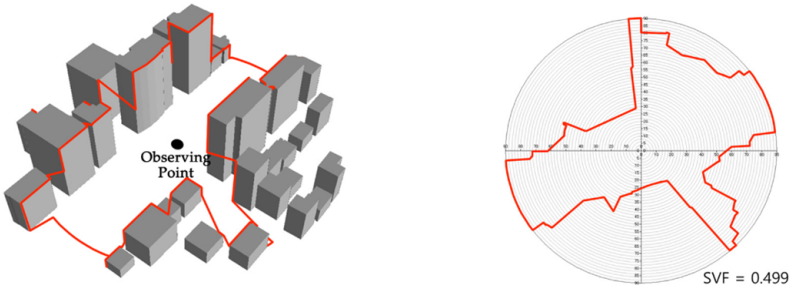

Figure 2.12: For a specified observer point within a building environment (right), a skyline graph in polar projection is generated using GIS software (left) [60].

Another approach is directly utilizing height data from a Digital Surface Model (DSM) [61]. In the work of Ferri et al. and De Jong et al. [18, 26], skylines are generated for a set of GPS coordinates through the extraction of elevation data from downloaded DSM data files. Finally, the third approach includes probability models, where a random distribution of shading objects is modelled to represent the environment [9, 62].

2.3.7. Categorized environments

The surrounding environment of a moving vehicle is important when estimating the varying shading losses. On a global scale, variations resulting from differences in latitudes and climate zones influence solar irradiation

levels. On a more localized level, variations in the surrounding environment, such as nearby obstructions (i.e. buildings and vegetation), further contribute to differences in solar irradiance. In a recent study conducted by Araki et al. [15], it is stated that the differences in VIPV energy yield mainly vary according to the shaded area in the local environment rather than the climate conditions or latitude [63]. Within this research, the shaded area is categorized into three zones and associated environments: (1) lightly shaded zone = open, (2) medium shaded zone = residential, and (3) deep shaded zone = urban. From an experimental study conducted by Araki et al. [15], typical sky images of the three zones have been captured and are represented in Figure 2.13.

Figure 2.13: Typical fisheye images of the three categorized environments: (1) open, (2) residential, and (3) urban [15].

The quantification of this result is visualized in Figure 2.14, where the calculation of the shading loss of each impact zone is given as a function of the latitude, in degrees (°) [64]. The shading correction factor, referring to the fraction of incident irradiance that is lost, is given as the ratio of the GHI for a horizontal car-roof in Figure 2.14.
The different categorizations are based on the surrounding obstruction density, with open, residential, and urban given as the grey, orange, and blue data points. These categories are presented in the same order in Figure 2.14. There is a visible correlation between the different shading zones [64]. The differences between the shaded zones, open, residential, and urban, are more significant than differences in latitude at a specific location on Earth [64].

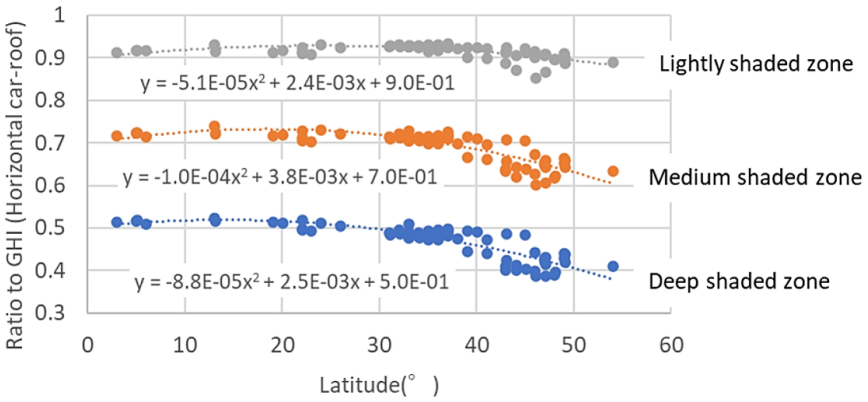

Figure 2.14: The fraction of incident irradiance indicated as a ratio to GHI (on the y-axis) given as a function of the latitude on Earth (on the x-axis), for all three categorized shaded zones [64].

From 2.14, the difference in ratio to GHI is more significant between the shaded zones compared to the differences in latitude. To illustrate, for a VIPV driving in an urban environment (deep shaded zone) around the equator, the ratio to GHI is approximately 0.5, whereas in The Netherlands, this ratio is around 0.4. When comparing this to differently shaded zones, the effect of latitude is considerably smaller, as the ratio to GHI is approximately 0.9 for the open zone (light-shaded zone) and remains 0.4 for the urban zone.
Furthermore, Araki et al. have categorized the shaded zones based on a land roughness indicator known as the sky view factor (SVF) [15]. The SVF determines what portion of the sky is visible and is obtained from the experimental study using the fisheye images [15]. The typical SVF values for open, residential, and urban zones are presented in Table 2.1 [15].

Next to the development of an improved shading assessment for TNO, which takes into account the location and time more specifically, the reverse approach to Araki et al. is investigated to determine whether a classified terrain map can give an approximation for the SVF [15].

Table 2.1: Typical SVF values for open, residential and urban zones [15].

	Open zone	Residential zone	Urban zone
Typical SVF values [-]	0.95	0.75	0.55

2.4. State-of-the-art approaches and values

In this Section, state-of-the-art studies that identify irradiance losses by applying various VIPV shading models to different cases are discussed. The impact of key factors that lead to irradiance losses in VIPV has yet to be researched. Most studies include one type of dataset, including the irradiance, time, and location data [14, 17, 18, 16]. To bridge the gap between the key factors which play a role in determining the incident irradiance in VIPV, this study investigates the reduction in incident irradiance more extensively by using different datasets, routes, and two different vehicle categories (public transport bus and a passenger car).

To consider the changing environment for a moving VIPV, studies have employed different methods, which include experimental studies or digital simulations [10]. In a comparative study by Keijzer [65] and Baek et al. [10], various modelling techniques were applied to compare the experimental and simulated approaches for identifying surroundings. Keijzer [65] compared SVFs derived from a simulation approach utilizing height data from a Digital Surface Model (DSM) and fisheye images from a static pyranometer across different locations. The differences between simulated and experimental SVFs were consistently below 3%. In a more recent study, Baek et al. [10] examined annual mean shading factors by comparing a manually created 3D model, based on land use and height maps, with the experimental use of fisheye images. The differences in mean shading factors between these two approaches ranged from 1.4% to 2.8%, varying by month. These comparative studies demonstrate minimal differences in SVF and yearly average SFs between simulation and experimental methods. Therefore, the values of both approaches are compared.

Furthermore, different studies have examined the yearly shading losses for VIPV by considering different irradiance and location datasets. A study by Brito et al. [30] employs a 3D modelling technique to estimate the shading losses using historical irradiance data and including the surrounding obstructions focused on a case study for the area of Lisbon, Portugal. The findings indicate an estimated annual average shading loss of 10% during the summer months and approximately 50% during the winter months. In this study, the height of vehicles has been neglected, which is estimated to represent a 5% underestimation of the solar potential. Another study by Cobbenhagen [11], for which the TNO shading assessment is based on [25], inputs historical KNMI irradiance and location data for Woensel, The Netherlands. In this study, a yearly average shading loss of 27% for a passenger car is determined, where the shading losses vary up to 54% in December and 23% in June.

Moreover, various studies have highlighted a correlation between SVF and incident irradiation. In a study by Robinson [66], the SVF can serve as an irradiance indicator in areas with high diffuse irradiance. A more recent study by Calcabrini has verified this [45], which identifies a strong relation between diffuse isotropic and SVF in complex and urban environments. In addition, Araki et al. [15] have categorized environments, open, residential, and urban, based on a typical sky view factor (SVF).

Finally, as this work focuses on The Netherlands, comparable studies The PV potential of Dutch highways as solar roads and the inland shipping fleet's PV potential have been assessed in the works of Ferri et al. [18] and De Jong et al. [67]. Ferri's research [18] involved simulating and determining yearly irradiation levels for Dutch highways, ranging from 295 to 1060 kWh/m^2/year. In De Jong's study [67], the simulated PV power was compared with experimental results for inland waterways in The Netherlands, showing a 6.15% difference for vessels with horizontal PV (0° tilt) across 33 data points.

In summary, the literature demonstrates the importance of considering the surrounding environment in VIPV, as annual shading loss values can vary based on key factors. For example, for Dutch highways the incident irradiation can result in a maximum difference of up to (1050-295 kWh/m^2/year =)765 kWh/m^2/year. The large differences in irradiance highlight the importance of a more accurate VIPV shading loss assessment, considering the key factors causing irradiance losses.

2.5. Research questions

This Chapter has delved into the three main factors influencing shading losses in VIPV: time, weather conditions and location. Additionally, this Chapter offers a comprehensive background and literature review by giving an overview of the current state-of-the-art models and research in this field. The research objective of this study is:

To improve TNO's current VIPV shading assessment by incorporating more variables into a new model and thereby contributing to a better estimation of the VIPV energy yield.

To fulfil the stated research objective, the following research questions are addressed:

1. **How to implement key factors causing shading loss to improve TNO's VIPV shading assessment?**

   The focus of this research question is to develop a model that can accurately and efficiently predict irradiance losses considering the three key factors causing shading in VIPV: location, weather, and time, which improves TNO's current shading assessment for a driving vehicle with integrated PV (VIPV).

2. **How to determine the quality of the model by validation?**

   This research question focuses on whether the developed model can accurately assess two different validation datasets by considering potential sources of error and variability.

3. **What are the shading losses caused by key factors based on two different case studies?**

   The last research question focuses on the shading loss results obtained from two different case studies by using different inputs based on the key irradiance loss factors, which are weather, location and time-dependent.

The first question is addressed in the next Chapter 3. Followed by the second research question in Chapter 4. Finally, the last question is addressed in Chapter 6. In the final Chapter 8, the three research questions will be addressed in the conclusions.

3
Methodology

This Chapter evaluates different modelling approaches, followed by the chosen model, the necessary input data and the required methodology. Section 3.7 presents the workflow for the modelling methodology. Finally, Section 3.8 of this Chapter addresses the first research question: **how to implement key factors causing shading loss to improve TNO's VIPV shading assessment?**

3.1. Evaluation of approaches

Both measurement and simulation-based approaches are focused on identifying the environment surrounding the VIPV panel and are considered in this evaluation. In comparative research studies conducted by Keijzer and Baek et al. [10, 65], minimal differences in results between both approaches are demonstrated. In an experimentally-based approach, the weather, time and location are fixed as they depend on the circumstances of the conducted experiment. Moreover, fisheye images require on-site capture, which can be time-consuming and associated equipment can be costly [10]. In contrast to a simulation-based approach, where the location, time, and weather parameters can be modified without the need to take photographs in the field [68]. As this thesis work is conducted for two case studies, the ability to generate different outcomes within a given time frame is essential. As a result, it was decided to adopt a simulation-based modelling method.
This study compares simulation models based on environmental mapping techniques which can identify obstructions, drawing from state-of-the-art methods in prior research: a) probability models, where a random distribution of shading objects models the environment [9, 62]; b) GIS-based models, where geographical tools in the software enable identification of the surrounding environment [17]; c) DSM-based models, where the input is based on a height map of the area which defines the environment [14, 69].

3.1.1. Multi-Criteria Analysis (MCA)

As each simulation modelling method requires different techniques and software tools, a multi-criteria analysis (MCA) is conducted to evaluate the methodologies based on various criteria. MCA consists of a multi-step process and considers multiple factors with levels of importance or relevance [70]. The selected criteria are based on the discussed aspects in a comparative study by Baek et al. [10], where the frequent variability of shading in VIPV is highlighted. In this study, the necessity of a flexible and widely applicable approach is emphasized, as well as the need for accurately identifying the surrounding obstructions for a specific route [10]. As shading constantly varies in a moving VIPV [4], an efficient approach is necessary to be applicable for multiple routes and locations.
Moreover, the surrounding environment needs to be considered more accurately in contrast to one location correction factor used by TNO. Finally, the results should be regarded as reliable, and software tools should be easy to access, translating into a valid and transparent approach. The following criteria are applied for the MCA, aiming to identify a more accurate approach which identifies the surroundings along a road in VIPV: scalability, accuracy, validity, and transparency.

- **Accuracy**: The accuracy of a model focuses on representing various obstructions of all sizes and shapes, as they can block the Sun, causing shade on the PV panel. In a probability model used in a research study by Araki et al. [9], the model relies on a random placement of obstructions and is not route-specific, therefore indicating a low accuracy. The GIS- and DSM-based models consider the surrounding environment using topographical maps, which results in a higher accuracy than the current TNO shading assessment.
- **Scalability**: The scalability of a model depends on factors such as the number of software tools and steps needed to obtain results, which is related to the computation time required. As the location data can be extensive for a long route, the amount of data that needs to be processed should be done efficiently. Using probability and DSM-based models, an algorithm for retrieval can be created in programming software, making the extraction of data efficient in contrast to Geographic Information System (GIS) software tools, which require most operations to be done manually as each geospatial tool has a different

purpose [10]. In summary, the probability and DSM-based models are more scalable than the GIS-based models.

- **Transparency**: Open-source data is essential as it provides more insights into the conducted method. The usage of open-source data makes a model reproducible for future research. The requirement for a subscription to access specific tools in GIS can vary depending on the software and the tools being utilized and is, therefore, not always open-source. This contrasts the probability and DSM-based models, which use open-source programming software such as Python.
- **Validity**: The validity of a model relates to the possibility of evaluation and comparison with other datasets, techniques, and models, ensuring the reliability of the model as a whole. In the case of probability models, validation is less applicable as it relies on a random distribution of shading objects and can, therefore, not be compared with a specific route. The GIS- and DSM-based models can be compared using Google Maps and Street View for the particular location of interest.

The stated criteria are assumed to be equal in terms of importance. The evaluation of the three simulation approaches has been summarized in Table 3.1.

Criteria	**Modelling approaches**		
	Probability	GIS-based	DSM-based
Accuracy Chosen input data	No	Yes	Yes
Scalability Limited manual operations required	Yes	No	Yes
Transparency Open-source software/tools	Yes	No	Yes
Validity Validation with available data	No	Yes	Yes

Table 3.1: Comparison of three modelling approaches using multi-criteria analysis.

3.2. Chosen approach

In this study, the four criteria, accuracy, scalability, transparency, and validity, are chosen as the most valuable given the preferred outcome for simulating obstruction shading within a given time frame while still improving TNO's shading assessment by introducing a more efficient and accurate model. Based on the evaluation provided in Table 3.1, the DSM-based model anticipates all desired outcomes concerning the four criteria and is, therefore, the most favourable method.

3.3. Modelling input data

The DSM-based simulation model is the base of the methodology, and to simulate the VIPV shading loss for a specific route, weather and time, the following inputs are necessary:

- **Study area**, where the location GPS coordinates are important. The GPS coordinates are a collection of singular or multiple sets of latitude and longitude values of the examined area.
- **DSM data**, providing obstruction elevation profiles in a digital form.
- **Time and day of the year**, to determine the position of the Sun, which is crucial for irradiance calculations.
- **Irradiance data**, which can be measured, estimated or calculated depending on the desired outcome and available databases.

The listed inputs are variables that can be retrieved from different databases. The study area is the initial input requirement, where the remaining three inputs are based on key factors causing shading loss. These databases and decisions related to the input datasets are further explained in this Section.

3.3.1. Study area

Each route is unique concerning the surrounding environment and obstructions. In this study, a geospatial planning software named ArcGIS Pro is used for identifying the route. To examine a route, multiple GPS coordinates are obtained along a route. In this study, the GPS coordinates used for analysis are referred to as 'road survey points' and marked as tracker points in ArcGIS Pro. ArcGIS Pro allows users to generate GPS coordinates or input datasets containing GPS coordinates. The workflow for generating and extracting the XY-coordinates is given in the ArcGIS manual in Appendix D.

There are two ways to obtain GPS data for the road survey points: time-based (temporal) or distance-based (spatial) methods. Time-based points are distanced by a specific frequency or time, for example, every 1 second on the road, thus considering vehicle speed influenced by factors such as driving behaviour. A higher density of points will result from a decreased vehicle speed. The other option is distance-based points, created using the same distance between each road survey point. In this method, the 'stop and go' behaviour is filtered, as there is no real-time data incorporated. In this study, the road survey points are plotted based on distance as it is a complex task to predict the duration of road factors, such as traffic lights or traffic jams for a specific route. The difference in results for using time-based and distance-based road survey points are presented in a sensitivity analysis in Section 4.3.2.
Moreover, the usage of topographical web maps is a powerful tool as it enables the loading of digital data, such as roadways, into an existing file for further analysis [61]. ArcGIS Pro can display and overlay these maps, as shown in Figure 3.1.

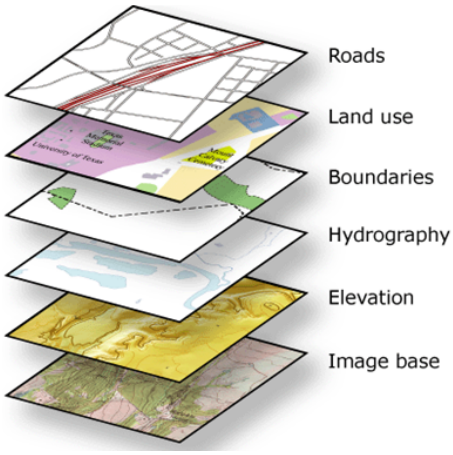

Figure 3.1: Topographical maps containing different information and data for analysis purposes [61].

Topographical maps can be retrieved from sources that publish reliable and consistent statistical information. Examples of valuable datasets are from Dutch open-data sources such as Centraal Bureau voor Statistiek (CBS), Rijkswaterstaat (RWS), and Actueel Hoogtebestand Nederland (AHN) [71, 72, 73].

3.3.2. Digital Surface Model (DSM)

A Digital Surface Model (DSM) of the specified area is required to identify surrounding obstructions along a road. A DSM represents the elevations on the Earth's surface, encompassing both organic and artificial structures, such as buildings and artificial objects positioned upon it [74]. The map typically represents a grid containing cells or pixels, with each cell holding a value that indicates the height (Z-value) of the corresponding location specified by XY coordinates. In The Netherlands, PDOK is the open-source geodata platform that contains height data in raster format [73]. The height data originates from Actueel Hoogtebestand Nederland (AHN), a digital map database for The Netherlands. In AHN, the DSM height data has been retrieved using the LiDAR technique. LiDAR (Light Imaging Detection and Ranging) is a remote sensing technology that uses laser pulses from an aircraft to measure the distance between the sensor and the Earth's surface [74]. LiDAR measurements require clear skies beneath the aircraft, as the measurements cannot penetrate through overcast clouds [74]. In addition, the terrain should be free from flooding and not covered by snow or hail [74]. The laser pulses return point cloud data, and by processing the data, a raster grid is created. In Figure 3.2, a schematic representation of the LiDAR scanning system is shown, where the Figure indicates how multiple laser pulses recreate the contour of a tree. Due to a particular scanning resolution, not every tree branch can be considered. Only the maximum height of the obstruction is considered.
The LiDAR data in a raster grid of 0.5x0.5m^2 is the highest resolution in The Netherlands. The AHN DSM dataset is organized into several map sheets, in total over 1 TB in size, for the entire area of The Netherlands [74]. Each sheet of a bounded area holds XYZ data and can be saved in GeoTIFF format, a TIF file. This format is helpful for analysis as it contains the coordinate system, projection, and spatial reference for the position on Earth [74]. The map sheets are visualized in Figure E.1 in Appendix E. In addition, the different data collection years for the AHN3 dataset are given in Figure E.2 in this Appendix.

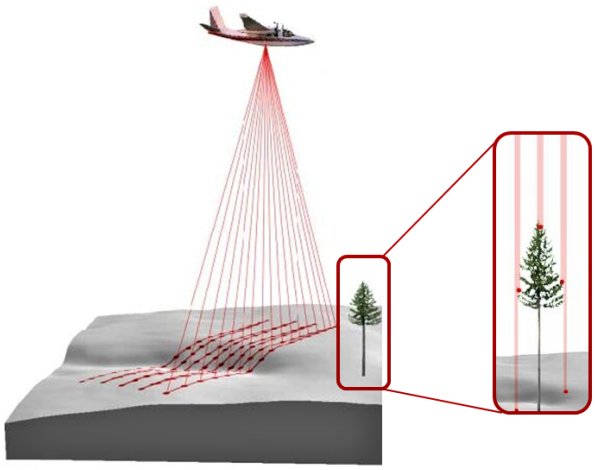

Figure 3.2: Schematic visualization of the LiDAR scanning approach, after [75].

3.3.3. Time and day of the year

The time and day of the year is a crucial input to determine the position of the Sun [42]. The Sun's position is indicated using a_S and A_S. The calculation of the sun angles, which determine the position, is performed using the required computations provided in Appendix A and B. The required input is the Local Clock Time (LCT), specifying the time and day of the year to the second precision for accurately determining the position of the Sun.

3.3.4. Irradiance

As presented in Section 2.3.4 in Chapter 2, different irradiance databases include various datasets. The irradiance datasets considered in this work are: historical KNMI irradiance, experimentally measured irradiance, and the clear sky irradiance model by Ineichen and Perez [55, 12, 54]. The experimentally measured irradiance, through measurements conducted by TNO, include surrounding obstructions, where the SVF $\leq$ 1. This irradiance data is used for validation purposes of the model, presented in Chapter 4. In contrast, the historical KNMI data and clear sky irradiance data are obtained or empirically determined for a free horizon, implying an SVF=1. These irradiance datasets are used for simulating the incident irradiance within the case studies. The historical KNMI irradiance can include all weather effects, from clear sky days to a day with high cloud cover. KNMI assesses the measure of cloud coverage and records it for that specific day. The cloud coverage measure is within a range of 0 to 9 okta, where 0 indicates a (near-)clear sky, and 9 is where the sky is completely covered by clouds, which is known as overcast [55]. When using the empirical Ineichen-Perez model, the solar irradiation is determined for clear sky conditions. This model helps isolate the shading impact caused by weather effects, such as clouds and rain.
Improving shading loss estimation in VIPV involves inputting irradiance data for various conditions, from clear to overcast skies, rather than relying on one input dataset in TNO's current approach. This ensures more accurate predictions, preventing the risk of over- or underestimation associated with a single shading value. The inputted irradiance datasets are specified in the case studies in Chapter 5.

3.4. Modelling methodology

The choice of a suitable modelling approach is dependent on the desired resolution. In the case of VIPV, where the amount of incident irradiance fluctuates throughout a route, an accurate yet scalable model is essential. Concerning the existing modelling approaches, this Section focuses on modifying and adapting existing methods to suit specific modelling needs.

3.4.1. Horizon scanning algorithm

It is essential to consider the surrounding obstructions, such as buildings and trees, to determine the degree of shading [10]. The Actueel Hoogtebestand Nederland (AHN) dataset contains height data in raster format, as explained in Section 3.3.2. This height data is retrieved in a GeoTIFF format, which can be done manually by extracting the map sheets for an area of interest. In the thesis of Ferri [76], an alternative to the manual operation was conducted by superimposing the DSM data on the Nationaal Wegenbestand (NWB) map. However, this is not feasible for different types of routes or applications, as explained in a more recent study by De Jong et al. [26], which required an AHN DSM dataset of waterways in The Netherlands containing a

total storage capacity of 656 GB.
In this thesis work, an improvement to this aspect of the model is made where no manual extraction of height data is necessary, which improves the model's scalability, as it results in a quicker operation. The new contribution directly extracts height information through a Web Coverage Service (WCS) [77]. The WCS technique does not require any manual operation of downloading an AHN tile, as it utilizes a URL link that stores configuration data in a structured XML file and extracts information through this file. Through the installation of the ***OWSLib*** library in Python, a GetCoverage request can be made [77]. Utilizing the GetCoverage request, the GPS coordinates are inserted to extract a bounded section of the height map for a specific location. The GetCoverage request requires various sub-settings, such as specifying location boundaries, selecting a coordinate system, and adjusting resolution [77]. The variable settings of the WCS service are presented and explained in Appendix G.
The WCS request establishes a connection to the AHN server and extracts data. The obtained height data is used as an input for generating a horizon profile. The base of this algorithm was a method established by Keijzer [65], which converts LiDAR data to a horizon profile. This work gives an observer point a certain height above the AHN grid. The observer then starts scanning one range of azimuth angles, called a 'slice', to obtain the data point with the most significant altitude. The corresponding maximum altitude angle (Δa) is then saved for the given slice. This process is repeated for *n* amount of slices for a full azimuth range of 360°. The angle in the horizontal plane indicates the azimuth slice angle (given as $\Delta\theta$ in degrees) is defined as $\frac{360}{n}^\circ$ [65]. Figure 3.3 gives a visual representation of the horizon scanning principle from the top and side view, where both angles (Δa and $\Delta\theta$) are shown. Some data points in the side view representation are visualized as bars showing the corresponding height for illustrative purposes.

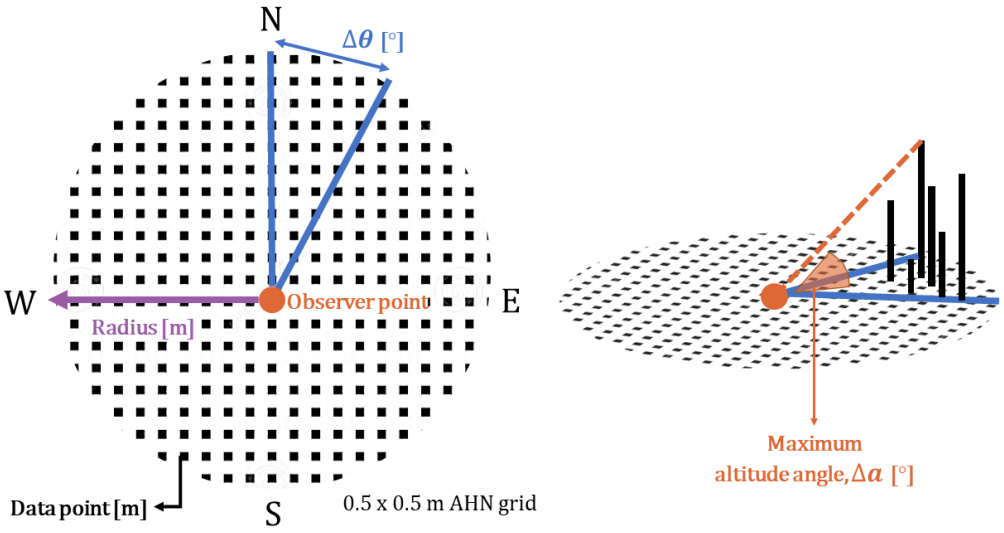

Figure 3.3: Left: top view of a height map in a grid format with the XY observer point indicated in orange, Right: side view of a scanned maximum altitude from the observer point, after [65].

The horizon skyline profile is projected on a 2D orthographic figure with the maximum altitude on the y-axis (from 0 to 90°) and the azimuth on the x-axis (from 0 to 360°). Figure 3.4 gives an example of a skyline representation.
An algorithm is created in Python to repeat this workflow for each observer point, which is explained in Appendix G. In short, a repetitive elevation scanning process is performed for each $\Delta\theta$. The main advantage of this algorithm is that it is an automated approach, and no manual modelling is needed, saving labour and time.
Considering the use of the WCS request, which performs actions directly via a URL in the background, the technique must be verified. By taking these steps and ensuring that the other horizon scanning steps remain valid, a verification with geometry calculations and ArcGIS is conducted, where the analysis and results of the verification are presented in Appendix H. Using Google Street View and identifying a solid obstruction along a data point of which the height can be estimated and the distance and direction are known, the deviation in height with the digital skyline representation is approximately 2.25%. This deviation, as stated in the Appendix, can be due to different factors. Given the small difference and the obstructions and contour in the results align, the improvement to the model is verified as a whole.

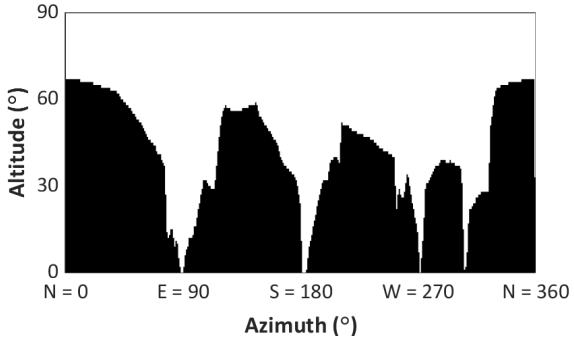

Figure 3.4: An example of an orthographic skyline profile for a road survey point in the residential area of Echt, The Netherlands.

3.4.2. 2D view factor (VF) model for SVF determination

After obtaining the skyline profile in a 2D orthographic representation, SVF can be determined. In a study conducted by Sönmez [48], a model for determining the sky view factor using a view factor model was presented. Calcabrini et al. refined this modelling method [45], making it applicable to a PV system in a complex urban environment. This is known as a 2D view factor (VF) model, as the rays are emitted from the PV panel back to the sky using evenly distributed rays in all directions [45]. Each sky patch gets a weight assigned according to its position. This methodology is previously explained in Section 2.3.5, Chapter 2. After the discretization of a sky dome and assigning the corresponding weights to each sky patch (visualized in Figure 2.21), the representation can be combined with the obtained skyline profile (visualized in Figure 3.4). The combination is given in Figure 3.5.

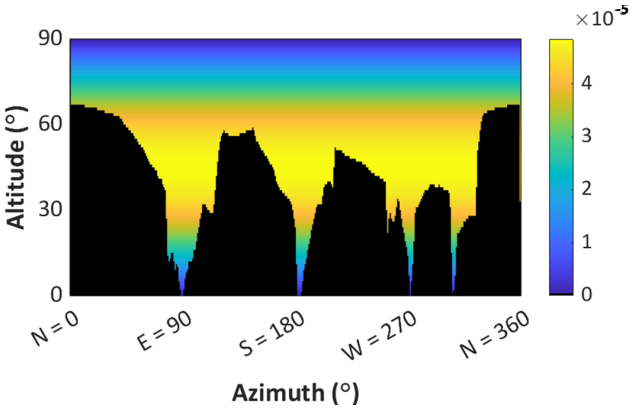

Figure 3.5: An example of an orthographic skyline profile combined with sky patch weights for calculating the SVF value.

The background knowledge for the 2D VF model is obtained from one of the assignments in the PV systems course, created by Calcabrini [43]. To filter out the sky patches that are not visible due to surrounding obstructions, a binary representation of the sky visibility is performed. The binary representation, resulting in 1 if the sky is visible and 0 if blocked, is known as a shadow map. This shadow map is an enlarged version as presented in Figure 3.6.

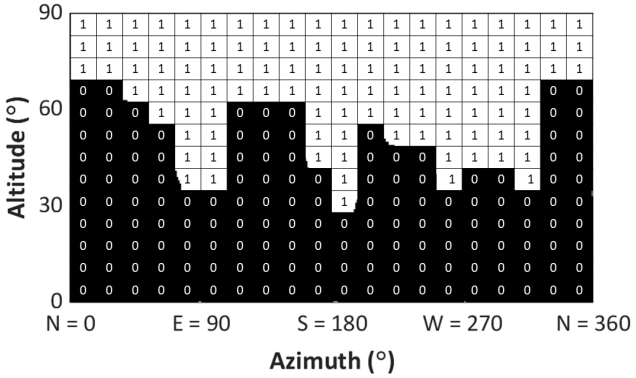

Figure 3.6: A binarized shadow map from the skyline profile in Figure 3.4, where the angular resolution is enlarged for illustrative purposes< after [46].

As the azimuth step size is 1° and the altitude angles are rounded to a whole number, the resolution of the shadow map in this work is chosen to be 1°. By multiplying the shadow map, presented in Figure 3.6, with the sky patch weights, all individual VFs can be determined. By summing the individual VFs for the discretized sky dome, the SVF value can be determined. Following the computation given by Equation (2.3.5). This is a unique value for each road survey point. By implementing a repetitive code, using a for loop in MATLAB, this process is continued for multiple points where the skyline profile is given.
The initial method introduced by Steyn in 1980 focuses on conventional fisheye photographs in a polar grid [57]. The SVF is computed based on the obstruction angle in each angular ring [57]. The methodology can be reproduced in an algorithm using the explained 2D VF modelling method. The 2D VF methodology is defined in this work as the determination of an obstruction from a line of sight from an observer's point of view [69]. The summation of all visible view factors of the sky patches, which are not blocked by an obstruction, form the SVF together as presented in Equation (2.22).

3.4.3. Sun position calculation for SF determination

Next to the SVF, the Shading Factor (SF) can be determined using the given skyline profile. In a dynamic situation such as VIPV, the solar altitude and azimuth (a_S and A_S) need to be determined for a series of specified locations which together describe a route. Using the JD sun position calculation, explained in Appendix B, the solar angles can be determined by specifying the time, to the second precision, and day of the year for a series of GPS coordinates. The solar azimuth (A_s) is rounded to the nearest integer to be able to compare it with the same skyline azimuth range, which is rounded in the horizon scanning algorithm to a round number ($A_{skyline}$). By looking at the same azimuth range, the altitude of the sun and skyline of the specified observer point are compared through a logical test to determine the SF. The Equation is a binary function, represented in Equation 2.6, where the SF is assigned '1' if the sun is visible and not blocked by the obstruction, and a SF '0' is applied when the skyline blocks the sun. The logical test for determining the SF is obtained using Equation (3.1) [45].

$$\text{SF } (A_{\text{S}}, a_{\text{S}}) = \left\{ \begin{array}{ll} 0 & 0 < a_{\text{S}} \leq a_{\text{skyline}}\,(A_{\text{S}}) \\ 1 & \text{otherwise} \end{array} \right\} \tag{3.1}$$

3.4.4. Irradiance model

After having obtained the SVF and SF for a road survey point, the final step is the application of an irradiance model to determine the irradiance losses. In Section 2.3.2, the three standard irradiance models have been introduced: transposition models, view factor models, and ray-tracing models [46]. In the case of a dynamically moving PV system integrated into a vehicle, decoupling the surrounding environment and irradiance helps reduce computational time. Therefore, a ray-tracing simulation method, although efficient for stationary objects, would be too computationally intensive as the ray-tracing simulation needs to be redone every time the surrounding changes [46]. In a study conducted by Sönmez and further refined by Calcabrini, the 2D VF approach which is proposed is a simplified version of a ray-tracing technique, considering the rays originate from the surface of interest [45, 48]. As explained in Section 2.3.5, this method includes the computation of a view factor from the solar panel to each sky patch, where the mathematical relation is shown in Equation (2.17). The advantage of this approach is the reduced computational time, as the ray-tracing simulation is decoupled from optical properties (such as reflectivity) and illumination conditions [46, 50]. This reduces the number of rays that need to be computed, and considering a horizon profile given in an orthographic 2D representation (presented in Figure 2.6 in Section 2.3.1), it is feasible to calculate the sky view factor (SVF) given this 2D VF model.

In summary, this thesis study uses a 2D VF model to determine the SVF and obtain the SF for a given time. Consequently, transposition models, such as the Perez sky diffuse model, are applied to simulate the total incident solar irradiance. By considering the key factors contributing to irradiance loss, the simulated irradiance can be used to obtain the varying shading losses.

3.5. Varying shading indicators

The base of this approach consists of using the DSM height data to obtain a 2D skyline representation of the surrounding environment, where the skyline method was initially proposed by Keijzer [65]. This is followed by the application of the approach by Steyn [57], which is further refined by Calcabrini et al. [45], to discretize the sky into 32400 sky patches to obtain a weighted sky view factor (SVF). Consequently, the SF is determined by overlaying the position of the Sun with the skyline profile. In this work, the SVF and SF are essential to compute the incident solar irradiance as they are substituted in Equation (2.14) in Chapter 2. These variables are referred to as the **varying shading indicators**, where the skyline profile and position of the Sun are

combined to determine the varying shading losses for VIPV through simulation of the incident irradiance. Figure 3.7 shows how the SF and SVF values relate to the obtained skyline. The black area indicates where obstructions are present, and the visible part of the sky is indicated in white. The SVF is a value within a range of 0 and 1, in contrast to the SF, which is a discrete value of either 0 or 1.

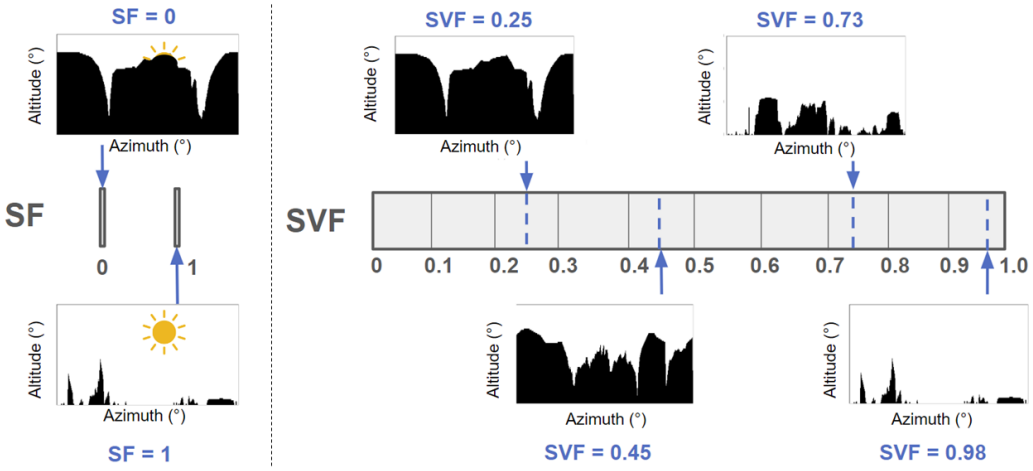

Figure 3.7: The relation between the skyline profile, which quantifies the obstruction density, and the varying shading indicators: SF (left) and SVF (right).

3.5.1. Discrete Shading Factor (SF)

As referred to in previous Sections, a SF of 0 indicates complete obstruction of the Sun. In contrast, a SF of 1 indicates no block. The shading factor is discrete, outputting either 0 or 1. This SF approach lacks detail for partial shading or movement across a panel, assuming a PV panel is uniformly shaded. This assumption is made to remain scalable for many routes while still enhancing TNO's current shading assessment with a route-specific approach.

3.6. Determination of the terrain types

This Section investigates the possibility of classifying terrain types for approximating the SVF value and, indirectly, the varying shading losses. The reverse approach has been studied in a paper by Araki et al. [15], where environments are classified based on SVF values obtained from fisheye images for a specific route. The categorization involves typical SVF values assigned to open, residential, and urban environments, showing that the shading losses are mainly affected by these environments rather than by the climate zone [15]. The typical SVF values are presented in Table 2.1 in Chapter 2. ArcGIS Pro can analyze and visualize datasets and maps indicating the topography. This study explores the feasibility of employing a topographical map to approximate the SVF and indirectly give a proxy of the shading loss for a vehicle with integrated PV.

The topographical map, which includes classified terrain types and relevant information about The Netherlands, is the Bestand Bodemgebruik (BBG) map acquired by CBS [78]. This map is a national 'land use' polygon map of The Netherlands. In this map, BBG identifies the predominant ground-level land use per region, referred to as terrain types [78]. As this is the most recent reference year in which the data is publicly available, the DSM data is aligned with the year of interest for a valid comparison. The collection of Algemene Hoogtekaart Nederland 3 (AHN3), using the LiDAR technique, runs from 2014 to 2019. It is, therefore, chosen to use this AHN data rather than the newest version to align with the map used for classifying the terrain types. The collection years for AHN3 are presented in Appendix E.
Within the BBG 2017 map, there are eight different terrains in which land use is classified. The digital map consists of contiguous, non-overlapping single-part polygons on a scale from 1:10.000, which results in the accuracy of the polygon geometry to be 2 meters [78]. The different terrains are subdivided into 38 categories. The eight different terrains, with categories and their identification codes (X), are the following [78]:

- **Traffic terrain**: railroad (10), main road (11), airport (12)
- **Built terrain**: residential (20), retail and hospitality (21), public (22), cultural buildings (23), business park (24)
- **Semi-built terrain**: construction (34) and industrial sites (30, 31, 33, 35)
- **Recreation terrain**: parks (40), sports ground (41), allotment garden (42), recreational grounds (43)

- **Agricultural terrain**: greenhouse farming (50), other (51)
- **Forest and open terrain**: forest (60), open dry natural terrain (61), open wet natural terrain (62)
- **Inland water**: lakes (70-74), recreational water (75), other waters, such as canals (76-78)
- **Outer waters**: sea (80-83)

In Figure 3.8, the BBG 2017 map is visualized for the area of Amsterdam.

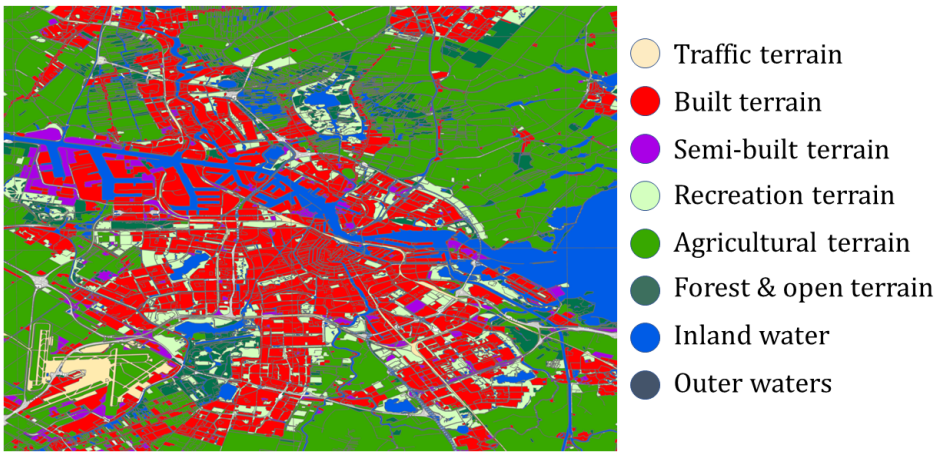

Figure 3.8: Bestand Bodemgebruik (BBG) map for the area of Amsterdam, indicated with the eight terrain categories in the legend (right) [78].

The BBG land use map is qualitative, as it categorizes land use and land cover based on different terrain types.
The terrain type classification is applied to one of the case studies, which includes all bus routes of Amsterdam, The Netherlands. This case study is chosen for analysis as it includes many routes and data points across different environments. For each road survey point along the route, different terrain types are observed within a 100-meter radius. Using the ArcGIS workflow presented in Appendix D, the terrain type constituted within the enclosed area can be extracted to determine the percentage share. This results in a database of differing percentages of terrains with the corresponding SVF value. By comparing the determined sky view factor (SVF) with the classified share of terrain type, an assessment can be made on whether a correlation exists.

3.7. Workflow

After obtaining the modelling input data and following the created methodology, the simulated irradiance can be determined. Figure 3.9 presents the workflow of the developed methodology. Determining the surrounding environment using the topographical BBG map is not presented in this workflow, as it is unrelated to the required steps in the modelling approach.

The simulated irradiance ($I_{simulated}$), given as the output in Figure 3.9, represents the irradiance which is lost due to shading by surrounding obstructions. The simulated irradiance includes the varying shading indicators, SVF and SF, for multiple points along the route. By subtracting the simulated irradiance (where SVF$\leq$1) from the input irradiance of an unobstructed horizon (where SVF=1), the reduction in incident irradiance can be determined. The reduction is known as the shading loss. This computation is given in Equation (3.2), where I represents irradiance, and I_{KNMI} is the example irradiance input dataset based on a free horizon.

$$I_{\text{lost by shading}} = I_{KNMI} - I_{\text{simulated}} \tag{3.2}$$

The shading loss in this work is represented as the part which is lost in irradiance or irradiation, in W/m^2 or Wh/m^2, or can be given as a percentage as in Equation (3.3). The statistical Equation is the percent error, representing the shading loss in percent [79].

$$\text{Shading loss } (\%) = \frac{I_{\text{lost by shading}}}{I_{KNMI}} \cdot 100\% \tag{3.3}$$

Given the improved methodology for determining the varying shading losses in VIPV, the first research question is addressed in the following Section 3.8, representing this Chapter's conclusion.

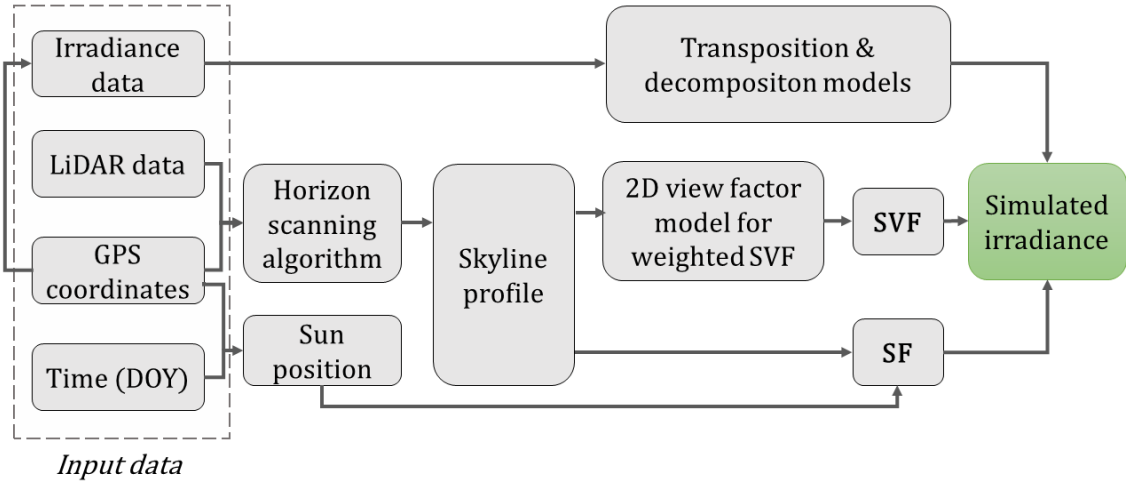

Figure 3.9: Workflow presenting the modelling methodology for obtaining the simulated irradiance, which is used to determine the shading loss.

3.8. Conclusion

This Chapter addresses the following research question: **how to implement key factors causing shading loss to improve TNO's VIPV shading assessment?** Key irradiance loss factors which affect the irradiance prediction are location, weather and time-dependent. Different approaches which identify the surrounding environment have been compared through a multi-criteria analysis using relevant criteria: scalability, accuracy, transparency, and validity of the modelling approach. The DSM-based approach is chosen in this work as it outperforms other methods by fulfilling all four stated criteria. To predict the irradiance losses in VIPV more accurately than the current TNO shading assessment, four key inputs are required.

The study area is the initial input requirement, where the remaining three inputs are based on key factors causing shading loss: the time and day of the year (to determine the Sun's position), irradiance data (of a particular location for calculating incident solar irradiance), and height data (using a DSM for simulating the surrounding environment). Within the DSM-based approach, an improvement is made concerning the model's scalability. Height data can be obtained by simply inputting GPS coordinates into a URL using a Web Coverage Service (WCS) request, eliminating the need for manual operations as seen in previous studies [18, 26]. By scanning the horizon for 360°, the surrounding environment can be visualized. Using the varying shading indicators, SVF and SF, the irradiance can be simulated for a chosen route. This results in a location- and time-specific model, which can input different weather datasets and where the simulated irradiance depends on various decisions and assumptions regarding the input parameters. In conclusion, the model effectively characterizes the key factors causing shading loss, thus providing a more comprehensive assessment than TNO.

4
Model Validation and Sensitivity Analyses

This Chapter introduces model validation using two different datasets, followed by sensitivity analyses to determine errors and, consequently, validate the model. The validation approaches and results are presented in this Chapter. The final Section 4.8 of this Chapter addresses the conclusions and research question: **how to determine the quality of the model by validation?**

4.1. Validation datasets

Two different types of datasets obtained by TNO are applied to validate the improved modelling approach. The data used for the first validation study is measured irradiance from horizontal sensors mounted on a moving vehicle, followed by a comparison with simulated irradiance in Section 4.2 [12]. This validation data is called the dynamic dataset, which consists of measured dynamic data for one day. The data used for the second validation study is measured irradiance from a stationary pyranometer, followed by a comparison with simulated irradiance in Section 4.4 [80]. This validation data is called the static dataset and includes measured irradiance for one year.
Both datasets include measured irradiance for an unobstructed horizon, resulting in a SVF$\leq$1. The validation of the model is conducted by comparing the measured irradiance with the simulated irradiance, which considers the computed SVF and SF for multiple road survey points (in the dynamic dataset) or data points (in the static datasets).

4.2. Dynamic dataset

On October 9th, 2019, TNO collected experimental data using the Vehicle Irradiance Test System (VITS) setup [12]. This setup included a flat PV panel mounted on the roof of a car, powering the data acquisition, and four irradiance sensors on each corner of the panel. The setup is visualized in Figure 4.1.

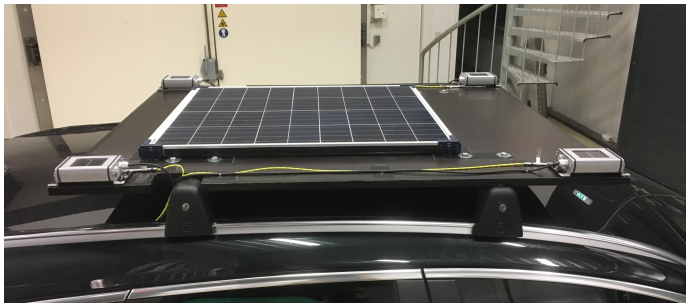

Figure 4.1: Vehicle Irradiance Test System (VITS) with four irradiance sensors mounted on each corner of the setup [12].

The system also recorded speed, temperature, and GPS coordinates while the vehicle was in motion. The sampling frequency, denoted as f, is the amount of data points obtained in one second: $f = \frac{1}{T}$, where T is the time interval in seconds. The irradiance and temperature values are measured with $f = 100$ Hz, and the GPS coordinates with $f = 1$ Hz. Therefore, irradiance data is averaged from 100 Hz to 1 Hz to align with the GPS coordinates. Irradiance data from the moving sensors and corresponding GPS coordinates are used for this validation. During the test route, the driver of a passenger car with the mounted VITS commuted from home to work in the early morning and returned home in the late afternoon. Around midday, the driver conducted another drive. On the test day of October 9th 2019, the clear sky irradiance, the KNMI irradiance data from the nearest weather station, and the horizontal measured irradiance are collected and compared. Figure 4.2 shows the collected irradiance datasets for the full test route, where the moments of a vehicle driving or parked are indicated. The clear sky and KNMI irradiance have a SVF value of 1, as both datasets are based on a

free horizon.

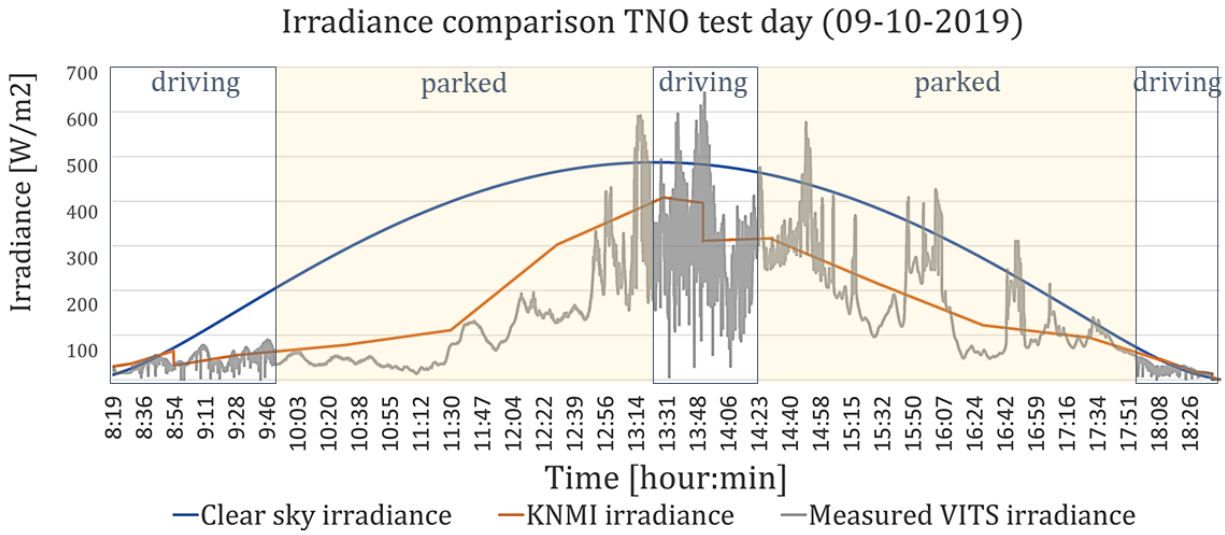

Figure 4.2: Comparison between measured, KNMI and clear sky irradiance datasets for the test route of the 9th of October 2019, including the time ranges of the vehicle being parked and driving.

This validation study primarily focuses on the midday drive because solar irradiation during this period shows more noticeable fluctuations, given the higher irradiance levels compared to early mornings and late afternoons. In addition, the midday drive offers the greatest potential for generating PV energy to supply for the vehicle [30]. The solar altitude varies depending on the specific time and location along the route. The highest point of the solar altitude, known as the solar noon, occurred around 12:28, reaching a peak altitude (a_S) of approximately 30 degrees for the 9th of October 2019 [42]. During the midday drive, the vehicle travelled from Breda at 13:27, passing through Tilburg and Eindhoven, and arriving at the Helmond Automotive Campus at 14:20. A total distance of 75 kilometres was covered during which the Sun's altitude gradually decreased from 26° to 21°. The midday route is shown in Figure 4.3.

Figure 4.3: Midday route from the test data obtained on the 9th of October 2019 used for model validation.

Fluctuations in measured irradiance

Significant variability and fluctuations in irradiance levels are observed in both parked and moving vehicle situations in Figure 4.2. The measured irradiance significantly deviates from the KNMI data and exceeds the clear sky irradiance. Figure 4.2 shows significant differences in measured, KNMI, and clear sky irradiance, especially during midday. On this specific day, KNMI recorded an average of 7 oktas, indicating a broken, cloudy atmosphere [55]. The potential factors which can cause this phenomenon are addressed below:

- **Cloud enhancement:** Even considering the nearest KNMI dataset and interpolating the values to the area of interest, there remains a significant uncertainty concerning the local clouds. As the intensity of clouds passing by varies locally, the Sun obstructed by clouds can differ for the two nearby areas. Cloud enhancement causes short-term reflections due to fair weather clouds and results in differences in measured irradiance depending on the intensity, ranging from 20 seconds (enhancements >400 W/m^2) to up to 140 seconds (enhancements >200 W/m^2) [81]. At short timescales, cloud enhancement can

result in irradiance surpassing clear-sky conditions [82]. This observation is also evident when looking at Figure 4.2.

- **Surrounding obstructions:** The measured irradiance includes surrounding obstructions along the road, in contrast to KNMI and clear sky irradiance, which are both considered for a free horizon. Surrounding obstructions, such as buildings and trees, result in different skylines which can obstruct the Sun. The presence of obstructions can lead to fluctuations in measured irradiance.

- **Irradiance sensor noise**: Sensors on the vehicle roof capture varying light intensities due to obstructions and rapid cloud changes, resulting in inaccuracies and noise. The signal reflection and noise is a random variation in the sensor's output [83]. Measurement uncertainty is addressed in Section 4.3.

Finally, in reality, the large variations in incident irradiance will affect the electrical performance of PV panels. Given the multitude of factors contributing to irradiance loss, the maximum power point for the PV panel faces challenges locating the optimal operational point, thus resulting in a lower PV power output [22]. This validation study only considers irradiance loss and leaves the PV panel power output out of scope. It is, therefore, assumed the loss in irradiance observed by the PV panel is in line with the sensors.

Comparison of simulated and measured data

Following the irradiance calculations given in Chapter 2, and using the methodology and workflow explained in Chapter 3, the simulated irradiance can be determined for the same GPS coordinates recorded in the experiment. In this case, only one point on the PV panel is considered, assuming a uniformly shaded PV panel. Using the GPS coordinates recorded by the front left sensor, the varying shading indicators (SVF and SF) have been computed for the midday drive, in total 3221 time-based road survey points. To simulate the irradiance, historical KNMI irradiance with SVF=1 is used as the irradiance input. The KNMI irradiance is obtained as Global Horizontal Irradiance (GHI) in W/m^2 1for every 10 minutes from the closest weather station. The irradiance values have been interpolated to obtain values every 1 second, and the GHI is decomposed into the DHI and DNI. The DHI, DNI, GHI, SVF and SF are the variable inputs in simulating the irradiance for each road survey point. Figure 4.4 plots the measured, simulated, KNMI, and clear sky irradiance for the midday drive.

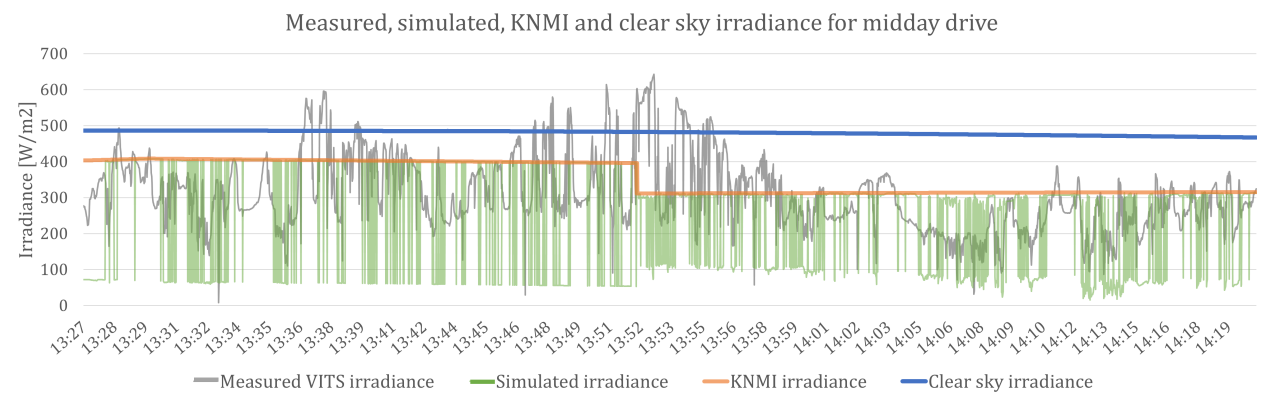

Figure 4.4: Measured, simulated and KNMI irradiance for the midday test route in the dynamic validation dataset.

The orange graph, representing KNMI irradiance, shows a drop in irradiance at 13:52. This drop is caused by transitioning to a new dataset from a closer KNMI weather station to the vehicle at that particular moment. TNO has integrated both KNMI irradiance datasets to use for analysis [12]. The measured irradiance fluctuates significantly, surpassing KNMI, reaching up to irradiance enhancements of 300 W/m^2 around 13:53. This leads to higher irradiance levels, up to a factor of two times more compared to the KNMI data. The KNMI dataset has a consistent SVF value of 1 and SF value of 1, whereas the measured includes obstructions in the surrounding environment. The simulated irradiance will, therefore, not exceed the KNMI irradiance.
For all the road survey points, the varying shading indicators have been determined, considering the specific location and time. When an obstruction blocks the Sun, an immediate reduction of irradiance can be seen. Upon closer examination of the simulated irradiance graph, given in green in Figure 4.4, a clear pattern is observed as it fluctuates with values ranging from around 400 W/m^2 in the top part to less than 100 W/m^2 in the bottom part. These fluctuations are primarily influenced by the interplay between the direct and diffuse components of irradiance, with the diffuse component providing a baseline and visible variations occurring due to the presence or absence of the direct component, represented by discrete SF values of 0 and 1. Given

the time frame of this experimental dataset, around solar noon, the decomposition of GHI into DHI and DNI results in the DNI component having a high contribution to the incident irradiance as the position of the Sun is highest above the horizon. This results in a higher direct solar irradiance component, for a SF of 1, when compared to diffuse solar irradiance, thus presenting a large difference in values.
In addition, the driving speed affects sensor response times, leading to phase lag [22]. Phase lag can result in unpredictable phase shifts of recorded irradiance, which is untraceable in the dataset. From the specification sheet, the irradiance sensors used in this experiment have a typical response time of 0.15 seconds (for 99% of the measurements) [84], which might lead to measured irradiance being associated with a different GPS coordinate. This can result in a larger deviation between the measured and simulated irradiance than in reality. Furthermore, LiDAR data captures static objects such as buildings but does not accurately represent open structures and seasonally changing objects such as trees. This results in an erroneous skyline, where an example is given in Appendix H. Furthermore, the DSM dataset lacks time-related information, so it cannot track moving or changing objects in the past or future. An example is traffic shading, where taller vehicles block sunlight from reaching PV panels on cars next to them, causing a drop in measured irradiance. This reduction in irradiance cannot be reflected in the simulated irradiance, leading to differences. This inconsistency is known as the LiDAR discrepancy.
To compare the obtained midday drive values, the average irradiance and shading loss values are determined and presented in Table 4.1. Moreover, Figure 4.5 shows linear trend lines of the irradiance datasets, which helps visualize the underlying trends for comparison, even though the fluctuations are smoothened.

		KNMI	Measured	Simulated
Average irradiance [W/m2]	Input	355.47		
	Output		306.53	257.50
Average varying shading indicators [-]	SVF	1	$\leq$1	0.87
	SF	1	$\leq$1	0.66
Shading loss [%] (using Equation (3.3)**)**			13.77%	27.56%

Table 4.1: Average irradiance, SVF and SF values for three irradiance datasets including the shading losses relative to KNMI irradiance for the midday route in the dynamic validation dataset.

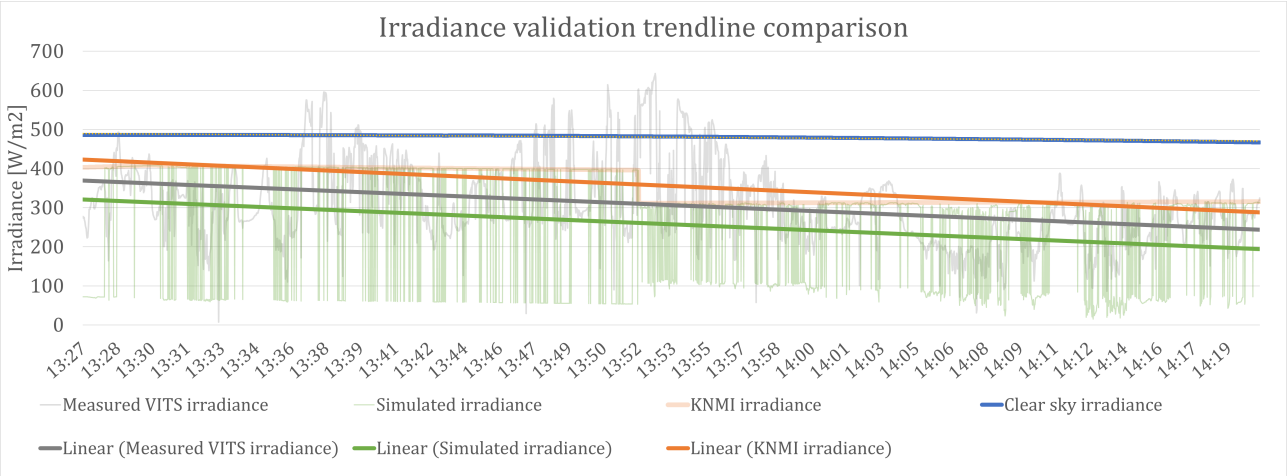

Figure 4.5: Linear trend lines for each dataset indicated in the irradiance comparison graph illustrate the underlying trends for the midday test route in the dynamic validation dataset.

Table 4.1 shows a 13.77% shading loss when comparing measured irradiance to the interpolated KNMI irradiance. In addition, a 27.56% relative percentage difference between KNMI and simulated irradiance is observed. The difference in shading loss between measured and simulated irradiance should be neglectable to validate the model. However, the absolute difference in average shading loss is 13.79%. This misalignment can be attributed to local weather effects, equipment sensitivities and LiDAR discrepancies, such as traffic shading and open structures. The obtained validation value is compared to existing literature, where a similar DSM-based modelling approach is applied in the thesis of De Jong [67], to estimate the PV potential of the in-land shipping fleet in The Netherlands. This research compared simulated irradiance with experimental results for a horizontal PV system (0° tilt). Based on 33 data points collected over a week, the percentage difference between measured and simulated irradiance was 6.15%. The difference in approaches is data points are collected and spread over different days, in contrast to many data points within one hour. This

study's more significant difference between simulated and experimental values is addressed in the next Section 4.3, where an uncertainty analysis accounts for various errors and factors.

4.3. Uncertainty analysis of dynamic data

This Section assesses and quantifies the uncertainties of inputs in the dynamic validation dataset by conducting various sensitivity analyses. As there are multiple factors which lead to misalignment in the results, the aspects which can be quantified are considered. Errors and uncertainties which arise in the validation studies are related to measurement inaccuracies (such as signal noise leading to GPS offsets), numerical imprecision (such as rounding and averaging of obtained values), assumptions (resulting in differences from real-world scenarios), and finally, the weather variability (which is a random error).

4.3.1. Sensor inaccuracy

The measurement uncertainty values of the irradiance sensor (Si-V-10C-T), the data acquisitions logger (IMC CANSAS SC18), and the GPS receiver sensor (Garmin GPS 18x 5Hz™) are presented in Appendix I. The combined standard uncertainty (u_c) for the irradiance sensor and data logger in the dynamic validation data was calculated following procedures from Cook's 'Assessment of Uncertainties of Measurement for Calibration and Testing Laboratories' book and Carr's PhD thesis work [83, 85]. This calculation considered components independent of each other. The computation of the combined standard uncertainty is presented in Appendix I and is determined to be 1.52% for the dynamic dataset.

4.3.2. Time- and distance-based road survey points

This sensitivity analysis is based on an assumption made in this thesis, where road survey points are spread for a chosen distance. Time-based points can be experimentally obtained, for example, with a frequency of 1 second such as in the dynamic dataset. In contrast, the distance-based points are created with a spatial distance in between them, used for computing the simulated irradiance. The comparison is based on the SVF, indicating the sky visibility, and the difference in values between the time- and distance-based road points. The average of all SVF values for the time-based road survey points is used as the dependent variable.

Temporal (1 second) and spatial (>23-3000 meters) points

A comparative analysis of the SVF values at different spatial intervals has been conducted, ranging from 23 meters to 3 kilometres between each road survey point. Figure 4.6 illustrates the correlation between the deviation in average SVF, given in percentage (%), concerning both temporal points and chosen spatial points. In this analysis, the coefficient of determination (R^2) is used, which provides information on whether the simulated data corresponds to the actual data. Curve fitting the data allows for a comparison to determine which regression better describes the data. By examining the data visually, the exponential curve has a slightly better fit to the data than the parabolic curve, resulting in R^2 is 0.9222.

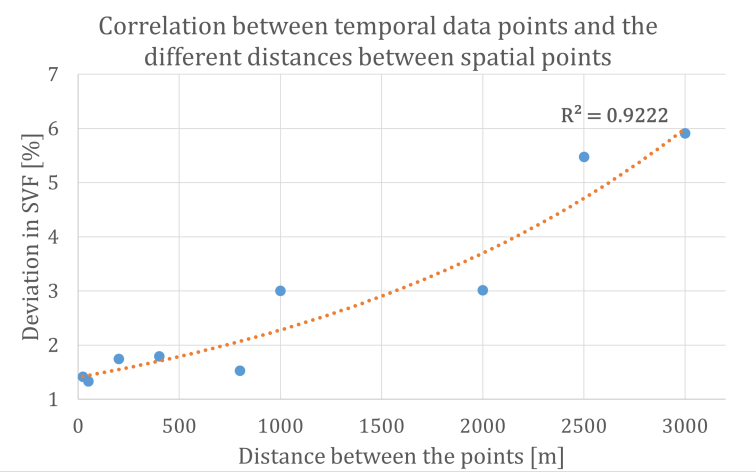

Figure 4.6: The correlation between temporal points and chosen spatial points based on the difference in average SVF, given in percentage (%).

For spatial distances below 500 meters, the difference in average SVF between temporal and selected spatial points remains at 1.80%. However, as the spatial distance exceeds 500 meters, the SVF deviation increases significantly. For example, at 3-kilometre intervals, the SVF deviation reaches 6%. However, the spreadability

between points can vary between routes and measurements. This sensitivity analysis indicates that the outcomes are route-dependent. For example, a long tunnel may be filtered out when distancing the points every 3 kilometres. This leads to many SVF values of 0 being filtered out, as the sky is blocked in the tunnel. The reverse is also possible, where many SVF values close to 1 are filtered out, but the SVF of 0 remains in the dataset. This leads to the spreadability of points in the correlation. To balance computational efficiency and accuracy, a spatial distance below 100 meters was chosen for road survey points in the case studies, depending on the route length.

Temporal (1 second) and spatial (>0.5 meter) points
This analysis involves testing the sensitivity between temporal and spatial road survey points, with distances smaller than the AHN3 LiDAR data resolution (0.5x0.5m^2). To evaluate the impact of distances smaller than the LiDAR resolution, a 200-meter route segment was selected for error analysis to minimize computational calculations yet still assess whether the approach is feasible. In the TNO dataset, time-based data points were filtered from 100 Hz to 1 Hz, as the GPS receiver's measurement frequency is limited to 1 Hz. The skylines are generated for a frequency resolution larger than 1 Hz or smaller than 0.5 meters to identify if the skylines can be represented correctly. The average speed for this route was 28.8 km/h, equivalent to 8 m/s. Assuming a constant speed, the road survey points are spaced 8 meters apart for every 1 second. To conduct this sensitivity analysis, the chosen spatial distances are 0.5 meters (equivalent to 16 Hz) and 0.08 meters (equivalent to 100 Hz) for an average speed of 8 m/s.
As a result, the skyline patterns and SVF values closely correspond between the temporal-based points and both simulated cases. In both simulated cases, the relative percent difference is 1.00%, indicating small spatial distancing between points is feasible. The small percent difference of 1.00% should be taken into account when choosing a distance smaller than the LiDAR resolution (<0.5 meters) or high-resolution measurement (>1 Hz).

4.3.3. GPS offset errors

This sensitivity analysis is based on measurement inaccuracies caused by the signal noise in a GPS receiver. The GPS receiver typically has an accuracy of <15 meters for 95% of readings [86]. In the dynamic dataset, a notable GPS offset of approximately 5 meters is observed, parallel to a 200-meter road segment in Echt, The Netherlands. The GPS coordinates have been logged incorrectly and away from the intended road. While the impact of such offsets can vary, this sensitivity analysis serves as an example to identify and evaluate the effect of GPS offset on the results. The offset is visualized in Figure 4.7.

Figure 4.7: A visible GPS offset in the dynamic dataset in a residential area in Echt, The Netherlands.

Without manually correcting the GPS coordinates, which have an offset, the horizon will be scanned with errors. ArcGIS Pro has the ability to manually move the data points back to the road using the 'Distance & Direction' tool. In a situation where the height of an obstruction (h_{obs}) is larger than the height of the vehicle (h_{offset}), the horizon will be scanned incorrectly. Skylines have been generated for data points with the 5-meter offset and corrected data points, back on the intended road. The comparison of the two skylines is shown in Figure 4.8, where the left skyline is the data point with a GPS offset and the right skyline without an offset. The skyline of the corrected data point is verified by examining surrounding obstructions on Google Street View in the southwest (SW) direction.
There are large differences between both skylines. For all road points, with and without GPS offset in the 200-meter road segment, the SVF values have been computed and compared. The relative percentage difference in SVF values is 15.77% on average. When relating this SVF deviation to the total route of 245 kilometres travelled during the TNO experiment, the error in measurements becomes a lot smaller: $\frac{0.200}{245} \cdot 15.77\% = 0.01\%$. The GPS measurement error for this route is estimated to be 0.01%. Although the

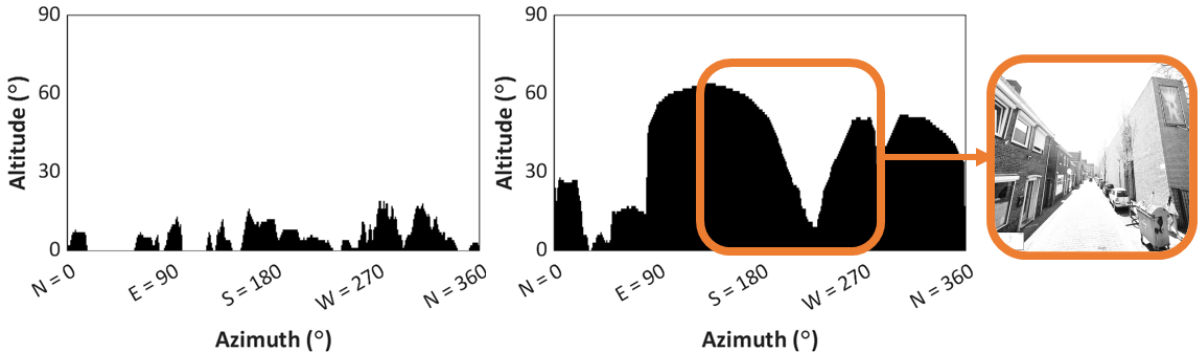

Figure 4.8: Skyline comparison of the data point with a GPS offset of 5 meters (left) and the corrected data point (right), including the Google Street View verification.

200-meter route segment was manually corrected due to an observed deviation in coordinates, it is essential to notice that other smaller or less distinguishable GPS offsets along the route can also lead to SVF differences. These offsets remain unaddressed in this GPS error analysis due to a lack of precise trajectory information, such as road lane-specific details during the experiment.
In summary, the GPS errors have an impact on simulated SVF values. Still, the exact error is context-dependent and influenced by route length, offset distance, obstructions, and signal-related issues. Assuming only this specific route segment experiences an offset, an inaccuracy of 0.01% for the simulated SVF values should be considered.

4.4. Static dataset

For the second validation study, a static dataset of year-long irradiance measurements was used, obtained with a static pyranometer under non-free horizon conditions, in contrast to the single-day dynamic validation dataset. This data is obtained from the SONOB project carried out by TNO [80], which is located in Den Bosch, The Netherlands. The pyranometer is installed on a fixed location with a height offset of 4.51 meters and associated GPS coordinates (51.684225, 5.282113), therefore only one skyline profile is necessary.
Figure 4.9 displays the skyline profile and a 360-degree Google Street View image near the static pyranometer. The street view image is included for illustrative purposes, confirming a correctly scanned horizon with visible obstructions, such as the tall building on the left side, which is also indicated in the northeast (NE) direction of the skyline profile.

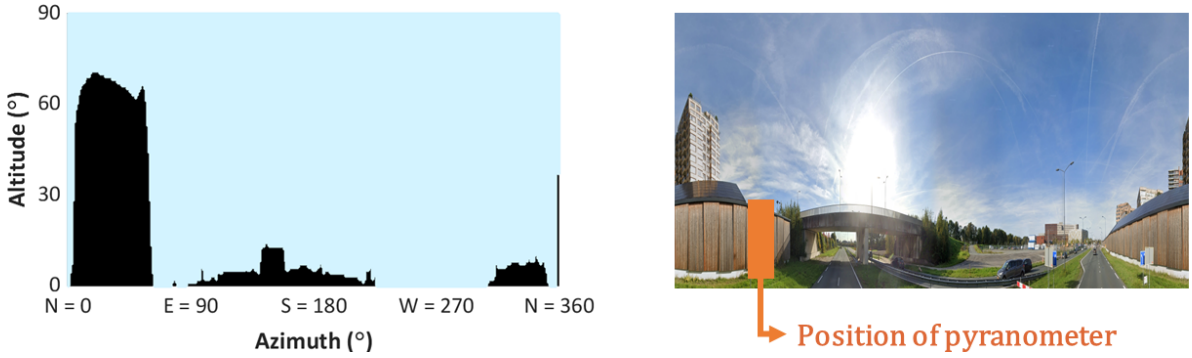

Figure 4.9: The simulated skyline profile (left) and verification using a 360-degree Google Street View image (right) of the static pyranometer location in Den Bosch, The Netherlands.

Comparison of simulated and measured data

The static pyranometer dataset consists of measured irradiance (in W/m^2) with a different frequency of $f = \frac{1}{120}Hz$. The dataset contains irradiance values measured every 2 minutes for one year. The running time of the experiment was from the end of April 2015 to the beginning of May 2016. The clear sky irradiance is computed for the given location and day of the year using the Ineichen-Perez clear sky model to validate the modelling approach [54]. With the same frequency as the measured data, the computed clear sky irradiance is compared to days where the static pyranometer measured (nearly) no cloud coverage. These days have been verified by looking into the KNMI-measured datasets of the closest weather station to indicate whether the okta was zero that day. By applying the varying shading indicator values, SVF and SF, for each specific time instant, the simulated irradiance can be computed. A reduction in irradiance is experienced, making it

valid to compare this dataset with the actual measured irradiance data by the static pyranometer. This process has been repeated for days each season with an okta of zero, representing little to no clouds.
An example of the simulated irradiance compared to the clear sky irradiance and what is measured is shown in Figure 4.10. For the 11th of October 2015, the profile of the irradiance measured by the static pyranometer, indicated in grey, aligns with the simulated irradiance, given in orange.

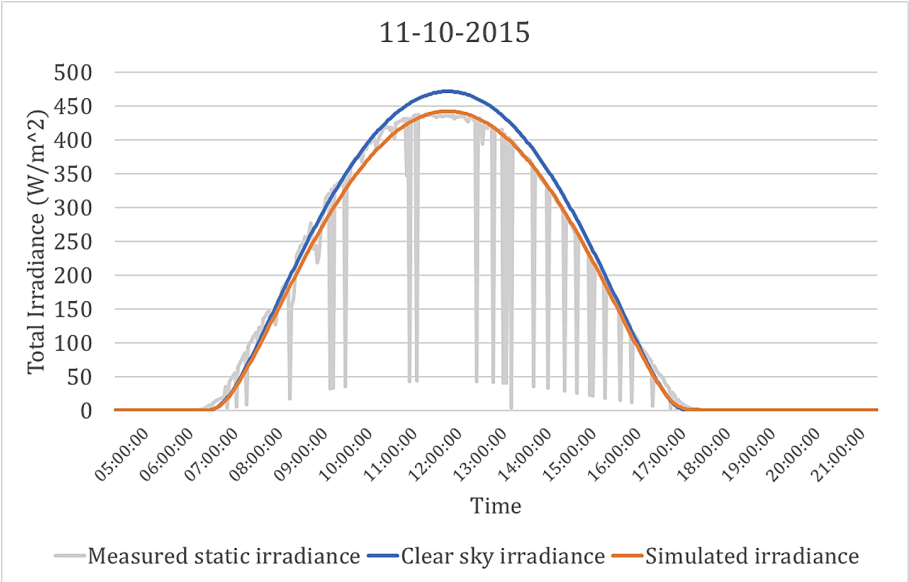

Figure 4.10: Measured, clear sky & simulated irradiance for a near-clear sky day on the 11th of October 2015.

There are no observable peaks in simulated irradiance indicating that the Sun is not obstructed by obstacles during this day. This indicates a good fit between the irradiance lost due to the environment, as represented by the SVF. This validates, along with the visual validation in Figure 4.9, the method for determining the environment using LiDAR data. However, peaks in the measured static dataset result in misalignment, reflecting rapid weather fluctuations typically caused by clouds passing by on a short timescale, usually within a few minutes.

		Clear sky	Measured	Simulated
Average irradiance [W/m2]	Input	173.16		
	Output		155.22	162.12
Varying shading indicators [-]	SVF	1	≤1	0.86
	SF	1	≤1	1
Relative difference between measured and simulated irradiance [%]			4.2%	

Table 4.2: Average irradiance, SVF, and SF values for three datasets with the relative percentage difference between measured and simulated irradiance in the static validation dataset.

In Table 4.2, the average irradiance and varying shading indicators are shown. Both the measured SVF and SF are ≤1, as the exact obstructions and cloud cover at that time are unknown. The relative percentage difference between the simulated and measured irradiance for the 11th of October is calculated to be 4.2%, using Equation (4.1). The small percentage difference is caused by uncertainties mentioned in the following Section 4.5.

$$\text{Relative percent difference \%} = \frac{|\Delta V|}{\left[\frac{\Sigma V}{2}\right]} = \frac{|Value_1 - Value_2|}{\left[\frac{(Value_1 + Value_2)}{2}\right]} \times 100\% \tag{4.1}$$

For other days, when the cloud coverage was low, the relative percentage differences between simulated and measured irradiance lie within the range of 0.4-18.8%, where the difference is highly dependent on the amount and intensity of local clouds. The range is based on four different days, one in each season, where the irradiance graphs had the least weather fluctuations to be used for validation with the simulated irradiance. The losses caused by local cloud passage are untraceable and, therefore, not considered in this work.
As with the dynamic dataset, the measured irradiance occasionally exceeds clear sky conditions, typically occurring in the early morning and late afternoon. This surpassing of irradiance can result from factors such as cloud enhancement or using empirical models, where real-world conditions are simulated using observed data

and mathematical modelling [54]. The advantage of the stationary pyranometer validation is that it does not encounter any inconsistencies due to driving speeds and dynamically changing shading within milliseconds. As a result, the output becomes more stable, making the static dataset more accessible and suitable for validation. Even though the results are more stable, the weather fluctuations and sensor uncertainties must be considered.

4.5. Uncertainty analysis of static data

Similar to the dynamic VITS dataset, the pyranometer measurements experience offsets due to equipment sensitivity. The main difference is that the static pyranometer has a fixed location compared to the dynamic VITS dataset. The static pyranometer (EKO MS-802) measurement uncertainties are detailed in Appendix I. Following procedures outlined in Appendix I, the combined standard uncertainty (u_c) for the static pyranometer and the assumed data logger is calculated to be 0.59%.
Another uncertainty factor in this dataset is the determination of days with little to no cloud cover. Historical irradiance data from the nearest KNMI weather station, located in Eindhoven and approximately 25 kilometres from the static pyranometer, was used for assessing cloud coverage. On days with an okta of zero, indicating little to no cloud cover, there could still be clouds present at the location of the static pyranometer. Besides, identifying the highest irradiance in the annual dataset can also result from significant cloud enhancements rather than only clear sky conditions. Weather conditions remain a highly influential factor, leading to deviations ranging from 0.4% to 18.8% between measured and simulated irradiance, even when weather fluctuations are minimized.

As a result, the validation of the modelling approach has been performed using two different types of datasets. To identify the differences in both datasets, the measured and simulated irradiance values are compared for both validation studies in Section 4.6.

4.6. Deviations in measured and simulated irradiance

The deviations in measured and simulated irradiance values are compared by plotting normal distribution curves. These curves describe data distribution using the mean (μ) and standard deviation (σ), and are useful to visualize the data distribution of the measured datasets [87]. The mean and standard deviation of the dynamic dataset ($\mu = 46.19$ and $\sigma = 58.87$) and static dataset ($\mu = 6.90$ and $\sigma = 142.66$) are determined, where the data distribution is given as a measure of the difference between the measured and simulated irradiance: $I_{t,measured} - I_{t,simulated}$. In this case, t indicates the time to which both data points are compared, where σ presents the amount of dispersion from the individual data values to the mean (μ) [83]. A value of μ close to 0, with minimal distribution, indicates similar values of measured and simulated irradiance. Yet, in both validation studies, there are deviations due to the previously mentioned uncertainties and discrepancies. The shape of a normal distribution curve is influenced by the μ (center) and σ (spread) [87]. Figure 4.11 displays both normal distribution curves.

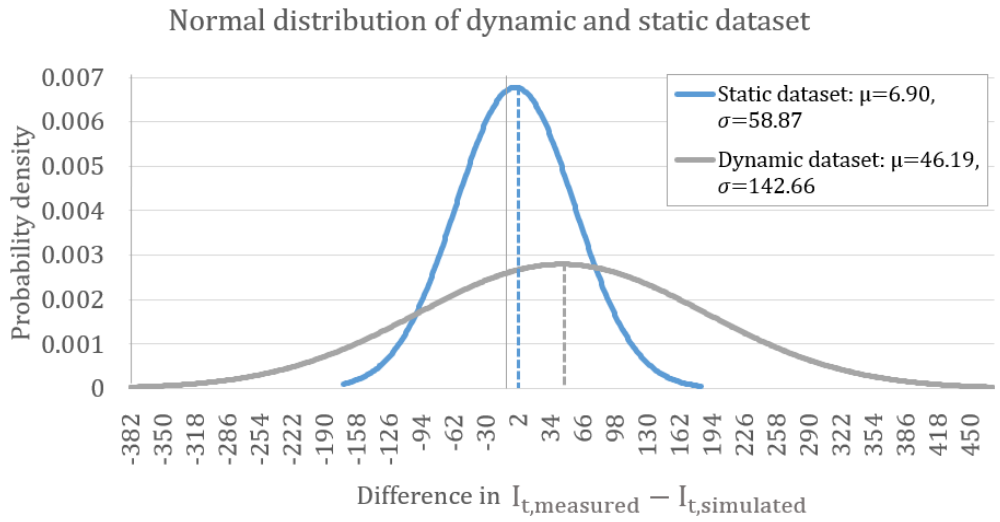

Figure 4.11: Normal distribution of the dynamic and static validation data, where the x-axis indicates the difference in measured and simulated irradiance and y-axis the probability density.

When examining the normal distribution of the dynamic dataset, it shows a significantly larger mean and

wider spread compared to the static dataset. This difference implies an imbalance, where either measured irradiance consistently exceeds simulated values or simulated irradiance is consistently lower due to identified uncertainties and LiDAR discrepancies. For example, in some cases, the measured dynamic data exhibits very high peaks, 1.5-2 times higher than the KNMI due to intermittent cloud enhancements. Similar to a reduction in irradiance due to clouds. In addition, the LiDAR discrepancy causes horizons to be scanned incorrectly for open structures such as overhanging power cables or leafless trees, leading to inaccuracies in the simulated irradiance. When comparing the individual measured and simulated irradiance for the dynamic dataset, a difference of 52% on average is determined. Whereas the absolute difference between the average measured and simulated irradiance was determined to be approximately 14%, showing more alignment as significant factors such as weather effects, discrete SF values and LiDAR discrepancies are filtered.
In contrast, the normal distribution of the static dataset reveals a smaller deviation between measured and simulated values, likely due to fewer LiDAR discrepancies, sensor noise and weather fluctuations under near-clear sky conditions. In addition, the incorrectly recorded GPS coordinates can lead to a GPS offset or phase lag in the dynamic dataset, while the static dataset benefits from fixed GPS coordinates.

4.7. Sensitivity analysis of terrain types

Next to the two validation studies, this thesis conducts a sensitivity analysis for extracting terrain types to be able to give a proxy of the SVF value. The land use (BBG) map, referred to in Section 3.6, is used to identify the surrounding environment. The BBG map has a scale of 1:10,000 and indicates an accuracy of 2 meters for the geometric polygons [78]. In total, eight different terrain types are categorized in this digital map, where the types are presented in Section 3.6
By creating a buffer of 100 meters, with a similar radius as the horizon scanner, the surroundings of every road survey point can be analyzed using the overlayed and intersected polygons from the land use (BBG2017) map [78]. There are two ways to extract terrain types intersected by the buffer: (1) all terrain types, or (2) only the largest overlapping terrain (assuming it is surrounded by one terrain type). The two different approaches are visualized in Figure 4.12. The extraction is further explained in Appendix D. Both approaches have been compared by performing a sensitivity analysis on one of the case studies, which includes 3018 road survey points. Considering only the largest overlay, the extracted amount of terrains remained at 3018. Whereas by taking into account multiple intersections within the buffer of each road survey point, 23,164 features were obtained.

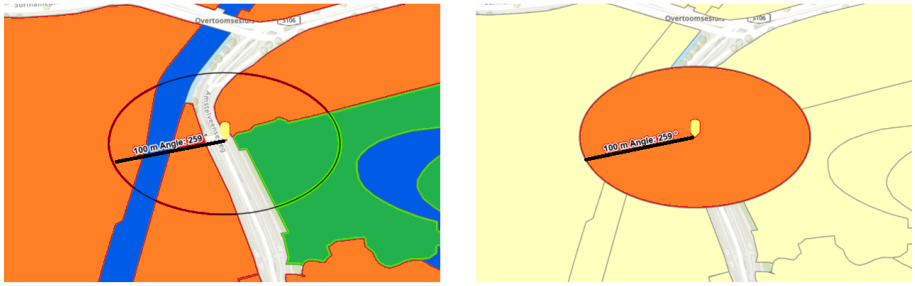

(a) Buffer intersects all terrain types

(b) Buffer intersects only largest overlapping terrain

Figure 4.12: Two different approaches for extracting terrain types, where (a) intersects all surrounding polygons, and (b) intersects only the largest overlapping polygon.

A sensitivity analysis between the two approaches is performed by determining the terrain type(s) for each feature in the case study. The terrain intersections are summed based on each category. The terrain type distributions, using both approaches, are shown in Figure 4.13.
In these charts, the share of all intersected terrains within the buffers is presented in the left graph, whereas the share of only the most significant terrain type is shown in the chart on the right. In residential and urban areas, the less precise method considers only the most significant overlapping section, resulting in a large fraction of 66% of the road survey points being within built areas. However, when including every intersection within the 100-meter buffer of a data point, this proportion decreases to 47%. In the pie chart, the traffic terrain is small for both approaches, as the roadways have been filtered out since every data point is situated on the road. The remaining 2% is the presence of mostly train tracks located close by.
In summary, as each route differs and the distribution of terrains varies, the quantification remains unfeasible. This comparison shows how sensitive the difference in interpretation of a topographical map is. This work considers all the surrounding terrain fields by gathering more than one intersection for each 100-meter buffer around a road survey point. This increases the calculation time; however, it is more accurate in terms of

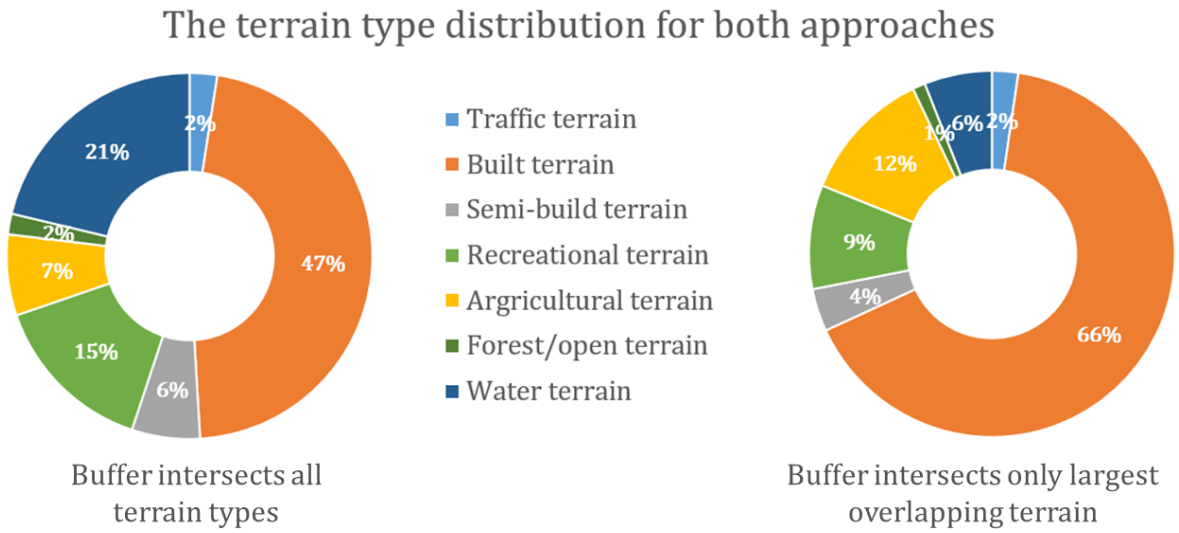

Figure 4.13: Comparison of terrain type distribution intersecting all terrains (left) and only the largest overlapping terrain (right).

quantifying the surroundings and for what part it constitutes in contrast to one terrain type enclosed by the entire buffer area.

4.8. Conclusion

In this Chapter, the following research question has been addressed: **how to determine the quality of the model by validation?** The quality of the model is determined through validation, which involves using two types of datasets: dynamic VITS data and static pyranometer data, both for non-free horizons (SVF$\leq$1). The validation process is demonstrated by aligning the simulation model with Google Street View images in dynamic and static validations (see Figure 4.8 and Figure 4.9), along with the previously verified WCS contribution in Appendix H. In addition, the comparison of measured and simulated irradiance in the static dataset indicates reduced irradiance due to obstructions, aligning the two in Figure 4.10. This concludes the model's ability to account for obstructions and validates the skyline approach. However, there are visible differences between the measured and simulated irradiance. This misalignment is caused by measurement inaccuracies, numerical imprecision, assumptions, and weather variability, where the errors arise from GPS offsets and LiDAR discrepancies. Sensitivity analyses determine how these uncertainties vary and contribute, with weather variability being the most significant uncertainty factor. Cloud presence leads to fluctuations in measured data, seen in both static and dynamic datasets, reflecting in the normal distribution spread. Additionally, the midday route around solar noon gives a larger portion of DNI than DHI in the decomposition, which results in large differences between direct and diffuse simulated irradiance (ranging from approximately 100 to 400 W/m2) due to the discrete SF value. Table 4.3 summarizes the input datasets used in both validation studies, where the differences are based on the key factors causing irradiance loss.

	Inputs		
	Irradiance data	**Time frame**	**Surrounding environment**
Dynamic dataset	measured & KNMI irradiance (including weather effects)	around solar noon	consistent for 1 route segment
Static dataset	Measured & clear sky irradiance (excluding weather effects)	all hours a day	consistent for 1 location

Table 4.3: Different inputs for the validation studies based on the significant irradiance loss factors in VIPV: irradiance data, specific time frame, and surrounding environment.

Despite these challenges, averaging results over the entire route or day provides better consistency in irradiance values, as it minimizes the impact of local variations and errors. By repeating measurements under constant conditions, systematic errors can be quantified and corrections can be applied [83]. Averaging is chosen to compare results in this work, removing outliers caused by untraceable factors. Therefore, this approach is suitable for route-level assessment, as it effectively identifies the environment, ensuring a good-quality model. However, determining a fixed inaccuracy factor requires more data from measurements.

5
Case Studies

This Chapter elaborates on the assumptions and decisions made for the two chosen case studies. In Section 5.1, the decision for analysing bus routes is explained. Section 5.1.1 introduces the first case study, the Bus 40 case study, traversing from Rotterdam to Delft. Section 5.1.2 introduces the second case study, which focuses on all 27 bus routes in and around Amsterdam. Both case studies use different input datasets. In Section 5.2, partial shading is explained in more detail considering the stated assumptions. Finally, Section 5.3 states the Chapter conclusions.

5.1. Bus routes

In this work, analysing a systematic route with a fixed timetable is preferred for determining the varying shading losses rather than a randomly chosen route. Both case studies focus on public transport routes, as many public transport systems operate on predetermined routes and do not change regularly. This thesis focuses on public transport options that operate via roadways, as the available validation dataset from TNO focuses on a passenger car traversing on roads. Buses and trams are common public transport options, coming across different environments whilst remaining part of the road traffic, unlike the metro and train, which operate on dedicated networks. The difference between a bus and a tram is that trams are connected to power lines above, providing electrical power for operation. Utilizing LiDAR data, the above power lines are seen as a higher obstruction, for which the maximum altitude is the power cable above the vehicle and will result in a blocked sky underneath. Therefore, this thesis focuses on bus routes.
To obtain geospatial information on the bus routes, General Transit Feed Specification (GTFS) data is used. The GTFS data includes details about public transport schedules and routes, along with relevant geographic information specific to The Netherlands [88]. The Geoportal University of Groningen has converted this data into an ArcGIS map for spatial analysis [88]. Within this map, each bus route is presented as a polyline. Road survey points are generated along this line with a specified spatial distance using the ArcGIS Pro manual presented in Appendix D. The exact bus stops are excluded, as the road point density must be higher to observe the varying shading losses.

5.1.1. Bus 40: Rotterdam-Delft

The first case study, based on the Bus 40 route, travels from Rotterdam Central to Delft Station and comes across various environments, including urban areas, residential neighbourhoods, the TU Delft campus, and open areas. This study focuses on simulating the irradiance for two categories, using both a car and a bus. The bus has a height of 2.99 meters, based on the actual vehicle dimensions for the bus operator RET [89]. The passenger car is modelled with a height offset of 1.5 meters, similar to the values in the Cobbenhagen case study used in the TNO shading assessment [11]. For both vehicle categories, the road survey points are spaced at 50-meter intervals. This case study specifically focuses on one daily route in the bus schedule, where the time frame is around solar noon, starting from Rotterdam Central at 12:05 and reaching Delft Station at 12:43 [89]. This solar noon route offers insights into maximum solar irradiance and clearly shows the impact of the surrounding obstructions. To obtain annual irradiance values, the irradiance is simulated for each 15th day of the month for a full year using the clear sky irradiance model to isolate the impact of weather conditions. This study assesses the annual shading losses for both a bus and a car using consistent inputs. This is followed by comparing the obtained annual shading losses for a car to the TNO shading assessment. The characteristics and inputs of this case study are summarized in Table 5.1, and the bus route is visualized in Figure 5.1.

5.1.2. Bus routes of Amsterdam

The second case study includes all bus routes in Amsterdam, where each bus line has a starting or ending point in Amsterdam. Amsterdam is chosen for this case study for two reasons. Firstly, Amsterdam is a relevant area for TNO, considering previous VIPV projects and plans, given it is a potential test area. At a later stage, the experimental results can be compared with the simulated irradiance results as an extra validation.

Bus 40: Rotterdam-Delft	
Route characteristics	
Number of bus routes	1
Bus operator	RET
Bus dimensions	11.95 x 2.99 x 2.55 meters (LxHxW)
Route length	17.4 kilometres
Route duration	38:00 minutes
Distance between road points	50 meters
Amount of road points	257
Modelling input characteristics	
Vehicle categories (height)	Public transport bus (2.99 m), Passenger car (1.5m)
Irradiance dataset	Clear sky irradiance
Time frame	12:05-12:43 for every 15th day a month, for a full year

Table 5.1: The route characteristics and modelling inputs for the Bus 40 case study [89].

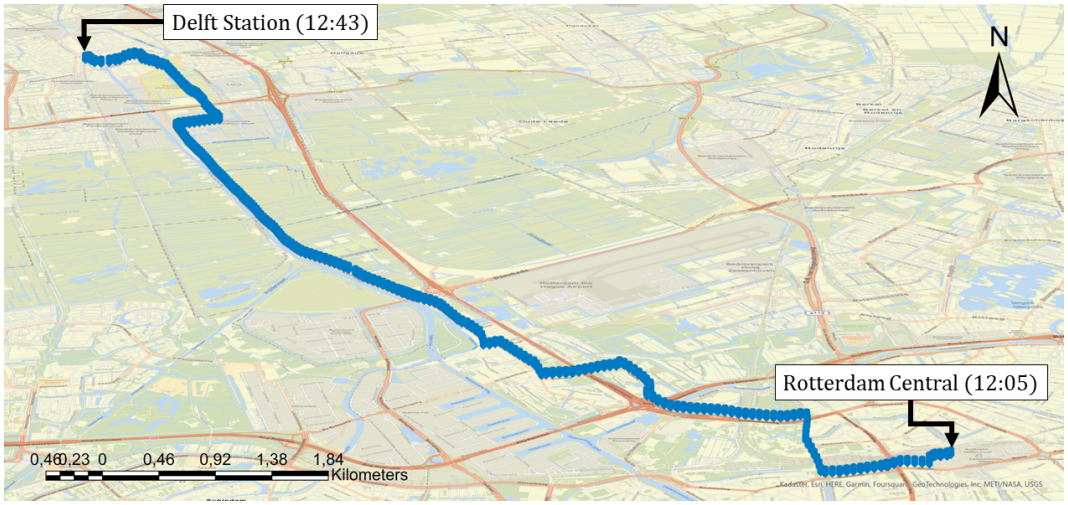

Figure 5.1: Bus 40 route, starting from Rotterdam Central (at 12:05) and arriving at Delft Station (at 12:43).

Secondly, given the city's emphasis on public transportation and reduced car commutes for work-home travel, the initial priority lies in implementing VIPV within public transit systems [90]. Since most buses in and around Amsterdam are electrified, integrating PV panels is a viable addition [91].
This study concentrates on simulating irradiance solely for buses across multiple routes. The road survey points are spaced at 100-meter intervals. A significant portion of the Amsterdam bus network consists of GVB buses, where this vehicle height is chosen for the irradiance simulation [91]. Furthermore, the comparison is based on the average annual irradiation of each bus route, given in kWh/m^2/yr, as the bus time schedules and durations are not similar. The irradiance data is obtained from the nearest KNMI weather station, Schiphol, and this data has not been interpolated to the exact location as it is assumed that this irradiance dataset is similar for all routes. This enables more consistency and gives the ability to compare the bus routes solely based on the differences in surroundings. The 27 bus lines and characteristics are presented in Appendix J.
Historical KNMI irradiance is used as input data in this study, where the time frame used for simulating the irradiance is hourly averaged KNMI irradiance for one month into one day. The data pre-processing involved hourly averaging of historical irradiance values, resulting in monthly representations. The monthly averaged values is assumed to be on the 15th day of that month to use this day of the year for the required solar position calculations. This approach is considered as it reduces many irradiance calculations in contrast to computing the irradiance for each day, whereas still obtaining realistic monthly irradiance values as weather effects cause reductions in irradiance. The averaging represents a uniform cloud cover and filters out high hourly fluctuations, contrasting with clear sky irradiance in the Bus 40 case study. In Figure 5.2, the averaging of hourly KNMI irradiance data into one respective day is illustrated. The light blue line graphs in this figure represent hourly irradiance values for each day in June, and the orange graph is the averaged irradiance input for June.

The fluctuating blue line graphs include weather effects, such as rain and overcast clouds, whereas the

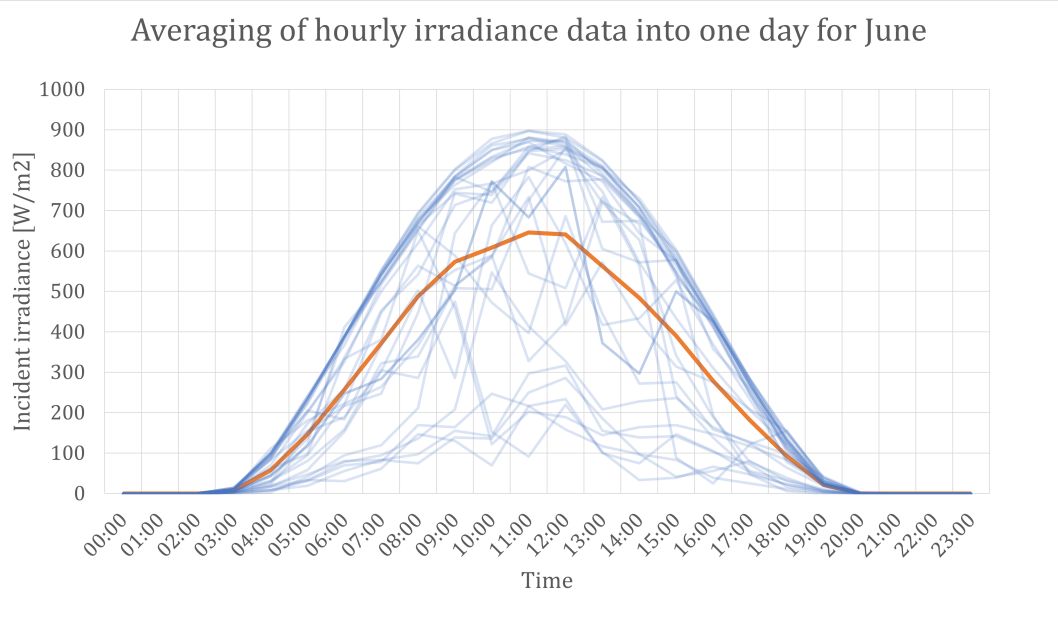

Figure 5.2: Averaging of hourly KNMI irradiance data into one respective day for June, where the 31 daily irradiance graphs (in blue) and averaged irradiance graph (in orange) are shown.

smoother parabola reaching high irradiance values refers to (near-)clear sky conditions.
The characteristics and inputs of this case study are summarised in Table 5.2.

Buses of Amsterdam	
Route characteristics	
Number of bus routes	27
Bus operator	GVB
Bus dimensions	18 x 3.42 x 2.55 meters (LxHxW)
Average route length	10.8 km (total length is 302 km)
Average route duration	26:00 minutes
Distance between road points	100 meters
Amount of road points	3018
Modelling input characteristics	
Vehicle categories (height)	Public transport bus (3.42 m)
Irradiance dataset	Averaged KNMI irradiance
Time frame	Hourly data for one month averaged into one day, for a full year

Table 5.2: The route characteristics and modelling inputs for the buses of Amsterdam case study [91].

This case study utilizes the BBG2017 land use map to assess the surrounding terrains [78]. In Figure 5.3 (on the next page), Amsterdam's bus routes are displayed with a 100-meter buffer around each road survey point. These buffers are overlaid and intersected with multiple terrain types, represented by a colour scale indicating the terrain type. The terrain type classification is used for the approximation analysis in Chapter 6.

5.2. Partial shading

Partial shading is caused by weather conditions as well as surrounding obstructions. Given the discrepancy of LiDAR for not accurately representing different obstructions, such as open structures and seasonally changing obstructions (trees and vegetation), the modelling approach used in this thesis is not useful for analysing partial shading as it requires more precision. Related to cloudy weather conditions, the exact pattern and geometry of local clouds passing by need to be known for partial shading. In addition, the cell interconnection as well as the bypass diodes, relevant for identifying the partial shading, is not considered. As this is beyond the scope of this work, it is limited to describing and quantifying the partial shading effect caused by surrounding obstructions by using methods and values in available literature.
In the outlook of C. Ferri [76], it was stated that the influence of dynamic shading on the maximum power point tracker (MPPT) efficiency should be researched further. In this theoretical case study, partial shading is

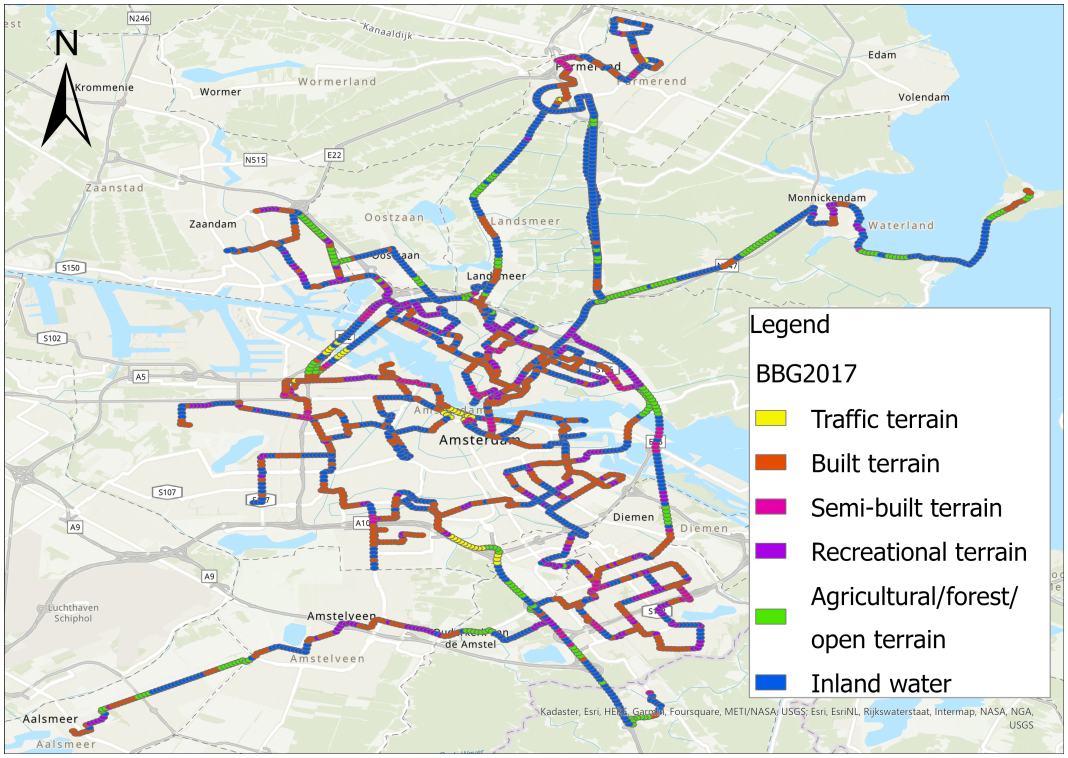

Figure 5.3: Bus routes in and around Amsterdam, categorized by surrounding terrain types from the land use (BBG2017) map [78].

explained to give a better understanding of how the partial shading losses relate to the total PV energy output. Point calculation assumes only one point on the PV panel, unlike area calculation, which uses numerous points on the PV panel to identify partial shading [28]. As a level of detail, this theoretical study considers the effect of partial shading by analysing the four irradiance sensors for the dynamic validation data, which produce an array of shading patterns. The analysis in ArcGIS is shown in Figure 5.4, where the irradiance values logged by the four sensors are visualized in a colour range. The red data points indicate a lower irradiance, whereas the irradiance values logged for the orange points are more increased.

Figure 5.4: Roadway indicating the four sensors which measured irradiance with a frequency 1 Hz (left),and a close-up view of the four sensors in every corner of the vehicle (right).

If a vehicle is in motion, shading results in a pattern which moves across the panel at a certain velocity. When the exact driving pattern and schedule are known with high precision, the frequency of shadows and varying shapes of a shadow moving across the VIPV panel can be predicted. The shading loss by surrounding obstructions can indirectly be assessed, assuming clear sky conditions which do not consider clouds passing by. In a situation where the exact driving pattern and surrounding obstructions are known, the rapid fluctuations that provide problems in the output of the MPPT can be adjusted. To illustrate this, when a vehicle travels beneath an underpass, which is a solid obstruction, a gradual decrease and increase in irradiance is measured [28]. In Figure 5.5, an example from the dynamic dataset shows the vehicle driving beneath the Viaduct Sterrenlaan within 5 seconds. In these 5 seconds, the four irradiance sensors experience a gradual change.

As the vehicle moves underneath an obstruction, most of the sky is blocked, resulting in a close-to-zero SVF and a SF of 0 as the Sun was obstructed. In this case, the irradiance is non-zero when travelling underneath the viaduct. This can be due to a small amount of diffuse or reflected irradiance reaching the PV panel, the sensitivities of the used sensors, or a combination of both. An illustration of the Viaduct is given in Figure 5.6.

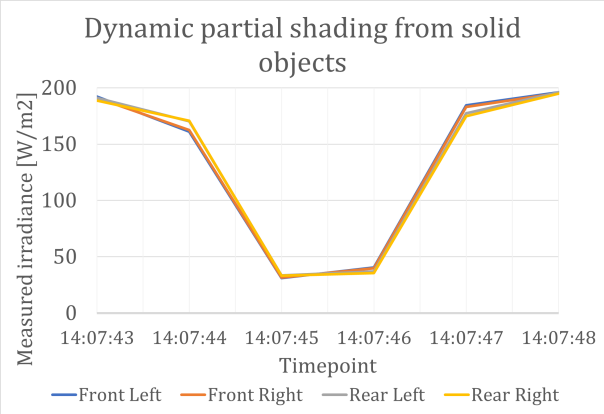

Figure 5.5: Partial shading caused by a solid object, Viaduct Sterrenlaan in Eindhoven, plotted for the four irradiance sensors in the dynamic validation dataset.

Figure 5.6: Viaduct Sterrenlaan in Eindhoven, where the vehicle route is indicated in yellow and the underpass in red.

In contrast to a solid obstruction, an irregular or complex surrounding obstruction causes arbitrary shading patterns. The nonlinear characteristic of the VIPV solar production is a significant challenge, as it leads to multiple peaks in the I-V and P-V curve, resulting in a reduced power output [92]. Examples of more complex obstructions are trees and traffic shading, caused by nearby vehicles with a greater height offset, such as trucks. This results in fluctuating measured irradiance. Even if the route and speed of a vehicle with integrated PV panels are known, the irregularity of the behaviour of nearby automobiles remains unknown in traffic-induced shadowing. Figure 5.7 depicts the randomness of this shading where the four irradiance sensors from the dynamic VITS experiment are plotted.

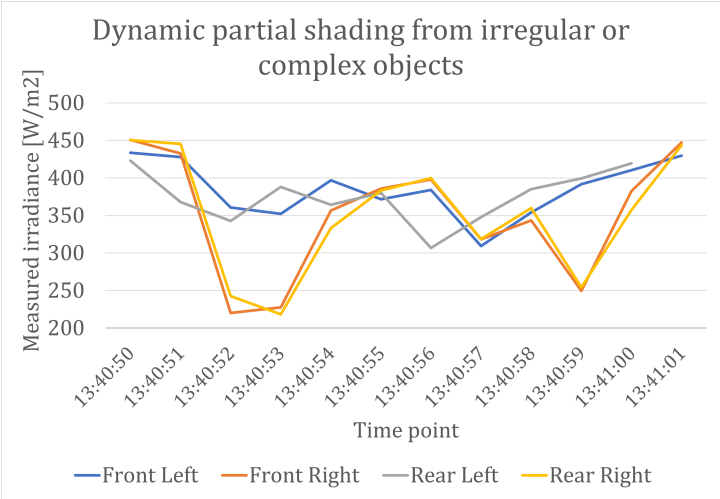

Figure 5.7: Partial shading caused by an irregular and complex object, plotted for the four irradiance sensors in the dynamic validation dataset.

The duty cycle can be optimized when considering the driving pattern and obstructions for a specific route. The solid obstructions are fixed, whereas the complex and irregular obstructions and events cannot be forecasted. An example of an irregular obstruction is a tree, where the density of leaves changes seasonally and casts different shading patterns on the solar panel.

5.2.1. MPPT losses in literature

There have been numerous research studies which investigate the partial shading impact on power electronics, especially the maximum power point tracker (MPPT). In a conference paper by Newman et al. [93], the impact of dynamic shadowing on power optimizers has been explored. It reveals that the optimizers have a big impact on the power output. In a conference paper by Zakki et al. [94], a fast distributed maximum power point

tracking technique for a rapidly changing mismatch condition is investigated. In the context of VIPV, there is a constant mismatch due to varying shadow patterns and the shading duration ranges from milliseconds to seconds. In a recent research study from TNO conducted by Dekker et al. [95], the effect of rapidly changing shading caused by rotating wind turbine blades on nearby PV panels is investigated. In this research, it was shown that the shadow of the wind turbine results in an energy loss of approximately 6% for the given period, park configuration, PV panels, inverter type and setting [95]. The loss due to partial shading depends on the speed of the moving shadow.
Moreover, in a conference paper by Araki et al. [37], an experimental study estimated a total generated energy of 2673 kWh/year for a car with a flat PV panel on the car roof. The shading of nearby obstructions caused a loss of 485 kWh, which indicates a shading loss caused by the surrounding environment of 18.1%. The MPPT losses were estimated to be 19 kWh, representing a minor loss of 0.7% compared to the shading loss by surrounding obstructions and weather effects. Due to this small fraction and considering the complexity of the MPPT algorithm, the determination of the exact MPPT losses has been left for future research.
In summary, partial shading on a PV panel results in MPPT losses and can result in other negative effects, which reduce the energy output as well. From the available literature, it is clear that the MPPT losses are dependent on the frequency, configuration, PV models, inverter type and other settings, which are left out of scope in this study.

5.3. Conclusion

Both case studies focus on public transport bus routes, given the systematic routing with a fixed timetable rather than any arbitrary route which can be driven. The case studies differ in the number of bus routes, vehicle categories, and input datasets. The differences in input datasets are driven by the key irradiance loss factors in VIPV, such as the surrounding environment, weather conditions, and the specific time and day of the year. The inputs used in both case studies, driven by the differences in irradiance loss factors, are presented in Table 5.3. By combining different datasets in both case studies, the varying shading losses are determined. The results for both case studies are presented in the following Chapter 6.

	Inputs		
	Irradiance data	**Time frame**	**Surroundings**
Bus route 40	clear sky irradiance (excluding weather effects)	around solar noon	consistent for 1 route
Bus routes of Amsterdam	averaged KNMI irradiance (including weather effects)	all hours a day	variable for 27 different bus routes

Table 5.3: Different inputs for the case studies based on the significant irradiance loss factors in VIPV: irradiance data, specific time frame, and surrounding environment.

Additionally, MPPT losses are generally lower than the annual average shading losses attributed to weather conditions and obstacles along a road. As a result, partial shading and the associated MPPT losses are not addressed in this study.

6
Results

In this Chapter, the results for both case studies are presented. Section 6.1 presents the results for the Bus 40 case study, followed by Section 6.2 which presents the results for the buses of Amsterdam case study. Finally, Section 6.3 summarizes the results and addresses the final research question: **what are the shading losses caused by key factors based on two different case studies?**

6.1. Bus 40 route: Rotterdam-Delft

This case study assesses annual shading losses for a bus and a car, using consistent inputs where only the height offset differs for both vehicle categories. Followed by the comparison between the simulated shading losses and the current TNO shading assessment, both focused on a car.

Vehicle category comparison results

This case study focuses on a public transport bus and passenger car, where the inputs presented in Table 5.1 in Chapter 5 are similar except for the vehicle height offset. The average SVF values for a car and bus are 0.74 and 0.79 along the Bus 40 route. The individual SVF values for the road survey points along this route are observed within a confidence interval of 0.35 and 1. This gives a prediction of the interval in which the SVF might be with 95% certainty [87]. The mean and confidence interval are visualized in the box plot in Figure 6.1. The presence of outliers, attributed to discrepancies originating from LiDAR data, is also visible in this plot. The SVF values correspond to the values obtained in the study of Araki [15]. As indicated in Table 2.1, the range for open and urban areas is between 0.55 and 0.95. Therefore, it is verified that this route includes various environments.

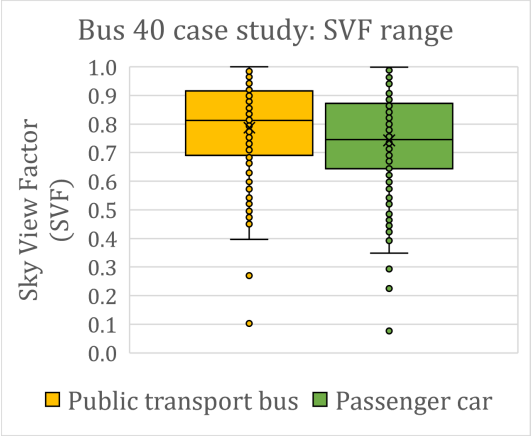

Figure 6.1: Box plot illustrating the SVF ranges for both a car and bus along Bus route 40, with average SVF values of 0.74 for a car and 0.79 for a bus.

As a next step, the varying shading indicators, SF and SVF, are combined with the clear sky irradiance in order to simulate the monthly incident irradiance. Table 6.1 presents the percentage difference in SF, SVF and yearly average shading losses for both vehicle categories.

	Passenger car	**Public transport bus**	**Percentage difference (%)**
Average SVF [-]	0.743	0.787	5.75% *(relative)*
Average SF [-]	0.681	0.734	7.49% *(relative)*
Annual average shading loss [%]	27.7%	22.7%	5% *(absolute)*

Table 6.1: Average varying shading indicators, SVF and SF, for both vehicle categories and the annual average shading loss values for Bus route 40

Plotting monthly shading losses reveals sinusoidal-like curves. Figure 6.2 shows shading loss curves for a bus and a car with similar shapes. However, shading losses for a passenger car are observed to be higher due to a larger visibility angle (ϕ) of the car compared to the bus: ($\phi_{car} > \phi_{bus}$). In this study, the visibility angle refers to the angle between the horizontal plane of the installed PV panel and the line-of-sight to the nearby obstruction, as shown in Figure 6.3. As a result, the annual average shading loss is estimated 5% higher for a car compared to a bus.

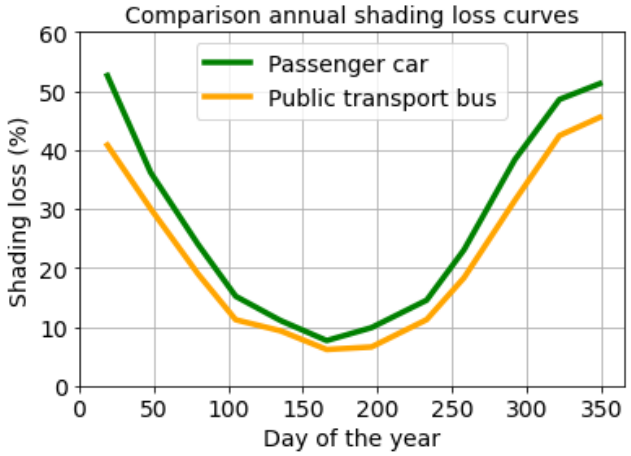

Figure 6.2: The annual shading loss curve for a passenger car (green) and public transport bus (yellow) driving the Bus 40 route.

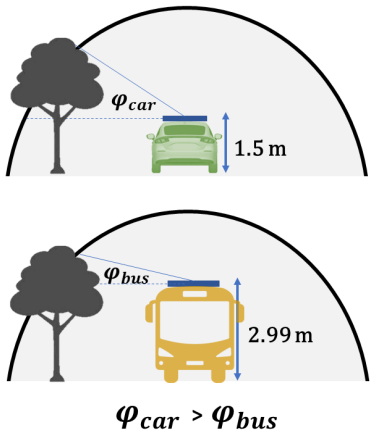

Figure 6.3: Difference in visibility angle (ϕ) for the passenger car and public transport bus for the same obstruction.

Comparison with TNO's shading assessment

The shading loss values from TNO's shading assessment, based on the case study of Cobbenhagen [11], and simulated shading losses for the Bus 40 route have been compared. Both for a passenger car with a height offset (h_{offset}) of 1.5 meters. The annual average shading loss for Cobbenhagen is 27%, and the simulated Bus 40 route has an annual average shading loss of 27.7%, resulting in a relative percentage difference of 2.6%. When looking at the monthly shading loss values, more dispersion is seen. The dispersion is caused by the differences in inputted weather data and chosen time range, where a maximum difference in shading loss is observed around summer in mid-June. Figure 6.4 illustrates sinusoidal-like curves which give the comparison between the shading losses for both cases, where the TNO's shading loss curve is presented by Equation (2.1) given in Chapter 2.

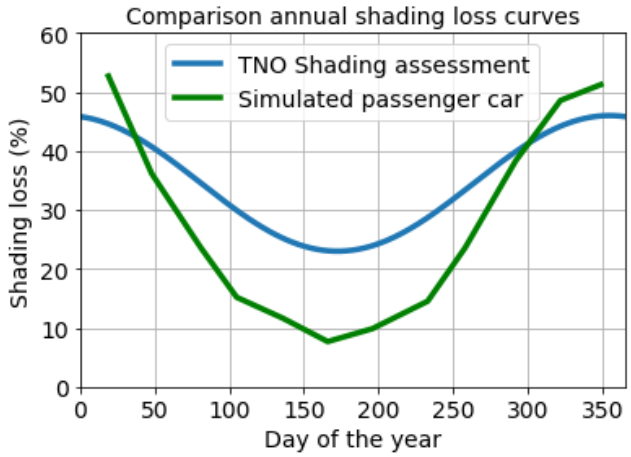

Figure 6.4: Annual shading loss curves showing the difference between the TNO shading assessment (in blue), based on the Cobbenhagen case study [11], and the simulated irradiance (in green) for both a passenger car.

TNO shading assessment represents a more smoothened shading curve compared to the simulated shading losses for Bus route 40. In TNO's current shading assessment, the shading losses range in a simplified sinusoidal relation from a minimum of 46% during the winter months to 23% during the summer months. For the simulated shading losses in this case study, the minimum and maximum values are more divergent, resulting in an average shading loss of 51% in winter and 14% in summer. The shading curve deviations for

both studies, Cobbenhagen and this simulated case study, are closely tied to differences in key factors.

Firstly, the shading factor (SF) is influenced by surrounding obstructions and the selected time frame. Figure 6.5 illustrates discrete SF values for the simulated case study, indicating solar obstruction in the months of June and December. The simulated Bus 40 case study only focuses on a time around solar noon, in contrast to TNO's shading assessment which accounts for all hourly values throughout the year, including those in the early morning and late afternoon when the Sun is lower on the horizon and more likely to be obstructed. This results in a shading factor (SF) of 0 more often, which translates into a smoother shading loss curve for TNO compared to the Bus 40 case study. When comparing the results with the dynamic validation dataset, as discussed in Chapter 4, a significant SF dependency is also observed. This case study and the dynamic validation study are both primarily centered on routes around solar noon.

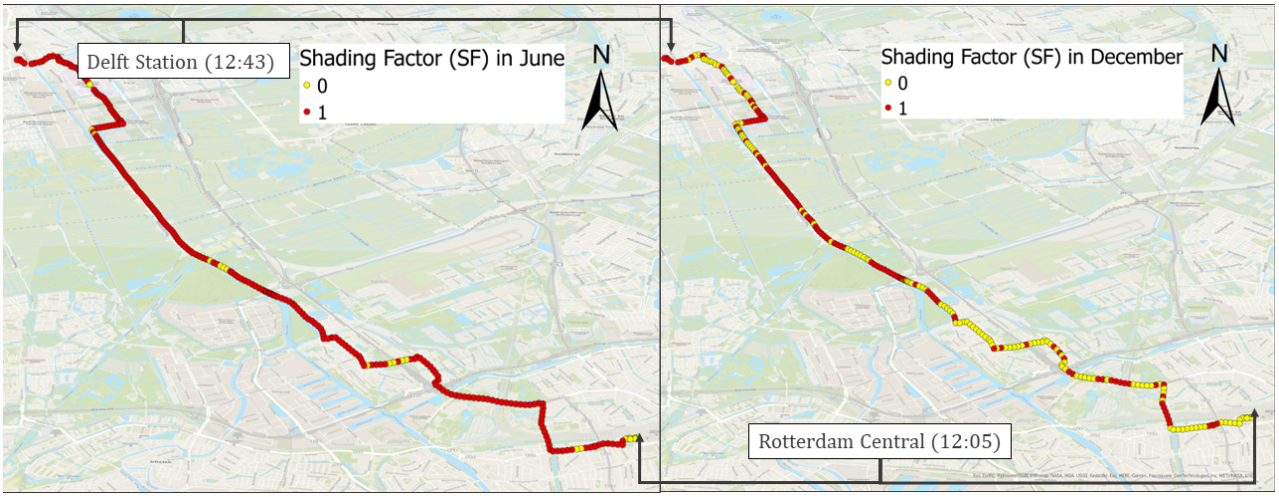

Figure 6.5: Discrete shading factor (SF) values for the months June (left) and December (right) in the Bus 40 case study, travelling from Rotterdam Central to Delft Station.

Secondly, unlike Cobbenhagen's use of historical KNMI data, which includes weather effects such as clouds and rain, this study uses clear sky irradiance data, excluding weather effects. This difference results in a different proportion of direct and diffuse irradiance. The simulated irradiance for Bus 40 with clear sky irradiance around solar noon results in a higher dependency on DNI. This leads to a strong dependence on the SF value in the irradiance calculations and this is reflected in the simulated shading curve. Figure 6.6 illustrates the positive correlation between the average SF value and monthly average irradiance, which verifies the SF dependency.

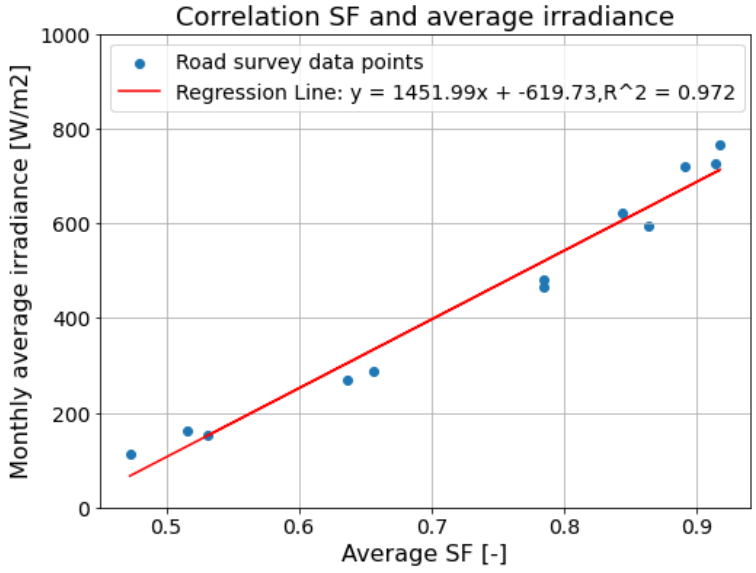

Figure 6.6: Correlation between average SF and monthly average irradiance (in W/m^2) for the Bus 40 case study, where R^2=0.972.

6.2. Bus routes of Amsterdam

The results obtained for the bus routes of Amsterdam case study are presented in this Section. The irradiance calculations are performed using averaged KNMI weather data. Averaging has a smoothing effect on sudden weather fluctuations, allowing for more realistic irradiance values but without noise from weather influences such as clouds. The averaging approach for this case study is explained in Chapter 5. As a result, comparing the impact of surrounding obstructions is more feasible, as opposed to using historical irradiance data with significant fluctuations caused by weather effects.
The amount of solar irradiance received for each individual road survey point, given as W/m^2, has been computed. By combining and averaging all the road survey points within a specific route, a monthly averaged irradiance value can be obtained for each individual bus route. The monthly average irradiance values for the 27 bus routes are shown in Figure 6.7.

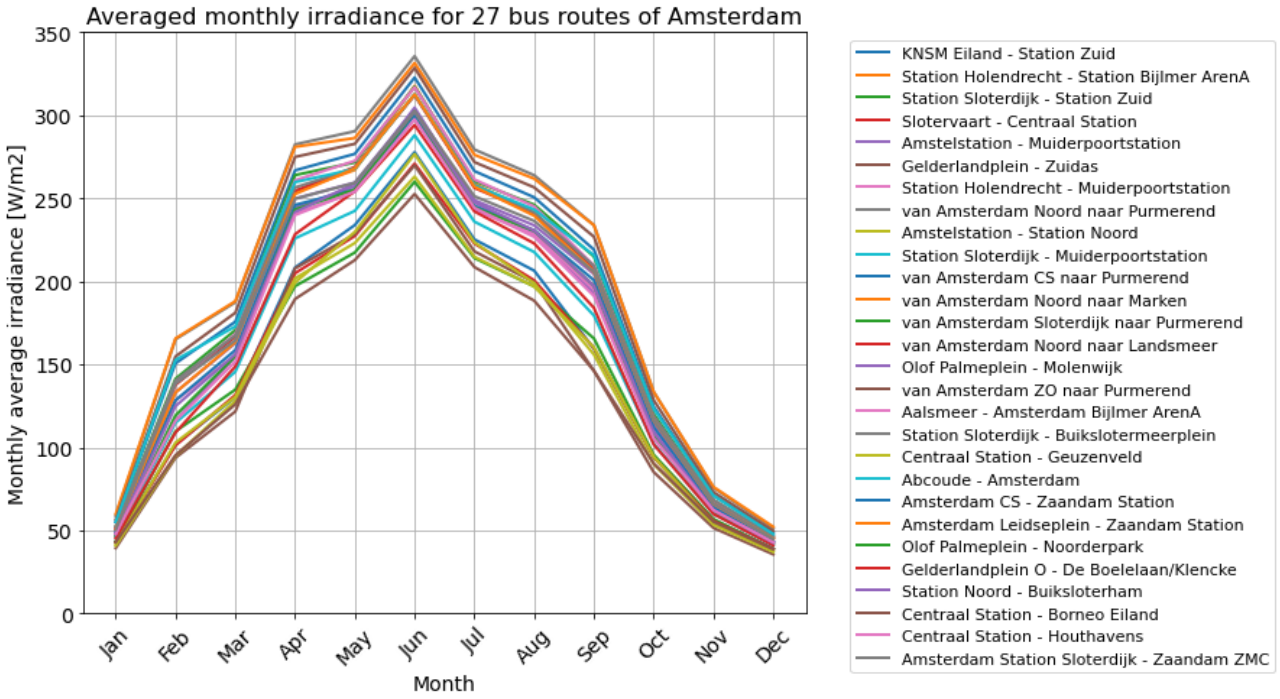

Figure 6.7: Monthly average irradiance for the 27 bus routes of Amsterdam, using averaged KNMI weather data, where the irradiance values (in W/m^2) deviate for different bus routes.

The differences in the graphs are only due to variations in the surrounding environment, as the irradiance data and time frame are the same for all routes. The differing inputs for each road survey point are the varying shading indicators, SVF and SF. Therefore, by looking at the deviations in the graphs, it is observed that the surroundings indeed affect the incident irradiance.
The shading losses have been simulated for the 27 bus routes. The annual average shading loss for all 27 bus routes accounts for 24.8%. Figure 6.8 shows the average annual irradiation for all bus routes on a geographical map. The annual irradiation value for each road survey point, given in kWh/m^2/year, has been interpolated to visualize the irradiation potential of the route. The interpolation of the road survey points is obtained using the ArcGIS workflow presented in Appendix D.
Given that each bus route has a unique time schedule and duration, the comparison between the bus routes is based on annual irradiation values, in kWh/m^2/year, for an equal comparison based on their incident irradiance potential. For each bus route, the average SVF value and average annual irradiation are determined and presented in Table J.1 in Appendix J. In addition, other characteristics, such as the different bus durations and lengths, are presented in the same Table J.1 in Appendix J. The lowest annual irradiation is for the shortest bus route from Gelderlandplein to De Boelelaan within 5 minutes. This bus routing mainly drives in the middle of tall offices and buildings, resulting in a low annual irradiation of 116.10 kWh/m^2/year and an average SVF of 0.11. In contrast to the bus route driving from Amsterdam Noord to Purmerend, which has the highest average annual irradiation of 975.13 kWh/m^2/year, as the route is mainly through a large open area resulting in an average SVF of 0.94.
Given the multiple routes, including many road survey points, the SVF correlation is investigated for the annual irradiation and surrounding terrains, using the results obtained in this case study.

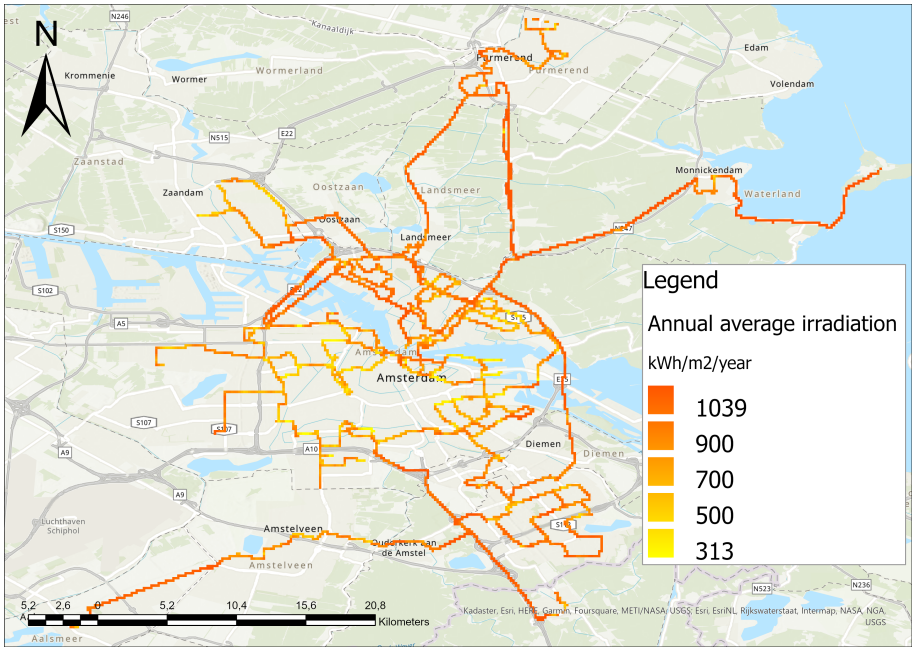

Figure 6.8: Annual average irradiation for the 27 bus routes of Amsterdam, shown on the geographical map.

Annual irradiation approximation using the SVF

The SVF values, obtained for all 3018 road survey points, have a clear correlation with the corresponding average annual irradiation. Figure 6.9 illustrates the positive correlation between the SVF (independent variable) and the average annual irradiation (dependent variable), where all 3018 data points are included.

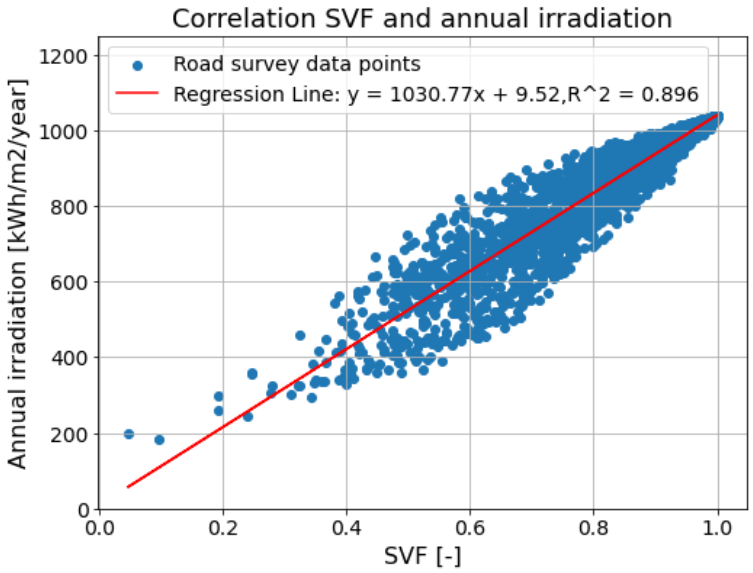

Figure 6.9: Correlation between SVF and annual irradiation for each road survey point, in the case study for the 27 bus routes of Amsterdam, where R^2=0.896.

.

In this case, the obtained R^2 of 0.896 indicates a strong linear correlation with some variation around the regression line [96]. Variability around the regression line is caused by differences in height and orientation of surrounding obstructions for a similar SVF. Obstructions in different orientations can result in the Sun being obstructed or visible more often, leading to different SF values. This is further discussed in Chapter 7.
From Figure 6.9, the linear regression equation is given as $y = 1030.77x + 9.52$. Where y corresponds to the annual irradiation (given in kWh/m^2/year) and x is the SVF value. To verify the results and trend line presented in this graph, the annual irradiation values are determined for SVF of 0 and 1. The computation of the average annual irradiance is based on the assumption of a horizontal, 0-degree tilt photovoltaic (PV) panel, enabling a direct comparison of the total GHI value.

For a SVF of 1, which is the case for an unobstructed horizon, the average annual GHI is 1047.28 kWh/m^2. When comparing the average annual irradiance using the regression equation (for a SVF of 1) with the total average GHI value, a slight difference can be seen, resulting in a SVF of nearly 1: $\frac{1040.29}{1047.28} = 0.993 \approx 1$. Furthermore, a SVF value of 0 indicates a car being parked in a closed garage for the entire year. In this specific case, it is expected the PV panel receives no irradiance. For $x = 0$ in the linear regression equation, the annual irradiation is calculated to be 9.52 kWh/m^2/year. This does not completely align with the expectancy of no irradiance being incident in the garage; however, the difference is small. A possible cause is the presence of reflected irradiance, which is not eliminated for a SVF and SF value of 0 and represents an inaccuracy in the model. Additionally, outliers with SVF values close to 0 still reach approximately 200 W/m^2. By taking one of the outliers as an example, a small stroke unobstructed sky area is visible, particularly in the southeast direction in the skyline profile. On most days of the year, the Sun reaches this unobstructed area shortly before solar noon. During this time, solar irradiance is close to its peak, leading to a higher average annual irradiance than the regression line, emphasizing the significance of orientation in these outlier scenarios. In this particular instance, the outlier data point results from a simulated road survey point which had a coordinate offset from the intended road in ArcGIS. By considering an uncertainty factor for GPS offsets, presented in the sensitivity analysis on offsets leading to different SVF values in Chapter 4, the dispersion of the outlier data point can be corrected and eventually will lead to a better fit.

SVF approximation using terrain types

This study investigates whether the terrain types can give a proxy of the SVF, as a reversed approach to Araki [15]. In Chapter 3, Section 3.6, the method for determining terrain types around a road survey point. For example, for a road survey point with XY coordinates (52.347565, 4.914474) in Amsterdam, the SVF is 0.69, indicating 31% sky visibility. The terrain breakdown within the buffer is 42% residential, 41% business park, 12% traffic terrain and 5% water. The predominant environments are residential (42%) and urban (41%). When verifying the SVF with typical SVF values presented in the research of Araki et al. [15], for residential (0.75) and urban (0.55), it can be seen that the respective SVF lies within this range of 0.55-0.75. Figure 6.10 presents the correlation between SVF and the percentage of built area intersected by the buffer.

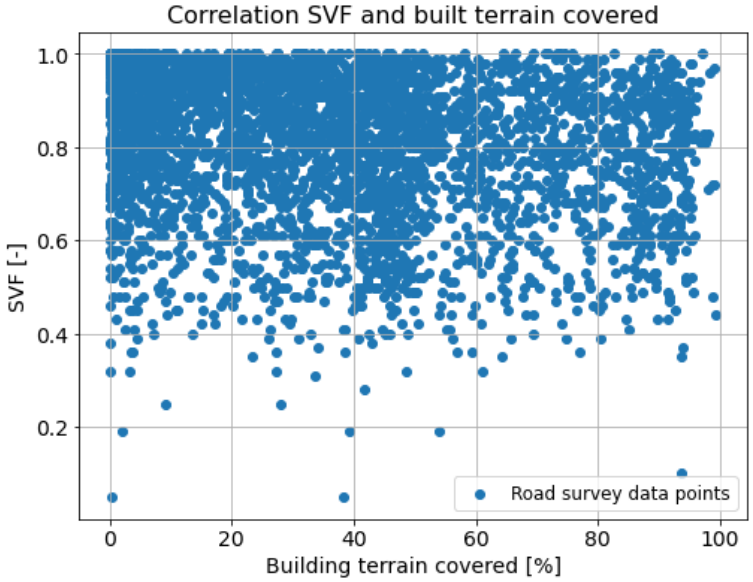

Figure 6.10: Correlation between SVF and built terrain covered (%) for each road survey point in the bus routes of Amsterdam case study.

.

In this correlation graph, significant dispersion in values can be seen. For areas with a low fraction of building terrain within a buffer (<10%), the point density is higher around an SVF of 1, indicating fewer buildings and more sky visibility. This is a logical observation; however, the data points are widely scattered. As a result, there is no clear correlation between the percentage of built terrain covered (independent variable) and SVF (dependent variable), meaning that no proxy can be given for SVF using the terrain types from the topographical BBG (land use) map [96]. This result is due to the SVF's sensitivity to obstruction heights, ranging from low-rise houses to high-rise buildings.

6.3. Conclusion

In this Chapter, the following research question has been addressed: **What are the shading losses caused by key factors based on two different case studies?**

In the first case study, based on the Bus 40 route, clear sky conditions and a time around solar noon are considered as inputs for the simulation of both bus and car, where the annual average shading losses resulted in 22.7% for the bus and 27.7% for the car. This results in an absolute difference of 5% in shading loss due to a higher height offset for the bus than the car. Moreover, the TNO shading assessment is compared with the simulated shading losses, using the same height offset but different input parameters. The comparison results in two different sinusoidal-like shading curves, where the minimum and maximum of the simulated shading losses are more divergent. However, comparing the annual average shading loss used by TNO (27%) and simulated for the Bus 40 route (27.7%) results in a small value of 2.6% relative difference. Finally, the clear sky irradiance, excluding weather effects, affects the irradiance decomposition and results in a correlation between average SF and irradiance for the Bus 40 case study.

In the second case study, the yearly average shading loss for all 27 bus routes in Amsterdam is 24.8%. The differences in the shading losses within each bus route are due to variations in the surrounding environment, represented by the varying shading indicators SVF and SF, as the irradiance data and time frame are the same for all routes. In the Amsterdam case study, a positive SVF-annual irradiation correlation was found, while using classified terrain types to give a proxy of the SVF resulted in no correlation.

In conclusion, as stated in the validation studies in Chapter 4, averaging is chosen to compare results in this work, which again shows alignment in the comparison between shading loss values. The key results for both case studies are summarized in Table 6.2.

Case studies	**Number of bus routes**	**Annual average shading loss [%]**		**Correlation**	
		Passenger car	Public transport bus	Irradiance	Terrain type
Bus route 40: Rotterdam-Delft	1	27.7%	22.7%	Positive correlation with SF (R^2 = 0.972)	X
All bus routes of Amsterdam	27	X	24.8%	Positive correlation with SVF (R^2 = 0.896)	No correlation

Table 6.2: Key results of the two performed case studies, based on the annual average irradiation and investigated correlations, where X indicates it has not been investigated.

7
Discussion

This Section analyses the research findings and relates them to literature values, quantifies the contributions beyond state-of-the-art and discusses the limitations and outlook of this thesis. Firstly, the results of this study are compared with values in literature in Section 7.1, followed by the discussion on the performed validation and case studies in Section 7.2. The research contributions are presented in Section 7.3. Followed by Section 7.4, which discusses the limitations of this thesis work. Finally, the outlook of this study is presented in Section 7.5 and a final Chapter conclusion in Section 7.6.

7.1. Literature comparison

Different studies have examined the yearly shading losses for VIPV by considering different irradiance and location datasets. The research studies which closely align with the scope of this work are presented in Section 2.4 and used for literature comparison.

For the Bus route 40 case study, the annual shading loss for a passenger car was estimated at 27.7%, closely matching the value in Cobbenhagen's thesis, which was simulated at 27%. This results in a relative percentage difference of 2.6% between the values. Average shading loss values are comparable, but monthly values in both approaches vary due to different input datasets. Nevertheless, the monthly simulated shading values for Bus 40 align with Brito et al.'s study estimating 10% summer and 50% winter irradiance losses for EVs in Lisbon using ArcGIS [30]. In addition, Brito et al.'s study neglected vehicle heights and states a 5% point underestimation of solar potential [30]. The Bus 40 case study shows a 5% absolute percentage difference between a car and a bus. This alignment enhances the credibility of the shading loss difference for vehicle categories with different height offsets.

For the buses of Amsterdam case study, the annual average shading loss is 24.8%, averaged for all 27 bus routes. This slightly differs from the 22.7% loss for the bus in the Bus 40 case study. The simulated shading loss results align with Brito et al. [30], who estimated an average annual irradiation loss of 25% for the urban area of Lisbon. Furthermore, average annual irradiation values for different bus routes in and around Amsterdam resulted in a range of 116.10 up to 975.13 kWh/m^2/year. In a study conducted by C. Ferri [18], the PV potential for Dutch highways was simulated, where the irradiation potential for the Amsterdam roads corresponded to values from 295 up to 1060 kWh/m^2/year. The simulated irradiation values in Ferri et al.'s study [18], based on Dutch highways, are higher compared to the irradiation values for Amsterdam's bus routes. This difference can be explained by the fact that highways typically run through more open areas, whereas bus routes primarily go through residential and urban zones. Overall, the irradiance values are comparable, verifying the irradiation results in the Amsterdam case study.
Finally, in a study by Robinson [66], it was found that SVF can serve as an irradiance indicator in areas with high diffuse irradiance. This has been verified by a more recent study by Calcabrini et al. [45]. Similar to the Amsterdam bus routes case study, which represents uniformly overcast sky conditions leading to high diffuse irradiance, a positive correlation between SVF and the average annual irradiation is observed. However, reversing the approach by Araki et al. [15], approximating the SVF using a classified terrain map is not possible, as no correlation was found.

In conclusion, the variations in surrounding environments and the use of different inputs related to irradiance data and chosen time frames pose a challenge for direct comparisons. Nevertheless, shading loss values are within the same order of magnitude, and similar correlations have been identified in the literature. Differences in input datasets, which lead to different results in the case studies, are investigated in more detail in the next Section.

7.2. Discussion of the results

In this thesis, two validation and two case studies have been conducted using different input datasets to validate and produce results.

7.2.1. Validation studies

The validation of the dynamic dataset is based on one route around solar noon and a measured irradiance dataset, including weather effects. In contrast, the static dataset includes all daily hours and focuses on clear sky irradiance, excluding weather effects. In the validation studies, the measurement uncertainties, which are independent of one another, are quantified as combined standard uncertainties using data obtained from sensor specification sheets [84, 97, 98]. Other uncertainties which come into play in the validation studies are related to sensor noise, road survey point assumptions, LiDAR discrepancies and weather variability, and in most cases, cannot be quantified as they are random or untraceable errors. For example, these relate to sudden errors caused by signal noise in the GPS receiver or local cloud cover obstructing the Sun.
The comparison between measured and simulated irradiance is necessary for model validation. The difference between the average measured and simulated irradiance in the dynamic validation is approximately 14%. However, the difference between individual data points is much larger and, on average, 53%. This difference results from simulated irradiance being underestimated and/or measured irradiance being overestimated. The underestimation of simulated irradiance can be because the horizon scanning approach uses only the maximum height in the skyline profile, which does not represent any open structures such as cables and road overpasses correctly. This underestimation of simulated irradiance is preferred in contrast to overpredicting irradiance, as for the case of predicting the solar driving range, a vehicle could come to halt. Therefore, the LiDAR discrepancy in effect represents a safer option. The overestimation of measured irradiance can result from cloud enhancements and sensor inaccuracies. The differences arising from local weather variability are the largest unknown. Obtaining localized weather data is essential but challenging due to the dynamic nature of the vehicle in the dynamic validation dataset. The results demonstrate that the varying shading loss can be quantified when looking at it from a holistic perspective. However, more misalignment can be seen in the comparison between individual irradiance values. As a comprehensive analysis is beyond the scope of this thesis, therefore, this is recommended in the outlook in Section 7.5.

7.2.2. Case studies

The case study results are based on different inputs for simulating conditions, which are based on the key irradiance loss factors: weather conditions, surrounding environment, and time frame for simulation conditions. The first case study, Bus route 40, considers clear sky conditions and a route around solar noon as inputs for both buses and cars. The second case study, all bus routes of Amsterdam, considers averaged KNMI irradiance, representing uniform overcast conditions, and includes all daily hours.

Irradiance data

The irradiance output measured by KNMI or determined using the Ineichen-Perez clear sky irradiance model is Global Horizontal Irradiance (GHI), where the decomposition into DNI and DHI leads to differing contributions of the direct and diffuse irradiance in the simulated irradiance.
For the first case study, Bus route 40, clear sky irradiance for a time around solar noon outputs a high proportion of DNI (as visualized in Figure F.1 in Appendix F for the decomposition of clear sky irradiance). This results in a large dependence on the SF value for the simulated irradiance.
The second case study, focused on Amsterdam's bus routes, represents uniform overcast sky conditions. In such situations, DHI plays a more significant role and results in a larger dependence on the SVF for the simulated irradiance. The SF and clear sky irradiance correlate in the first case study and the SVF and average KNMI irradiance correlate in the second case study. However, using clear sky conditions and uniform overcast conditions does not represent realistic weather conditions and leads to a bias in the correlation.
Another point of discussion is the presence of reflected irradiance for a fully blocked skyline. The reflected irradiance is computed using Equation (2.14), where for a SVF of 0, the remaining part becomes: $G_{tot} = GHI \cdot \alpha \cdot (1-0) = GHI \cdot \alpha$. This implies that still reflected irradiance is present, even though no radiation can enter a fully obstructed environment, therefore, this term leads to inaccuracy. Besides, the albedo, given as α, is a fixed value leading to a simplification of the simulated irradiance results.
Finally, in the case of making a design decision or predicting the supplied solar energy to the vehicle for estimating the solar driving range, all (extreme) weather conditions should be considered instead of one averaged irradiance value.

Surrounding environment

Within the bus routes of Amsterdam case study, the irradiance components and factors, such as the GHI, DNI, DHI, F1, and α, are assumed to be similar for simulating irradiance. The remaining variables in simulating irradiance are the varying shading indicators (SVF and SF). The SVF and SF depend on the generated skyline for a specific point. Due to the uniqueness of each skyline, similar SVF values can lead to different SF values. An example is shown in Figure 7.1, where two skylines with the same SVF of 0.71 lead to different SF values

and, thus, different irradiance values. To illustrate this, a road survey point with SVF=0.71 can have an average annual irradiance of approximately 600 kWh/m^2/year. In contrast, a different point with a similar SVF has an average annual irradiance of approximately 800 kWh/m^2/year. This leads to variability around the regression line in Figure 6.9 [96].
Furthermore, no correlation is observed between the percentage of built terrain covered and SVF, meaning that no proxy can be given for SVF using the classified terrain types. An explanation for the large spreadability in results is the changing obstruction heights. As an example, the portion of a specific terrain type can be similar for two skylines, say 50% of built terrain, however, the corresponding SVF can highly differ. To give an example, one skyline consists of 50% low-rise buildings, whereas the other 50% of skyscrapers. Since each terrain, building, and tree is unique, no proxy for a SVF can be given using the portion of terrain type. Figure 7.1 illustrates that for a similar SVF, the portion of built terrain can still differ. The values for the SVF, SF and portion of built terrain for this example are shown in Table 7.1.

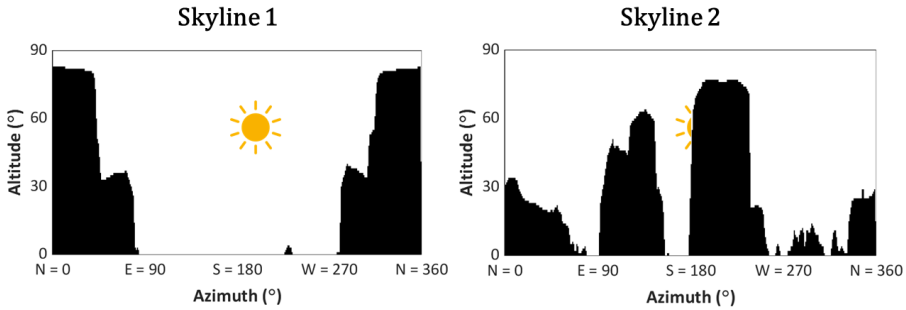

Figure 7.1: Illustrative example of two skyline profiles with a similar SVF value and the same position of the Sun, resulting in a different SF value and portion of built terrain (%)

	Skyline 1	Skyline 2
SVF	0.71	
SF	1	0
Portion of built terrain (%)	45%	61%

Table 7.1: Values for the two skyline profiles in the illustrative example

Furthermore, the surrounding environment along a route is identified by scanning the horizons of multiple road survey points. In some cases, similar to the experimental GPS offsets, deviations can occur in the simulated route. In the Amsterdam case study, an error has arisen in the polyline from the converted GTFS route data [88], resulting in a route error. Consequently, the skyline has been scanned incorrectly. To illustrate, one of the outliers in the correlation plot in Figure 6.9 is affected by this phenomenon. Figure 7.2 displays the error in the simulated bus route and the erroneous skyline. In this skyline, there is a small stroke of visible sky in the southeast direction. This leads to direct solar radiation being present slightly before solar noon and resulting in higher irradiance levels. As a result, the annual irradiation is approximately 200 W/m^2 for a SVF of 0.05. Given that this value is based on an erroneous skyline in the first place, this outlier point should not be considered.

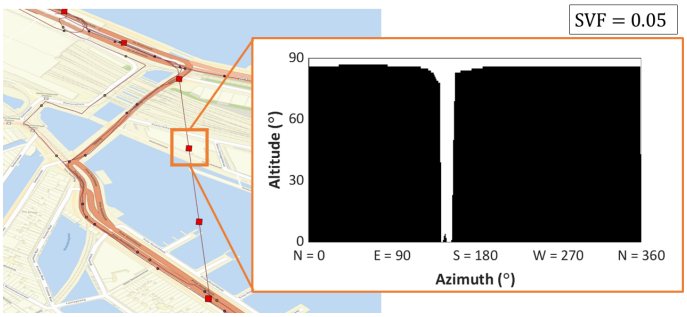

Figure 7.2: Illustrative example of a route discrepancy in one of the bus routes of Amsterdam, leading to an erroneous skyline.

Time frame

The chosen time frames for simulating conditions differ for both case studies. When all hours of the day are

included, from early mornings to late afternoons, the Sun is low on the horizon and the SF will likely result in 0 more often. This leads to lower overall incident irradiance and a smooth annual shading curve. When looking at a specific time frame around solar noon, the impact of surrounding obstructions is more significant as the Sun is the highest of the day. In the Bus 40 case study, variations in time frames result in monthly shading loss differences between the TNO shading assessment and the simulated shading loss as presented in Figure 6.4. These differences are essential to consider when making design decisions for VIPV systems. For example, a car driving around solar noon on Bus route 40 would halt in the winter months as TNO's shading assessment predicts an overestimation in incident irradiance. Similarly, overestimation of incident irradiance in the summer months can also occur by using the simulated irradiance values. Therefore, considering multiple time ranges is necessary to obtain a safe scope for estimating the incident solar irradiance.
Finally, when comparing the annual average shading losses for the case study on Bus 40, bus routes in Amsterdam, and TNO's yearly average shading value, similarities are observed despite using different inputs. Averaging filters errors and uncertainties, resulting in small differences between shading loss values.

7.3. Contribution to beyond state of the art

This research improves TNO's current VIPV shading assessment by incorporating a location- and time-specific model that can input diverse datasets, which contributes to a better estimation of the VIPV energy yield. By using different datasets, such as irradiance data for conditions from clear skies (okta 0) to complete overcast (okta 9), a more precise assessment is ensured compared to a fixed shading loss value, which might lead to overestimation or underestimation of VIPV irradiance loss.
Furthermore, the efficiency of the state-of-the-art approach is enhanced by eliminating the manual operation of downloading DSM tiles. Instead, data is extracted directly via a URL link using the Web Coverage Service (WCS) application [77], enabling quicker operation.
The horizon scanner approach has previously been applied in the research of Keijzer [65], Ferri et al. [18], and De Jong et al. [26], where the performed case studies focused on different outputs and were based on one specific case study. The case studies performed in this work incorporate different time ranges and datasets, including the Clear Sky Ineichen-Perez model [54] and averaged KNMI weather data [55], providing a more comprehensive understanding of the varying shading losses. This approach sets this work apart from studies focusing on a single case study or dataset, building upon varying shading loss research in VIPV.

7.4. Limitations

In this Section, the limitations of this study are addressed and discussed. By identifying the shortcomings of this research, potential solutions can be investigated.

Experimental data
Firstly, there is a lack of experimental data available for model validation. The dynamic validation dataset only covers one day and contains errors and uncertainties. Secondly, many uncertainties are untraceable, such as local weather effects and traffic shading, but also signal noises, which are random errors. The unknown factors lead to no fixed correction factor to apply to the model, lacking model validity. Besides, shading loss values are averaged to even out outliers and uncertain data points, which leads to the potential loss of valuable information. Furthermore, the static pyranometer validation data did not provide a good enough example for seeing the reduction in irradiance by the Sun being blocked behind the high obstruction since the position of the high obstruction was orientated in the North(-East) direction. As the position of the Sun, over a full year, does not pass the North azimuth, this example data is limited to precisely show shading where an obstruction blocks the Sun.

Partial shading
Secondly, this work assumes one calculation point on the PV panel where solar irradiance is assumed to be uniformly distributed. In reality, obstructions surrounding a moving VIPV cause partial shade on the PV panel. Partial shading on a PV panel results in MPPT losses and can result in other negative effects, which reduce the energy output as well [95]. From the available literature, it is clear that the MPPT losses are dependent on the frequency, cell interconnection and configuration, PV models, inverter type and other settings, which are left out of scope in this study. This is a limitation of the model as it should investigate how this affects the irradiance losses on PV cell level to provide a PV energy yield estimation.

LiDAR discrepancy
Thirdly, the discrepancy in utilizing LiDAR height data arises from its limitation in accurately representing open structures and seasonally varying obstructions. In reality, sunlight can pass through these objects, yet skyline profiles only consider the maximum height of obstructions. This implies a shortcoming in the model's accuracy.

Another limitation is that LiDAR only captures stationary obstructions in a DSM and does not consider aspects which change in time, such as traffic shading. In reality, traffic shading will result in a drop in measured irradiance, whereas this phenomenon is not reflected in the simulated irradiance, leading to misalignment in the results.

Road survey points
Fourth, the spatial road survey points lack information regarding driving behaviour and live traffic conditions. Variations in surroundings for different routes lead to divergent SVF outcomes. Therefore, the temporal and spatial road survey point comparison is not valid for all cases, limiting the credibility of the sensitivity analysis in this study. Next to this, a limitation arises for road survey points which experience an offset, experimentally due to signal noise or in a simulated environment due to an offset in the created polyline in ArcGIS. This leads to incorrectly generated skylines and, thus, irradiance values simulated incorrectly. Lastly, the starting point of the spatial road survey points can lead to differences in skylines. For a different shift of spatial points, over- or underestimation can be obtained in the surrounding skyline and indirectly in the SVF. This is a limitation to the spatial road survey points, which can unknowingly filter certain skylines, where an example is given in Figure 7.3.

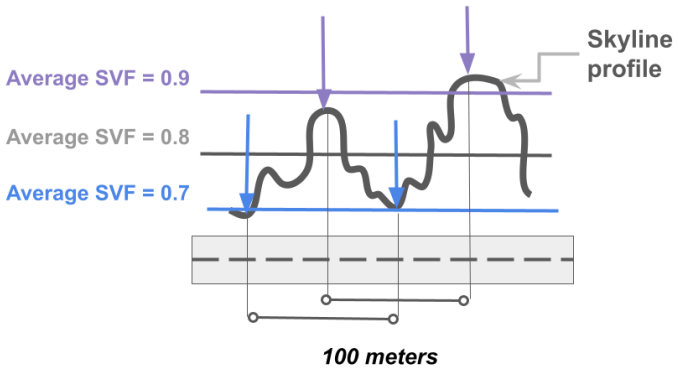

Figure 7.3: Differences in skylines along a route for different spatial starting points, resulting in differences in the SVF.

Topographical map
By using only one specific topographical map in this work, the full range of information, such as open and seasonally changing obstructions, cannot be captured and is a limitation of this work.

Criteria analysis
Moreover, the comparison for different modelling approaches is conducted using a multi-criteria analysis, where a non-systematic and standardized approach was used for selecting the criteria. Choosing criteria based on pre-existing notions can introduce confirmation bias. This may lack the objectivity of the evaluation and is a limitation to this thesis work.

Irradiance data and calculations
Furthermore, limitations in this work arise from various factors and choices related to irradiance data and calculations. The averaging of KNMI weather data and taking the irradiance losses relative to this average leads to a weather bias. Using different irradiance datasets, which include or exclude clouds and other weather effects, results in unrealistic conditions and less consistency between both case studies. This leads to no one-to-one comparison between the case studies and is, therefore, a limitation of this research. In addition, the Erbs diffuse decomposition model is more simple compared to other models such as DISC, DIRINT, and Reindl 3 [99]. These models include other variables, such as mean flux and relative humidity, which attempt to simulate the variations in diffuse irradiance more accurately [99]. Moreover, one albedo value is used to compute incident irradiance, even though the environment changes dynamically in VIPV. This leads to a simplification in this work.

Research scope
Lastly, the scope of this research is limited to only a horizontal and flat PV panel, where the case studies are performed for The Netherlands. In this study, PV panel interconnections, vehicle dimensions, and other characteristics are not considered. Consequently, predicting VIPV energy yield and its impact on the extended driving range is beyond the scope of this research, which focuses solely on irradiance losses. The VIPV energy yield estimation warrants investigation in future work.

In summary, the assumptions and decisions in this thesis come with limitations. The next Section explores ways to improve these limitations, enhancing model accuracy and applicability for future work.

7.5. Outlook

This Section looks ahead, derived from the insights and findings of this thesis, presenting an outlook. The outlook emphasizes enhancing the accuracy and applicability of the model.

Accuracy

Firstly, by conducting more experiments, the uncertainty of values in the validation dataset can be reduced. For model validation, more extensive datasets are necessary as the day-to-day variations are significant. It is recommended to collect more experimental VIPV data for various routes, driving in different surrounding environments, weather circumstances and time frames. It is recommended to repeat measurements under constant conditions, systematic errors can be identified and corrections can be quantified, which can be applied [83]. This enables the detection of outliers and unidentified data points, allowing for an assessment of whether they are systematic or random errors. As a result, a more precise model validation approach is achieved.

Secondly, by delving into more detail, experiments containing more irradiance sensors can help identify partial shading losses. The model could be combined with an electrical optimization tool to predict the best electrical configuration for a set of shading scenarios [37]. Another option to evaluate varying shading on PV cell level, without needing more irradiance sensors, would be to integrate the area enclosed by the four sensors to determine the difference in irradiance and predict a shadow pattern. However, uncertainties may still be present, as the exact pattern is not completely traceable. In conclusion, next to the need for more experimental data collection, evaluating multiple points on the panel for partial shading analysis is recommended for future work, preferably using more irradiance sensors.

Thirdly, different obstruction types are affected by the discrepancy in LiDAR data. To obtain a correctly scanned horizon for obstructions such as road sign overpasses, power line cables, and bridges, a line-of-sight tool is recommended. By using Google Earth datasets or other tools which show obstructions in 3D, unlike the limited skyline representation using LiDAR data, a more detailed view can be given. Furthermore, trees and vegetation change seasonally in opacity. A correction factor which quantifies the seasonal variability of obstructions that incorporates changing vegetation densities, growth potential, and environmental factors could be addressed. This requires in-depth study and understanding of the climate and environmental sciences, focusing on tree types and quantities. Moreover, LiDAR discrepancies can occur for tunnels. A logical solution involves using datasets containing tunnel information and using geospatial tools, filtering the tunnel points or assigning them with a SVF and SF of 0.

Fourth, to improve accuracy, it is recommended to mimic driving behaviour and real-time traffic in the road survey points rather than constant distances between the points, assuming a constant driving speed. Options for including time-related aspects in road survey points is the usage of Google Maps Routes API (Application Programming Interfaces), which includes the real-time traffic in a route of interest [100]. Moreover, the integration of bus time schedules can estimate the varying shading losses more precisely by using the bus stops and time points as an indication to recreate the bus route and determine the time-based road survey points.

Next to the recommended usage of more topographical maps for the terrain type classification, different maps can be useful for identifying road survey points with an offset outside the intended road. This can be achieved by overlaying roads and polylines more accurately, as well as providing more information on open and seasonally changing structures to overcome the LiDAR discrepancies. On top of that, topographical maps can be useful for indicating the type of obstructions to obtain a more realistic albedo value and for the identification of hilly terrain, where this work assumes the entire area of The Netherlands is flat terrain and thus no other PV panel orientation than flat. Topographical maps have a variety of uses and, therefore, should be considered in future research.

Finally, the irradiance simulation and chosen input datasets introduce inaccuracies in the results. Related to irradiance simulations, it is recommended to investigate a more accurate decomposition model which decomposes GHI into DHI and DNI and considers more factors than the Erbs decomposition model [53]. For the bus routes of Amsterdam case study, the irradiance losses are determined relative to the average. Related to the different input datasets, it is recommended to not only consider the average but also examine the high fluctuations in irradiance caused by extreme weather conditions, such as sunny weather and heavy rainfall, to ensure that the driver is not caught off guard due to an incorrectly estimated shading loss. In future research, this aspect should be considered more in the irradiance calculations. Another possibility would be instead of averaging the irradiance data, data can also be collected using a Test Reference Year (TRY). In this case, different datasets of individual months are collected and compiled to represent typical weather conditions for a location. Another option to incorporate the diversification of weather conditions could be a factor based on historical data. This factor should represent the different and extreme shading conditions caused by categorized weather conditions.

Applicability and scalability
As the scope of this research is limited to The Netherlands, expanding the application of the improved shading model to locations abroad is recommended. To make this approach more scalable, height data for a specific location is necessary. Many countries provide Digital Surface Model (DSM) data, some freely accessible. The Joint Research Centre (JRC), part of the European Commission, has published a technical report that presents countries in Europe which have non-commercial LiDAR data and an established WCS request available. Incorporating height datasets from international locations represents a valuable direction for future research.
To broaden the research scope, it is necessary to address and build on assumptions and decisions made in this work. The multi-criteria analysis was selected as the most suitable method within the given time frame of this literature study. However, it is crucial to acknowledge that choosing criteria based on preconceived notions can introduce confirmation bias. For future research, a more comprehensive comparative study is recommended, which can be achieved by looking into more extensive datasets which can accurately represent the surrounding obstructions. Integrating both qualitative and quantitative approaches leads to a more validated methodology.
Another assumption of this work was a flat PV panel, where for future work, it is essential to consider curved PV panels and the inclination angle of PV panels, for example, when integrated into the sides of a vehicle. The 2D VF model methodology by Calcabrini holds potential for PV panels with different orientations, particularly in complex environments [45].
Lastly, to estimate the PV energy yield for a VIPV driving a particular route, it is crucial to consider both thermal and electrical models. As a next step, this can provide guidance to drivers for choosing the most optimal routes which enable the highest and most efficient solar energy generation without the need for charging from the grid. This can improve the applicability of the modelling method.

7.6. Conclusion

The varying shading losses depend on the route, differing in the surrounding environment, and different input datasets for simulating conditions based on the type of weather data and chosen time frame. The validation and case studies yield different insights, where the input datasets for the three key factors are summarized in Table 7.2.

		Inputs		
		Irradiance data	**Time frame (for a year)**	**Surroundings**
Validation studies	**Dynamic dataset**	Measured & KNMI irradiance (including weather effects)	Around solar noon	Consistent for 1 route
	Static dataset	Measured & clear sky irradiance (excluding weather effects)	All hours a day	Consistent for 1 location
Case studies	**Bus route 40**	Clear sky irradiance (excluding weather effects)	Around solar noon	Consistent for 1 route
	Bus routes of Amsterdam	Averaged KNMI irradiance (including weather effects)	All hours a day	Variable for 27 different bus routes

Table 7.2: Summary of input datasets for validation and case studies

The TNO shading assessment is improved by implementing a location- and time-specific model capable of incorporating various irradiance datasets. The primary contribution, beyond the state of the art, is the WCS request in the horizon scanner, eliminating the manual extraction of DSM data.
The validation and case study results demonstrate that the varying shading effect can be quantified when looking at it from a holistic perspective. The deviations in individual values in validation studies are larger than the difference between average values. Averaging and comparing results to the total route or over the course of an entire year result in more alignment as large fluctuations, mainly caused by local weather effects, traffic shading, sensor inaccuracies, and LiDAR discrepancies, are evened out.
The assumptions and decisions in this thesis come with limitations, where an outlook is presented focusing on improving model accuracy and applicability for future work.

8
Conclusions

The constant change in irradiance presents a significant challenge within VIPV. Key factors that cause irradiance losses are based on the location, weather, and time. TNO's current shading assessment uses a fixed value to account for the surrounding obstructions and weather effects, where the only variable input is the day of the year. This study has improved TNO's current VIPV shading assessment by incorporating more variables into a new model, thereby contributing to a better estimation of the VIPV energy yield. In this study, the lost incident irradiance is referred to as shading loss. The structure of this Section is based on the three main research questions.

How to implement key factors causing shading loss to improve TNO's VIPV shading assessment? Different approaches identify the surrounding obstructions along a route, which are compared through a multi-criteria analysis using relevant criteria: scalability, accuracy, transparency, and validity. The DSM-based approach is chosen in this work as it outperforms other methods by fulfilling all four stated criteria. An improvement has been made regarding the modelling approach, replacing the manual process of DSM data extraction for a quicker operation that directly obtains data through a URL link using a Web Coverage Service (WCS) request [77]. The improved model can effectively characterize the shading losses for a route with the aid of the varying shading indicators (SVF and SF), input different irradiance datasets, including or excluding weather effects, and input the exact time and day of the year for the determining the position of the Sun. Using different datasets for irradiance loss factors, including different routes and weather conditions, enhances model accuracy and provides a more comprehensive understanding of shading losses compared to the current TNO assessment that only varies by the day of the year.

How to determine the quality of the model by validation? The quality of the model is determined through validation, which involves using two types of datasets: dynamic and static data for non-free horizon conditions ($SVF \leq 1$). The input datasets differ regarding location, time, and weather conditions for both studies. As a result, it is verified that the surrounding obstructions can accurately be represented in a skyline representation, which results in a good-quality model. However, some uncertainties can come into play when simulating the surrounding environment, known as LiDAR discrepancies. Measurement inaccuracies, assumptions, and weather variability cause the validation results to be misaligned. Weather variability is the primary factor affecting model uncertainty, resulting in no fixed inaccuracy factor. To remove outliers and unknowns, averaging is chosen to compare results in this work. This modelling approach is valid for route-level assessment, as it accurately identifies the environment. However, weather variability should be minimized when quantifying shading losses from the surrounding obstructions.

What are the shading losses caused by key factors based on two different case studies? In the Bus 40 study, simulations under clear sky conditions and time around solar noon resulted in shading losses of 22.7% for the bus and 27.7% for the car. Moreover, the simulated shading loss shows a 2.6% relative difference compared to the yearly average TNO value (27%) for a car. The average shading loss values are comparable, but monthly values in both approaches vary due to different input datasets. In the Amsterdam bus routes study, the yearly average shading loss is 24.8% based on averaged KNMI irradiance. The average SF and clear sky irradiance, as well as all SVF values and average KNMI irradiance, correlate in this research. However, using clear sky conditions or yearly averaged KNMI data for uniform overcast conditions introduces a bias in this correlation, given the larger share of DNI or DHI irradiance. Finally, classified terrain types do not correlate with SVF, in contrast to the reversed approach by Araki et al. [15].

In conclusion, the model effectively determines irradiance losses at the route level. However, it faces limitations in finer resolution, such as analyzing small route segments or partial shade. Despite this, the improved model can be helpful for different stakeholders, such as bus operators selecting routes for optimal solar energy generation and policymakers in SolarMoves [20], predicting required charging infrastructure when VIPV comes into play. Additionally, the model provides predictions of extended solar driving range by incorporating diverse datasets and can, therefore, provide a more accurate range of shading losses. This reduces the risk of overestimation or underestimation for a single VIPV shading loss value, contrasting TNO's assessment.

References

[1] Sono Motors. *'Sion' Solar-Electric Passenger Car And 'Solar Bus Kit' For Public Transportation Fleets*. https://sonomotors.com/en/press/press-releases/sono-motors-unveils-production-design-of-its-sion-and-solar-bus-kit/. 2022.

[2] International Energy Agency (IEA). *Global Electric Vehicle Outlook 2023*. 2023.

[3] European Parliament. *Car-recharging stations should be available every 60 km*. https://www.europarl.europa.eu/news/en/press-room/20221014IPR43206/car-recharging-stations-should-be-available-every-60-km-say-meps. 2023.

[4] A. S. Rodriguez et al. "A feasibility study of solar PV-powered electric cars using an interdisciplinary modeling approach for the electricity balance, CO2 emissions, and economic aspects: The cases of The Netherlands, Norway, Brazil, and Australia". In: *Progress in Photovoltaics: Research and Applications* 28 (6 June 2020), pp. 517–532. ISSN: 1099159X. DOI: 10.1002/pip.3202.

[5] SolarPower Europe. *Global Market Outlook For Solar Power 2023-2027*. https://www.solarpowereurope.org/insights/outlooks/global-market-outlook-for-solar-power-2023-2027/detail. June 2023.

[6] ITRPV. *International Technology Roadmap for Photovoltaic Report 2023, 14th edition*. https://www.vdma.org/international-technology-roadmap-photovoltaic. 2023.

[7] IEA. "State-of-the-Art and Expected Benefits of PV-Powered Vehicles 2021". In: *IEA-PVPS T17-01:2021* (2021).

[8] PWC Strategy&. *Hyperefficient EVs can help accelerate & realize the energy transition in The Netherlands*. https://www.strategyand.pwc.com/nl/en/industries/energy-utilities/hyperefficient-evs.html. 2022.

[9] K. Araki, Ota Y., and M. Yamaguchi. "Measurement and modeling of 3D solar irradiance for vehicle-integrated photovoltaic". In: *Applied Sciences (Switzerland)* 10 (3 Feb. 2020). ISSN: 20763417. DOI: 10.3390/app10030872.

[10] J. Baek and Y. Choi. "Comparative Study on Shading Database Construction for Urban Roads Using 3D Models and Fisheye Images for Efficient Operation of Solar-Powered Electric Vehicles". In: *Energies* 15 (21 Nov. 2022). ISSN: 19961073. DOI: 10.3390/en15218228.

[11] A.T.J.R. Cobbenhagen. *Performance analysis of solar cars for everyday use*. Technical University of Eindhoven (TUE), 2016.

[12] A. J. Carr et al. *Vehcile Integrated Photovoltaics Evaluation of the Energy Yield Potential through Monitoring and Modelling*. 2020.

[13] O Kanz and B. Lim. *VIPV Position Paper, Vehicle-integrated Photovoltaics (VIPV) as a core source for electricity in road transport*. 2019.

[14] E. Sovetkin et al. "Vehicle-Integrated Photovoltaics Irradiation Modeling Using Aerial-Based LIDAR Data and Validation with Trip Measurements". In: *Solar RRL* (2022). ISSN: 2367198X. DOI: 10.1002/solr.202200593.

[15] K. Araki et al. "3D Solar Irradiance Model for Non-Uniform Shading Environments Using Shading (Aperture) Matrix Enhanced by Local Coordinate System". In: *Energies* 16 (11 May 2023), p. 4414. ISSN: 1996-1073. DOI: 10.3390/en16114414.

[16] Naveed ur Rehman, Mohamad Hijazi, and Muhammad Uzair. "Solar potential assessment of public bus routes for solar buses". In: *Renewable Energy* 156 (Aug. 2020), pp. 193–200. ISSN: 18790682. DOI: 10.1016/j.renene.2020.04.081.

[17] K. Hanjin et al. "A new GIS-based algorithm to estimate photovoltaic potential of solar train: Case study in Gyeongbu line, Korea". In: *Renewable Energy* 190 (May 2022), pp. 713–729. ISSN: 18790682. DOI: 10.1016/j.renene.2022.03.130.

[18] C. Ferri et al. "Mapping the photovoltaic potential of the roads including the effect of traffic". In: *Renewable Energy* 182 (Jan. 2022), pp. 427–442. ISSN: 18790682. DOI: 10.1016/j.renene.2021.09.116.

[19] C. Lee et al. “Rapid and Effective Technology Development for 3D-Model-Based Solar Access Analysis and Comparative Study with Fish-Eye Camera”. In: *Energies* 16 (7 Mar. 2023), p. 3135. ISSN: 1996-1073. DOI: 10.3390/en16073135. URL: https://www.mdpi.com/1996-1073/16/7/3135.

[20] TNO. *Europe explores potential of solar powered vehicles — tno.nl*. https://www.tno.nl/en/newsroom/2023/02/europe-explores-potential-solar-powered/. 2023.

[21] K. Araki et al. “Solar Electric Vehicles as Energy Sources in Disaster Zones: Physical and Social Factors”. In: *Energies* 16 (8 Apr. 2023). ISSN: 19961073. DOI: 10.3390/en16083580.

[22] G. Wetzel et al. “High time resolution measurement of solar irradiance onto driving car body for vehicle integrated photovoltaics”. In: *Progress in Photovoltaics: Research and Applications* 30 (5 May 2022), pp. 543–551. ISSN: 1099159X. DOI: 10.1002/pip.3526.

[23] Sono Motors. *Mobility Powered by the Sun*. https://sonomotors.com/en/subpage-solar/. 2022.

[24] B. Commault et al. “Overview and perspectives for vehicle-integrated photovoltaics”. In: *Applied Sciences (Switzerland)* 11 (24 Dec. 2021). ISSN: 20763417. DOI: 10.3390/app112411598.

[25] L. H. Slooff, A. J. Carr, and B. K. Newman. “Proposed method for evaluation of VIPV systems”. In: *PVinMotion Conference* (2023).

[26] D. De Jong and H. Ziar. “Photovoltaic Potential of the Dutch Inland Shipping Fleet: An Experimentally Validated Method to Simulate the Power Series from Vessel-Integrated Photovoltaics”. In: *Solar RRL* (2022). ISSN: 2367198X. DOI: 10.1002/solr.202200642.

[27] A. Robert. *Cars can run on solar power*. https://www.techgyd.com/cars-run-on-solar-power/32668/. Oct. 2017.

[28] O. Myeongchan, S. M. Kim, and H. D. Park. “Estimation of photovoltaic potential of solar bus in an urban area: Case study in Gwanak, Seoul, Korea”. In: *Renewable Energy* 160 (Nov. 2020), pp. 1335–1348. ISSN: 18790682. DOI: 10.1016/j.renene.2020.07.048.

[29] N. R. Khan et al. “Solar powered UAV: A comprehensive review”. In: AIP Publishing, 2023. DOI: 10.1063/5.0127815.

[30] M. C. Brito et al. “Urban solar potential for vehicle integrated photovoltaics”. In: *Transportation Research Part D: Transport and Environment* 94 (May 2021). ISSN: 13619209. DOI: 10.1016/j.trd.2021.102810.

[31] W. Hoffmann. “PV solar electricity industry: Market growth and perspective”. In: *Solar Energy Materials and Solar Cells* 90.18-19 (Nov. 2006), pp. 3285–3311. DOI: 10.1016/j.solmat.2005.09.022.

[32] *Lightyear One*. https://lightyear.one/lightyear-0/. 2020.

[33] EV Database. *Electric Vehicle Database*. https://www.ev-database.org/. 2020.

[34] M. Heinrich, C. Kutter, and F. Basler. *Potential and Challenges of Vehicle Integrated Photovoltaics for Passenger Cars*. 2020.

[35] Justyna Pastuszak and Paweł Węgierek. “Photovoltaic Cell Generations and Current Research Directions for Their Development”. In: *Materials* 15 (16 Aug. 2022). ISSN: 19961944. DOI: 10.3390/ma15165542.

[36] New Energy and Industrial Technology Development Organization (NEDO). *PV-Powered Vehicle Strategy Committee Interim Report*. 2018.

[37] Y. Ota, K. Araki, and K. Nishioka. *Impact of the partial shading distribution on the output of the vehicle-integrated photovoltaic module PVinMotion 2023*.

[38] J. Macías et al. “On the effect of cell interconnection in Vehicle Integrated Photovoltaics: modelling energy under different scenarios”. In: *2021 IEEE 48th Photovoltaic Specialists Conference (PVSC)*. 2021, pp. 1336–1339. DOI: 10.1109/PVSC43889.2021.9518935.

[39] Fraunhofer ISE. *Vehicle-Integrated Photovoltaics into Cars*. https://www.ise.fraunhofer.de/en/business-areas/photovoltaics/photovoltaic-modules-and-power-plants/integrated-photovoltaics/vehicle-integrated-photovoltaics/vehicle-integrated-cars.html.

[40] A. H. Smets et al. *Solar Energy: The physics and engineering of photovoltaic conversion, technologies and systems*. English. UIT Cambridge Limited, 2016. ISBN: 978-1-906860-32-5.

[41] G. Wetzel et al. “Specifications for maximum power point tracking in vehicle-integrated photovoltaics based on high-resolution transient irradiance measurements”. In: vol. 2020-June. Institute of Electrical and Electronics Engineers Inc., June 2020, pp. 1124–1126. ISBN: 9781728161150. DOI: 10.1109/PVSC45281.2020.9300565.

[42] P. Gilman et al. *SAM Photovoltaic Model Technical Reference Update*. 2016, pp. 15–20.

[43] O. Isabella. *PV Systems Course, Introduction to Location Issues*. 2023.

[44] PennState College of Earth and Mineral Sciences. *Sky Dome and Projections*. https://www.e-education.psu.edu/eme810/node/534.

[45] A. Calcabrini et al. "A simplified skyline-based method for estimating the annual solar energy potential in urban environments". In: *Nature Energy* 4 (3 Mar. 2019), pp. 206–215. ISSN: 20587546. DOI: 10.1038/s41560-018-0318-6.

[46] A. Calcabrini et al. "Time-varying, ray tracing irradiance simulation approach for photovoltaic systems in complex scenarios with decoupled geometry, optical properties and illumination conditions". In: *Progress in Photovoltaics: Research and Applications* 31 (2 Feb. 2023), pp. 134–148. ISSN: 1099159X. DOI: 10.1002/pip.3614.

[47] R. Perez et al. "Modeling daylight availability and irradiance components from direct and global irradiance". In: *Solar Energy (Journal of Solar Energy Science and Engineering); (USA)* (Jan. 1990). ISSN: 0038-092X. DOI: 10.1016/0038-092X(90)90055-H. URL: https://www.osti.gov/biblio/6568615.

[48] F. F. Sönmez et al. "Fast and accurate ray-casting-based view factor estimation method for complex geometries". In: *Solar Energy Materials and Solar Cells* 200 (2019), p. 109934. ISSN: 0927-0248. DOI: https://doi.org/10.1016/j.solmat.2019.109934.

[49] A.R. Burgers, G.J.M. Janssen, and B. B. Van Aken. *BIGEYE: Accurate energy yield prediction of bifacial PV systems*. https://repository.tno.nl//islandora/object/uuid:d34d4e48-4f2d-4afe-aff8-ca5771fbc400. 2018.

[50] R. Santbergen et al. "Calculation of irradiance distribution on PV modules by combining sky and sensitivity maps". In: *Solar Energy* 150 (2017), pp. 49–54. ISSN: 0038092X. DOI: 10.1016/j.solener.2017.04.036.

[51] M. Rouholamini, Lei Chen, and C. Wang. "Modeling, Configuration, and Grid Integration Analysis of Bifacial PV Arrays". In: *IEEE Transactions on Sustainable Energy* 12.2 (2021), pp. 1242–1255. DOI: 10.1109/tste.2020.3040427.

[52] Sandia National Laboratories. *POA Sky Diffuse*. https://pvpmc.sandia.gov/modeling-steps/1-weather-design-inputs/plane-of-array-poa-irradiance/calculating-poa-irradiance/poa-sky-diffuse/.

[53] D. G. Erbs, S. A. Klein, and J. A. Duffie. "Estimation of the diffuse radiation fraction for hourly, daily and monthly-average global radiation". In: (), pp. 293–302.

[54] W. F. Holmgren, W. C. Hansen, and M. A. Mikofski. "pvlib python: a python package for modeling solar energy systems". In: *Journal of Open Source Software* 3.29 (2018), p. 884. DOI: 10.21105/joss.00884. URL: https://doi.org/10.21105/joss.00884.

[55] Koninklijk Nederlands Meteorologisch Instituut (KNMI). *Daggegevens van het weer in Nederland*. https://www.knmi.nl/nederland-nu/klimatologie/daggegevens.

[56] Y. A. Eltbaakh et al. "Solar attenuation by aerosols: An overview". In: *Renewable and Sustainable Energy Reviews* 16 (6 Aug. 2012), pp. 4264–4276. ISSN: 13640321. DOI: 10.1016/j.rser.2012.03.053.

[57] D. G. Steyn. "The calculation of view factors from fisheye-lens photographs". In: *Atmosphere-Ocean* 18.3 (Sept. 1980), pp. 254–258. DOI: 10.1080/07055900.1980.9649091.

[58] Wikipedia. *View Factor (VF)*. https://en.wikipedia.org/wiki/View_factor.

[59] W.X. Cheryl, Z. Ji, and E.R. Tay. "A Tropical Case Study Quantifying Solar Irradiance Collected on a Car Roof for Vehicle Integrated Photovoltaics towards Low-Carbon Cities". In: vol. 2020-June. Discusses results from experiments on the building orientation, the effect of the weather, how the tests were conducted etc [READ]. Institute of Electrical and Electronics Engineers Inc., June 2020, pp. 2461–2464. ISBN: 9781728161150. DOI: 10.1109/PVSC45281.2020.9300351.

[60] C. Park, J. Ha, and S. Lee. "Association between three-dimensional built environment and urban air temperature: Seasonal and temporal differences". In: *Sustainability (Switzerland)* 9 (8 July 2017). ISSN: 20711050. DOI: 10.3390/su9081338.

[61] ArcGIS 10.7. *ArcMap Projections*. https://desktop.arcgis.com/en/arcmap/10.7/map/projections/what-are-map-projections.htm.

[62] Japan Toyota Technological Institute. *Rough and Straightforward Estimation of the Mismatching Loss by Partial Shading of the PV Modules Installed on an Urban Area or Car-Roof*. 2019.

[63] C. Thiel et al. “Impact of climatic conditions on prospects for integrated photovoltaics in electric vehicles”. In: *Renewable and Sustainable Energy Reviews* 158 (Apr. 2022). ISSN: 18790690. DOI: 10.1016/j.rser.2022.112109.

[64] K. Araki, Y. Ota, and A. Nagaoka. “Matrix calculation of 3D solar irradiance”. PVSEC-34, Area 7. 2023.

[65] M. C. Keijzer. *A multi-surface reflected irradiance model for pyranometer corrections and PV yield calculations in complex urban geometries*. Master of Science (MSc), TU Delft, 2019.

[66] D. Robinson. “Urban morphology and indicators of radiation availability”. In: *Solar Energy* 80 (12 Dec. 2006), pp. 1643–1648. ISSN: 0038092X. DOI: 10.1016/j.solener.2006.01.007.

[67] D. De Jong. *Photovoltaic potential of the Dutch shipping fleet Experimentally validated method based on photovoltaic power calculations to simulate the energy yield of general cargo inland vessels*. 2020.

[68] Z. H. Jiao et al. “Evaluation of Four Sky View Factor Algorithms Using Digital Surface and Elevation Model Data”. In: *Earth and Space Science* 6 (2 Feb. 2019), pp. 222–237. ISSN: 23335084. DOI: 10.1029/2018EA000475.

[69] N. Stendardo et al. “GPU-enabled shadow casting for solar potential estimation in large urban areas. Application to the solar cadaster of Greater Geneva”. In: *Applied Sciences (Switzerland)* 10 (15 Aug. 2020). ISSN: 20763417. DOI: 10.3390/APP10155361.

[70] H. Taherdoost and M. Madanchian. “Multi-Criteria Decision Making (MCDM) Methods and Concepts”. In: *Encyclopedia* 3.1 (2023), pp. 77–87. ISSN: 2673-8392. DOI: 10.3390/encyclopedia3010006. URL: https://www.mdpi.com/2673-8392/3/1/6.

[71] Centraal Bureau voor de Statistiek (CBS). *“Mobiliteit; per persoon, vervoerwijzen, motieven, regio’s,”* https://opendata.cbs.nl/statline/#/CBS/nl/dataset/84713NED/table?dl=42841. 2022.

[72] Nationaal Georegister (NGR). *Maximum snelhedenkaart (RWS)*. https://www.nationaalgeoregister.nl/geonetwork/srv/api/records/d7df2888-0c0d-40f1-9b35-3c1a01234d01.

[73] Publieke Dienstverlening Op de Kaart (PDOK). *Dataset Actueel Hoogtebestand Nederland 3 (AHN3)*. https://www.pdok.nl/introductie/-/article/actueel-hoogtebestand-nederland-ahn. 2023.

[74] Actueel Hoogtebestand Nederland (AHN). *“AHN: The making of”*. https://www.ahn.nl/ahn-the-making-of. 2022.

[75] R. Mcgaughey, H. Andersen, and S. Reutebuch. “Considerations for Planning, Acquiring, and Processing LiDAR Data for Forestry Applications”. In: (Jan. 2006).

[76] C. Ferri. *Irradiation and DC yield potential of solar highways in the Netherlands*. Delft University of Technology (TU Delft), 2019. URL: http://repository.tudelft.nl/..

[77] J. Evans. *Web Coverage Service (WCS), Version 1.0.0 (Corrigendum)*. 2005.

[78] Centraal Bureau voor de Statistiek (CBS). *Bestand Bodemgebruik (BBG2017) Productbeschrijving*. www.cbs.nl. 2017.

[79] Physics Labs for Scientists and Engineers. *Percent Error and Percent Difference*. https://www.webassign.net/question_assets/ncsucalcphysmechl3/percent_error/manual.html.

[80] TNO. “SONOB project”. 2016.

[81] E. Peerlings. *Cloud gazing and catching the sun’s rays: Quantifying cloud-caused variability in solar irradiance*. 2019.

[82] C. A. Gueymard. “Cloud and albedo enhancement impacts on solar irradiance using high-frequency measurements from thermopile and photodiode radiometers. Part 1: Impacts on global horizontal irradiance”. In: *Solar Energy* 153 (2017), pp. 755–765. ISSN: 0038092X. DOI: 10.1016/j.solener.2017.05.004.

[83] R.R. Cook. *Assessment of Uncertainties of Measurement for Calibration and Testing Laboratories*. National Association of Testing Authorities, Australia, 1999. ISBN: 9780909307462.

[84] *Silicon Irradiance Sensor Measurement of Solar Irradiance general Information*. Ingenieurbüro Mencke & Tegtmeyer GmbH. June 2017.

[85] A. J. Carr. “A Detailed Performance Comparison of PV Modules of Different Technologies and The Implications for PV System Design Methods”. PhD thesis. Western Australia: Murdoch University, July 2005.

[86] *GPS Technical Specifications GPS 18x-5Hz*. Garmin International, Inc. Oct. 2011.

[87] Dr. W. Brinkman. *Lecture notes for IN4303: Data preparation methods*. Spring 2010.

[88] University of Groningen Geodienst. *Openbaar Vervoer Nederland*. https://hub.arcgis.com/maps/RUG::openbaar-vervoer-nederland/about. 2021.

[89] Regionaal Openbaar Vervoer RET. *Over RET: materieel en bussen*. https://corporate.ret.nl/over-ret/materieel/bus. 2023.

[90] M. W. Van Dijk. *Integrating PV systems directly on metro traction networks Focussing on the metro traction network of Amsterdam*.

[91] Gemeentevervoerbedrijf (GVB) Amsterdam. *Kennismaking cijfers met de nieuwe elektrische bus*. https://over.gvb.nl/nieuws/kennismaken-met-de-nieuwe-elektrische-bus/. 2023.

[92] P. S. Arun and S. R. Mohanrajan. "Effect of Partial Shading on Vehicle Integrated PV System". In: Institute of Electrical and Electronics Engineers Inc., June 2019, pp. 1262–1267. ISBN: 9781728101675. DOI: 10.1109/ICECA.2019.8821888.

[93] B. K. Newman et al. "Impact of Dynamic Shading in cSi PV Modules and Systems for Novel Applications". In: *2019 IEEE 46th Photovoltaic Specialists Conference (PVSC)*. 2019, pp. 3088–3092. DOI: 10.1109/PVSC40753.2019.8980544.

[94] M. Iqbal, M. Zakki, and N. Hussain. "A Hybrid Fast Distributed Maximum Power Point Tracking Technique in Rapid Mismatching Condition Tatabhatla, V.M.R.," in: *IEEE 2nd International Conference on Automatic Control and Intelligent Systems (I2CACIS 2017)*. Universiti Teknologi MARA Malaysia. Kota Kinabalu, Sabah, Malaysia, Oct. 2017.

[95] N.J. Dekker et al. "Effects of Wind Turbine Dynamic Shading on Combined Solar and Wind Farms". TNO Solar Energy. 2023.

[96] Dr. C. (Kees) Maat. *Lineaire regressie, CT3501 Het ruimtelijk systeem: mobiliteit en effecten*. Department of Transport Planning, Faculty of Civil Engineering and Geosciences, TU Delft, 2023.

[97] *IMC CANSAS SCI8, Technical Specification Sheet*. IMC Meßsysteme GmbH. Dec. 2014.

[98] *EKO MS-802 Instruction Manual*. Version 13. EKO INSTRUMENTS CO., LTD.

[99] Sandia National Laboratories and First Solar. *Evaluation of Irradiance Decomposition and Transposition Models at Locations Across the United States*. https://www.osti.gov/servlets/purl/1569197. 2014.

[100] Google Maps API Platform. *Route Optimization Planning using Real-Time Traffic*. https://mapsplatform.google.com/solutions/offer-efficient-routes/.

[101] T. Chang. "The Sun's apparent position and the optimal tilt angle of a solar collector in the northern hemisphere". In: *Solar Energy* 83 (8 Aug. 2009), pp. 1274–1284. ISSN: 0038092X. DOI: 10.1016/j.solener.2009.02.009.

[102] Wikipedia. *Axial tilt*. https://en.wikipedia.org/wiki/Axial_tilt.

[103] Dr. P. Nourian. *Visibility, Sky-View-Factor, Solar Irradiation, and Solar Envelope Configraphix: Graph Theoretical Methods for Design and Analysis of Spatial Configurations View project 3D RASTER View project*. DOI: 10.13140/RG.2.2.17235.81441.

[104] M.E. Tobar et al. "Rotating Resonator-Oscillator Experiments to Test Lorentz Invariance in Electrodynamics". In: *Special Relativity*. Springer Berlin Heidelberg, pp. 416–450. DOI: 10.1007/3-540-34523-x_15.

[105] ArcGIS Pro 3.1. *Tabulate Intersection (Analysis)*. https://pro.arcgis.com/en/pro-app/latest/tool-reference/analysis/tabulate-intersection.htm.

[106] ArcGIS 10.8. *ArcGIS Natural neighbor interpolation*. https://desktop.arcgis.com/en/arcmap/latest/manage-data/terrains/hidden-natural-neighbor-interpolation.htm.

[107] Egged Bus Systems (EBS). *Dienstregeling en routes*. https://www.ebs-ov.nl/reizen/dienstregeling/dienstregeling-en-routes. 2023.

[108] Connexxion (CXX). *Onze routes en diensregeling*. https://www.connexxion.nl/nl/resultaten/dienstregeling. 2023.

A
Conversion of Local Clock Time (LCT) to Julian Date (JD)

The Julian date (JD) is commonly used for solar position calculations, as it provides a standardized way to represent dates and times by considering the necessary celestial and orbital events [101]. The Julian day is a count of days that is continuous and begins from the Julian Period on January 1, 4713 BCE, at 12:00 noon [101]. Calculating the Julian date is essential to continue determining the solar position. The sun position in this work is calculated following the methodology provided by SAM, which is accepted and handed out by the United States Department of Energy's National Renewable Energy Laboratory [42].
The solar altitude, azimuth, zenith, and declination angles indicate the Sun's position, which is defined for each time step and location. Firstly, the time of interest is computed by computing the Julian date (JD). In order to account for leap years, the variable *k* is introduced, where the Equation (A.1) is given as:

$$k = \begin{cases} 1 & \text{if year} \quad \text{if year is easily divisble by 4} \\ 0 & \text{if year} \quad \text{otherwise} \end{cases} \tag{A.1}$$

A year divisible by four is known as a leap year and thus adds one extra day to the calculation. By taking into account factor *k*, the Julian day of the year, noted as *jdoy* of the corresponding year is then calculated using Equation (A.2):

$$jdoy = \begin{cases} day + a & \text{for January and February} \\ day + a + k & \text{for March through December} \end{cases} \tag{A.2}$$

Where *a* calculates the number of days in each month (January=31, February=28, etc.). For example, the experiment conducted by TNO on the 9th of October 2019, which was not a leap year, is known to have a *jdoy* of 282. To consider different time zones, the current decimal time of the day is converted with an offset for the Coordinated Universal Time (UTC). The time is converted using Equation (A.3), to express the value in the correct time stamp.

$$t_{UTC} = hr + \frac{\text{min}}{60} - tz \tag{A.3}$$

Where *hr* refers to the hour, *min* to the minutes and *tz* to the time zone of the location of interest (values which is inputted as 12< tz <12). A correction factor is applied to correct for some time stamps and time zone combinations, where values are $\leq$0 or $\geq$24 (in hours). The correction is given by Equation (A.4).

$$t_{UTC} = \begin{cases} t_{UTC} + 24 & \text{if } t_{UTC} < 0 \\ t_{UTC} - 24 & \text{if } t_{\text{UTC}} > 24 \end{cases} \tag{A.4}$$

The Julian date, JD, can be calculated using Equation (A.5) [42].

$$\text{JD} = 32916.5 + 365(year - 1949) + \frac{year - 1949}{4} + jdoy + \frac{t_{\text{UTC}}}{24} - 51545 \tag{A.5}$$

In this work, the computation of JD is done in MATLAB, where the calendar date can be inputted in the format as: *t = ["YYYY-MM-DD HH:MM:SS"]*. The Julian date utilizes UTC. Through the MATLAB function, ***juliandate(t)***, this timestamp is automatically converted into the Julian date. Finally, the number of days that have elapsed since the 1st of January 2000 (where JD=2451545) can be computed using Equation (A.6):

$$D = JD - 2451545.0 \tag{A.6}$$

After obtaining this value, the location of interest needs to be inputted as the latitude (lat) and longitude (lng) to determine the altitude and azimuth angle of the Sun's position for that exact time and location. The corresponding Equations are given in Section 2.3.1.

B
Solar position calculation

The Solar Position Algorithm (SAM) determines the position of the Sun, where SAM is accepted and handed out by the United States Department of Energy's National Renewable Energy Laboratory [42]. Researchers widely adopt this algorithm to calculate the solar position, where the associated equations are also applied and stated in the Solar Energy book by Smets et al. [40]. After having converted LCT to JD, the sidereal time can be computed. The sidereal time is a measure of time used in astronomy and celestial navigation to determine the position of celestial objects in the sky. In this work, the celestial object of interest is the Sun. The JD is used to determine the Local Mean Sidereal Time (θ_L), which is the sidereal time at the observer's location, and can be used to determine the position of the Sun. The Greenwich Mean Sidereal Time (GMST) is the sidereal time given in hours at the prime meridian. The location of the observer needs to be inputted as the latitude (ϕ_0) and longitude (λ_0), which in this case is the location of the PV module.
For calculating the solar position, limits for ecliptic coordinate variables are indicated. These variables define the position of the PV module on Earth relative to the Sun. They are known as the mean longitude (q), mean anomaly (g), ecliptic longitude (λ_s) and axial tilt of the Earth (δ). The computation of these variables are given below in Equations (B.4), (B.5) and (B.6). To convert the ecliptic coordinates (x) into of equatorial coordinates (a), it is necessary to make sure the equatorial coordinates are within the range of 0° to 360°. For a value *x* with the limits $0° \leq x < 360°$, SAM adjusts the value by dividing *x* by 360° and checking whether the remainder, given as *a*, is less than zero. If so, it adds 360° to the rest:

$$\begin{aligned} a &= x - 360° \,\text{trunc}\left(\frac{x}{360°}\right) \\ x &= \begin{cases} a & \text{if } a \geq 0 \\ a + 360° & \text{if } a < 0 \end{cases} \end{aligned} \tag{B.1}$$

Firstly, the GMST is computed and followed by the computation of the Local Mean Sidereal Time, θ_L. The calculation is done using the following Equations (B.2) and (B.3) [42]:

$$GMST = 18.697374558 + 24.06570982441908 \cdot D + 0.000026 \cdot (\frac{D}{36525})^2 \tag{B.2}$$

The first term, 18.697374558, represents the initial value, which is the difference between the Greenwich meridian and the 1st of January 2000. The second term, $24.06570982441908 \cdot D$ accounts for the Earth's rotation. The last term, $0.000026 \cdot (\frac{D}{36525})^2$, takes into consideration the Earth's long-term variation in rotation rate caused by factors such as small periodic oscillations and gradual changes in the Earth's axis [42]. It serves as a small correction factor to enhance the overall accuracy of the calculation.

$$\theta_L[°] = GMST \cdot 15 + \lambda_0 \tag{B.3}$$

Where λ_0 is the longitude of the point of interest, which in this case is the PV module. The formula converts GMST from hours to degrees, as the Earth rotates 15°/hour. After obtaining the θ_L, the following Equations (B.4) are obtained to determine the intermediate variables, which are used for the computation of the angles respectively.

$$\begin{aligned} g[°] &= 357.529 + 0.98560028 \cdot D \\ q[°] &= 280.459 + 0.98564736 \cdot D \end{aligned} \tag{B.4}$$

Where *g* is the mean anomaly of the Sun, defining the position of the Sun along the orbital plane, and *q* is the mean longitude of the Sun, which is a combination of measures in the equatorial plane and the orbital plane [102]. The axial tilt is the angle between the orbital and equatorial plane (δ). The computation of the axial tilt (δ) is denoted by the following Equation (B.5) [103]:

$$\delta[°] = 23.439 - 0.0000004 \cdot D \tag{B.5}$$

The equatorial and orbital plane and the axial tilt, δ, are visualized in Figure B.1. By inserting the ecliptic

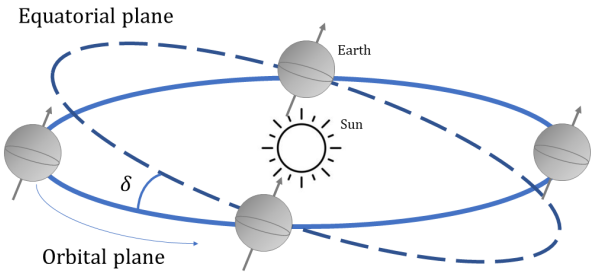

Figure B.1: The Earth revolving around the Sun for a full year, indicating the equatorial plane, orbital plane and axial tilt (δ), after [104].

coordinate variables, g and q, into the following Equation (B.6), the longitude of the Sun in elliptic coordinates (λ_s) can be found:

$$\lambda_s[^\circ] = q + 1.915sin(g) + 0.020sin(2g) \tag{B.6}$$

Where λ_s is the ecliptic longitude of the Sun. The variables q, g and λ_s range from 0° to 360°.

Finally, using the solar position variables determined in this Appendix, the solar altitude and azimuth angles, given in Equations (B.7) and (B.8), can be determined [40].

$$a_S = \sin^{-1}\left(\cos(\phi_0)\cdot\cos\left(\theta_L\right)\cdot\cos\left(\lambda_s\right) + \left(\cos(\phi_0)\cdot\sin\left(\theta_L\right)\cdot\cos(\delta) + \sin(\phi_0)\cdot\sin(\delta)\right)\cdot\sin\left(\lambda_s\right)\right) \tag{B.7}$$

$$A_S = \tan^{-1}\left(\frac{-\sin\left(\theta_L\right)\cdot\cos\left(\lambda_s\right) + \cos\left(\theta_L\right)\cdot\cos(\delta)\cdot\sin\left(\lambda_s\right)}{-\sin(\phi_0)\cdot\cos\left(\theta_L\right)\cdot\cos\left(\lambda_s\right) - \left(\sin(\phi_0)\cdot\sin\left(\theta_L\right)\cdot\cos(\delta) - \cos(\phi_0)\cdot\sin(\delta)\right)\cdot\sin\left(\lambda_s\right)}\right) \tag{B.8}$$

C
Perez component calculations

The empirical functions given by Perez [47], in Equation (2.9) and (2.10) in Section 2.3.3, include the factors F1 and F2 which are known as the Perez coefficients. As mentioned in Section 2.3.3, this work does not include the horizon brightening component (G_{hor}). Therefore the factor F2, which is only included in G_{hor}, will not be discussed in further detail. The Perez coefficient F1, which is used for calculating the isotropic (G_{iso}) and circumsolar irradiance component G_{cir}, is determined by the following set of Equations:

$$F_1 = \max\left[0, \left(f_{11} + f_{12}(\frac{\mathsf{DHI} \times \mathsf{AM_a}}{E_\mathsf{a}}) + \frac{\pi\theta_z}{180^\circ} f_{13}\right)\right] \tag{C.1}$$

$$E_\mathsf{a} = E_{sc} \times \left(\frac{R_{av}}{R}\right)^2 \tag{C.2}$$

$$\left(\frac{R_{av}}{R}\right)^2 = (1.00011 + 0.034221\cos(b) + 0.00128\sin(b) + 0.000719\cos(2b) + 0.000077\sin(2b)) \tag{C.3}$$

$$b = 2\pi\frac{\mathsf{DOY}}{365} \tag{C.4}$$

In the given context, the solar zenith angle is denoted as θ_Z, the extraterrestrial radiation as E_a, and the solar constant as E_{sc} (1367 Wm^{-2}). R_{av}/R is the ratio for the distance between the Sun and the Earth at a specific time, and DOY is the day of the year [47]. The constant κ, which is used to characterize the distribution of circumsolar radiation, takes a value of 1.041 when angles are in radians or 5.535 $\cdot 10^{-6}$ when angles are in degrees [47]. "AM_a represents the absolute air mass, and ϵ is a parameter linked to the sky clearness index, determining the bins for categorizing Perez coefficients. Using Equation (C.5), the clearness (ϵ) is calculated and used for defining the bin for the f coefficients, given in Table C.1.

$$\varepsilon = \frac{\kappa\theta_Z^3 + (\mathsf{DHI} + \mathsf{DNI})/\mathsf{DHI}}{1 + \kappa\theta_Z^3} \tag{C.5}$$

The different bins, ranging from 1 to 8, are used to determine the Perez coefficients (f11, f12, f13, f21, f22 and f23). These coefficients are used as an input for determining the irradiance and are given in Table C.2.

bin	**1 Overcast**	**2**	**3**	**4**	**5**	**6**	**7**	**8 Clear**
Lower Bound	1	1.065	1.230	1.500	1.950	2.800	4.500	6.200
Upper Bound	1.065	1.230	1.500	1.950	2.800	4.500	6.200	—

Table C.1: Sky clearness categories for each bin [47].

bin	**f11**	**f12**	**f13**	**f21**	**f22**	**f23**
1	-0.008	0.588	-0.062	-0.06	0.072	-0.022
2	0.13	0.683	-0.151	-0.019	0.066	-0.029
3	0.33	0.487	-0.221	0.055	-0.064	-0.026
4	0.568	0.187	-0.295	0.109	-0.152	-0.014
5	0.873	-0.392	-0.362	0.226	-0.462	0.001
6	1.132	-1.237	-0.412	0.288	-0.823	0.056
7	1.06	-1.6	-0.359	0.264	-1.127	0.131
8	0.678	-0.327	-0.25	0.156	-1.377	0.251

Table C.2: Perez coefficients for irradiance modelling [47].

D
ArcGIS workflow manual

Spatial road survey points
Spatial road survey points are generated when simulating the incident irradiance for a specific route. The distance between each point is chosen and can be changed to meet the desired resolution. Within ArcGIS Pro, the 'Data Management Tools' should be licensed. The following steps are required to obtain road survey points:

1. The route of interest needs to be quantified in terms of a 'polyline', which in this work is done by selecting this polyline from a road database or other dataset. For all bus routes in The Netherlands, Geoportal University of Groningen has converted roadway data into an ArcGIS map for spatial analysis [88]. This dataset used for both case studies in this work.
2. Then followed by application of the Geo-processing tool, found in the Data Management Tools → **Generate Points along Lines**. The necessary inputs for this tool are:
   (a) Input features: polyline
   (b) Output feature class: given name
   (c) Point placement: by distance
   (d) Distance: [desired spatial distancing] in *meters*
3. The XY-coordinates for the generated spatial points can then be determined using the tool Data Management Tools → **Add XY coordinates**.
4. The generated coordinates can be displayed in the *Attribute Table*, and all the items can be selected and by copying the multiple coordinates to an Excel sheet, they can be used as an input for the horizon scanning algorithm.

The reversed approach inserts existing points in ArcGIS instead of creating points. Logged GPS coordinates can be converted into road survey points for this approach. For this application, the tool Data Management Tools → **XY Table To Point** is required.

Land use map intersection & buffer creation
Using the BBG 2017 dataset, as referred to in Section 3.6, the overlay and intersection of maps are necessary. A buffer is generated for a road survey point, using the same radius as when the horizon of that point was scanned for the skyline profile. By using the feature **'Buffer'** in ArcGIS, a circular buffer is created. In this work, the radius of the buffer is 100 meters to align with the horizon scanning inputs. Using the '**Spatial Joint - Largest Overlap**' tool in ArcGIS, the buffer around a road survey point is joined with one terrain type feature. It is linked with the terrain feature with the most significant area within the buffer intersection. A higher accuracy is obtained by finding more overlaps in the overlaid spatial joints. For this case, buffer layer (generated with a radius of 100 meters) and BBG map are overlaid and intersected for which the parameter 'Intersect many layers' needs to be chosen. The result can be visualized using ArcGIS, where the main terrain types for the different bus routes of Amsterdam are shown in Figure 5.3 in Section 5.1.2.

Impact zone distribution within a road survey point buffer
Each road survey point contains a different surrounding environment. The topographical BBG map consists of polygons, where each polygon is indicated by one of the terrain type codes (given in Section 3.6). This map is overlayed with the 100-meter buffers around each road survey point. Each road survey point contains a SVF value, which has been obtained using the modelling approach presented in this work. To find what part a specific terrain type constitutes within the entire buffer which is enclosed, the **'Tabulate Intersection (Analysis)'** tool is used. Within ArcGIS Pro, this intersection tool can be found in the Statistical toolset → ***Tabulate Intersection (Analysis)*** [105]. This gives a percentage of how much of a terrain type is intersected by the buffer. Figure D.1 illustrates how this tool works, where the 'zone' refers to each buffer with a radius of 100 meters, and the' class features' refer to the land use (BBG) map including different polygons classified in terrain types [105]. The intersection results in an area and percentage of a certain terrain, which is covered

in the polygon. The percentage gives the share of a specific terrain area within the buffer. The outcome is a database of different percentages of terrains with their corresponding SVF value. Figure D.1 shows how terrain type polygons (class features) within a buffer (zone) can be extracted to a database for analysis.

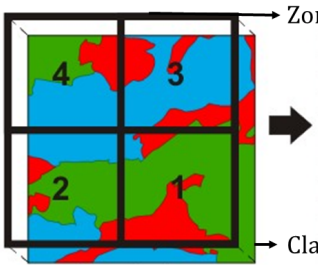

Output

Zone	Color	Area	Percentage (%)
4	Blue	5.5	59.3
4	Green	2.0	21.5
4	Red	1.8	19.1

Figure D.1: Illustration of the ArcGIS Tabulate Intersect tool, where 'zone' refers to each buffer, and 'class features' refers to the land use (BBG) map, including different colors which represent terrain types, after [105].

This database is used for further analysis in the case study of the bus routes of Amsterdam. By comparing and analyzing the fraction of a specific terrain, such as a building terrain, and their corresponding SVF value, it can be determined whether it is possible to give a proxy of the SVF using this topographical map.
From this, a road survey point with corresponding SVF value is divided into multiple terrain types. In summary, using the 'intersect many layers' tool, a road survey point with a SVF value of 0.69 consists of 70% built terrain, 20% recreational terrain, and 10% agricultural terrain. This is the used approach in this work.

Interpolation to visualize irradiance on roads
To visualize the incident irradiance for a specific route, the following steps need to be conducted in ArcGIS Pro. Within the ArcGIS Pro software, the licenses' spatial analyst' and '3D analyst' are required. As a first step, the irradiance (W/m^2) or irradiation (Wh/m^2) values for the individual road survey points need to be interpolated to visualize the route. For this, the following steps are required:

1. A data file (in the format of a .csv, .xlsx or .txt file, includes the calculated irradiance values for each individual XY-coordinate. Where the necessary inputs in this data file are: *X-POINT, Y-POINT, and Irradiance*.
2. By loading this data into the ArcGIS environment, the XY-points can be added to the map, by right-clicking "Display XY Data") (X- & Y-point).
3. To represent the irradiance values as interpolated values, use ArcToolbox → 3D Analyst Tools → ***Natural Neighbour***. Using an algorithm, this interpolation tool finds the subset of input samples closest to the search point and weights the samples according to their relative areas [106]. The advantage of this interpolation tool is that it produces a smooth interpolation surface where the input variables gradually change between the data points [106]. However, the interpolation between the road survey points leads to inaccuracy. Therefore, it is necessary to choose a high density of points to filter out any unknowns. Given that for a high point density, the surrounding obstructions gradually change during a driven route which makes the interpolation between the irradiance values more accurate. The following input parameters for the Natural Neighbour tool are:

   (a) Input point features: the dataset of coordinates with corresponding annual irradiance values
   (b) Z value field: annual irradiance
   (c) Output raster: given name

   Where the output cell size can be kept to the default.
4. By running this interpolation, a raster map of the interpolated annual irradiance values will be shown.
5. To extract the interpolated values and represent them as the specified roads, the raster data can be extracted for corresponding feature mask data, which are roads. By using the ArcToolbox → Spatial Analyst tool → ***Extract by Mask*** tool, with the following input parameters:

   (a) Input raster: ArcMap with the given interpolated irradiance values
   (b) Feature mask data: road polylines

6. By running this function, the interpolated irradiance values will be shown for the route segments, given the range of irradiance values. The interpolated values for all the bus routes are visualized in Figure 6.8 in Section 6.2.

E
Algemene Hoogtekaart Nederland (AHN)

Figure E.1: AHN3 map of The Netherlands indicating the division into different map sheets [73].

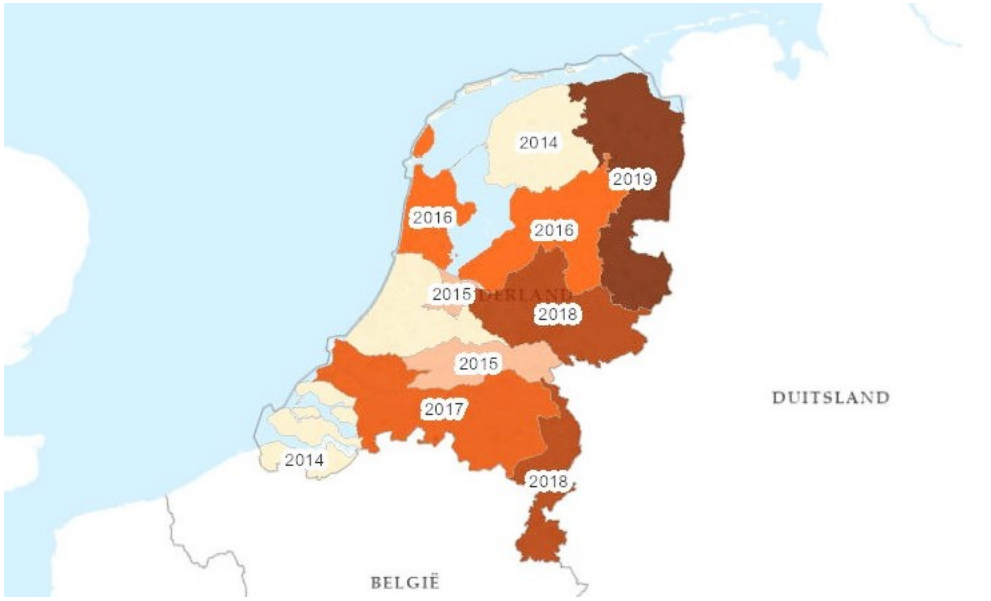

Figure E.2: AHN3 map of The Netherlands indicating the division of the different years in which LiDAR data is collected [73].

F
Clear sky irradiance model

The Ineichen-Perez clear sky irradiance model empirically determines the GHI, DNI and DHI for a specific location and time. This model is obtained through the usage of PVlib, which is an open-source Python library used for PV modelling and analysis under different conditions [54]. Various tools and models are available in the library, including clear sky irradiance models. Each model requires other input datasets and differs in accuracy due to its characteristics and assumptions. In PVlib-python, the two most common clear sky irradiance models are the Ineichen-Perez and REST2 models. The Ineichen-Perez model is well-known for its adaptability and accuracy in different situations [54]. Table F.1 presents the input parameters for calculating the clear sky irradiance using the Ineichen-Perez model.

Inputs in Python	Description	Unit
latitude	latitude in decimal degrees, ranging from -90° (south pole) to +90° (north pole), with the equator at 0°	*dd*
longitude	longitude in decimal degrees, ranging from -180° (west) to +180° (east). The prime meridian, at GMT/UTC, is assigned 0° longitude.	*dd*
tz	time zone, which converts it to UTC from a place and time of interest. In this work, the time zone for the Netherlands is used which is indicated as 'Europe/Amsterdam'	-
altitude	altitude/elevation above sea level	*m*
name	providing the inputs for the inputs given above, in the format: name = latitude, longitude, 'tz', altitude, 'city'	-

Table F.1: Inputs for the Ineichen-Perez Clear Sky irradiance model [54].

The definition in Python to calculate the clear sky irradiance using Ineichen-Perez is given by:
`ineichen = pvlib.clearsky.ineichen(apparent_zenith, airmass, linke_turbidity, altitude, dni_extra).`
Through a for-loop in Python, the clear sky calculation is performed for every time stamp inputted in an Excel sheet. This iteration between different timestamps is important as the frequency of measured or simulated irradiance values can differ.
The clear sky irradiance, applying the Ineichen-Perez model, is determined for the static pyranometer validation study as well as Bus 40 case study. This empirical modelling approach can easily be adjusted for a specific location and time. The computed clear sky irradiance is saved in an Excel file where the values for GHI, DNI and DHI are given for the chosen timestamp. In addition, the clear sky irradiance values are plotted in a graph for the indicated time range. For illustrative purposes, the decomposition of the clear sky irradiance is obtained for the static validation location in Section 4.4 and presented in Figure F.1 for the 11^{th} of October 2015.

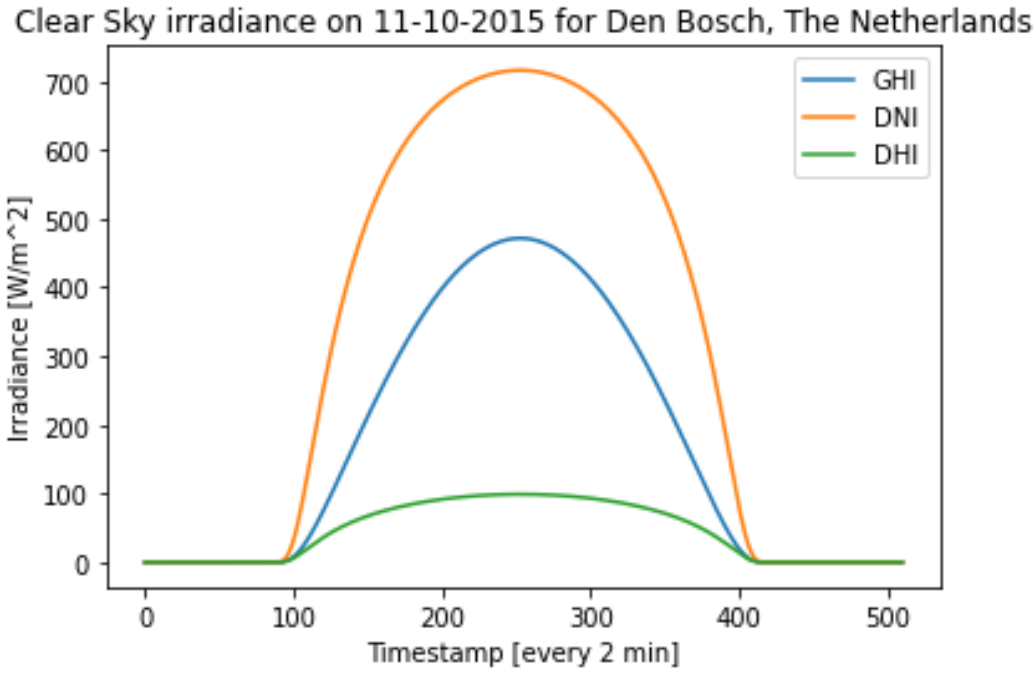

Figure F.1: The clear sky irradiance simulated for the 11th of October for the static pyranometer in Den Bosch, The Netherlands, through the usage of PVlib [54].

G
Horizon scanner

In the thesis of Keijzer [65], the horizon scanning approach was initiated, using the created geometry calculations and the SVF calculation equations by Steyn [57]. The improvement made regarding the existing model is extracting height data using a Web Coverage Service (WCS) instead of manually withdrawing large AHN files. The extraction of the DSM data using WCS is explained in Section 3.4.1 in Chapter 3. In this Appendix, in Section G.1, the variable settings using WCS are presented and explained in more detail. The working principle of the horizon scanning technique for the code in Python is described in Section G.2.

G.1. Web Coverage Service (WCS) request

The Web Coverage Service (WCS) enables direct extraction of DSM data through a URL link, which stores configuration data in a structured and standardized format [77]. As a first step, the **OWSlib** package needs to be installed in Python using the command: ”pip install OWSLib” in the Command Prompt. After the installation of the **OWSlib** library in Python, the GetCoverage request can be executed to extract the bounded part of the height map for the indicated GPS coordinates [77]. This workflow is performed for multiple GPS coordinates situated on a road. There are various sub-settings for obtaining the preferred GetCoverage response. Table G.1 displays the URL for extracting the data and the necessary sub-settings for this work.

url = ’https://service.pdok.nl/rws/ahn3/wcs/v1_0?request=getcapabilities&service=wcs’

URL component	**Output**	**Description**
Serivce	WCS	Service name
Version	1.0.0	Requests protocol version
Request	GetCoverage	Name of the request in order to return a response
Identifier	ahn3_05m_DSM	Specifies the layer identifier which is retrieved, where options are DSM and DTM and the resolution is 0.5 and 5 meters.
Format	GEOTIFF_FLOAT32	The format of the output is given in a
Coordinate Reference System (CRS)	EPSG:4326	Geographic coordinate system given in decimal degrees
Bounding box (bbox) [x = longitude, y = latitude]	x-(radius), y-(radius) x+(radius), y+(radius)	A bounding box is created around each specified set of GPS coordinates, where the outer edges of this box is the radius of the area to be scanned
Size	WIDTH = radius*2 HEIGHT = radius*2	The size of this bounding box is a square with both the width and length having a size of ”radius*2”

Table G.1: The WCS GetCoverage request URL and settings for obtaining AHN3 DSM data from PDOK [73].

By inserting the sub-settings presented in Table G.1, the output is in the format of a clipped TIF file (image file) of the bounded area around the specified GPS coordinate. This clipped TIF file is inputted in the horizon scanner code. The workflow is repeated for each set of coordinates and can be done in one run without manual operations in between.

G.2. Horizon scanner code explanation

After obtaining the clipped TIF file, it is used as an input for the horizon scanner. The Digital Surface Model (DSM) image (in the format of a TIF file) is scanned to read and convert relevant height data into a *NumPy* array. Pixel values >10,000 (10E3) are removed as they are assumed to be errors. These error pixels get a value of 0 assigned and are, therefore, not considered in the scanning of the horizon.

The code then computes the horizontal and vertical angles of each pixel relative to a point p (x_p, y_p) at the centre of the sky dome, as well as the distance of each pixel from the centre point. The angles are rounded to the nearest degree and stored in the *azi_round* array. The vertical angles are stored in the *alti* array. Next, the code initializes empty arrays to store the horizon altitude and distance values. The amount of slices, given as n, determines the number of horizon angles to be scanned, which is given by the Equation: $\Delta\theta = \frac{360}{n}$. In this case, $\Delta\theta$ is the angle for which each 'slice' scans the vertical alitude angles. In this work, there are 360 slices (=n), indicating an angular resolution of $\Delta\theta = 1°$. The geometrical formula which scans each azimuth slice, $\Delta\theta$, to determine the maximum altitude angle at that particular azimuth, $a_{skyline}$, is given in Equation (G.1).

$$a_{skyline} = \tan^{-1}\left(\frac{h_{\text{obs}} - h_{\text{offset}}}{r_{\text{obs}}}\right) \tag{G.1}$$

Where h_{obs} is the maximum height of the obstruction in that slice, h_{offset}, is the height offset of the vehicle and r_{obs} is the distance from the road survey point to the obstruction.

As a next step, raw horizon arrays are generated. This is done by iterating over all the pixels in the image and checking if they are within a minimum radius from the defined spatial point p. If a pixel is within the minimum radius (*r_max*), its altitude and distance values are compared to the existing values at the corresponding azimuth index in the horizon arrays. Suppose the pixel altitude is higher than the existing value. In that case, the new and highest value is stored in the *horizon_alti_raw* array. The highest value of an obstruction is used to calculated the corresponding $a_{skyline}$ for that particular azimuth slice.

The raw horizon arrays are smoothed to remove any errors or extremely large values in the LiDAR data. The smoothing is done by using a simple algorithm that applies a correction factor to each azimuth index based on the distance to the nearest neighbouring pixel. This is referred to as the **'close wall effect'**. The close wall effect indicates the example of a slice situated between two data points and not seeing any data points in the grid. Therefore, no value can be scanned or seen, which results in an error. In the thesis of Keijzer [65], the 'close wall effect' was initiated and generates an imaginary wall by assigning the same values for the slices in between the grid data points to prevent an error or 0 as an outcome for this azimuth slice. To overcome this error due to a limited grid distance, slices to the wall data point will be allocated the same altitude as the slice holding the wall data to counteract this effect. An illustrative example of this approach is displayed in Figure G.1, where the altitude of slice 45 (containing the wall data) is extended to all slices between 41 and 49.

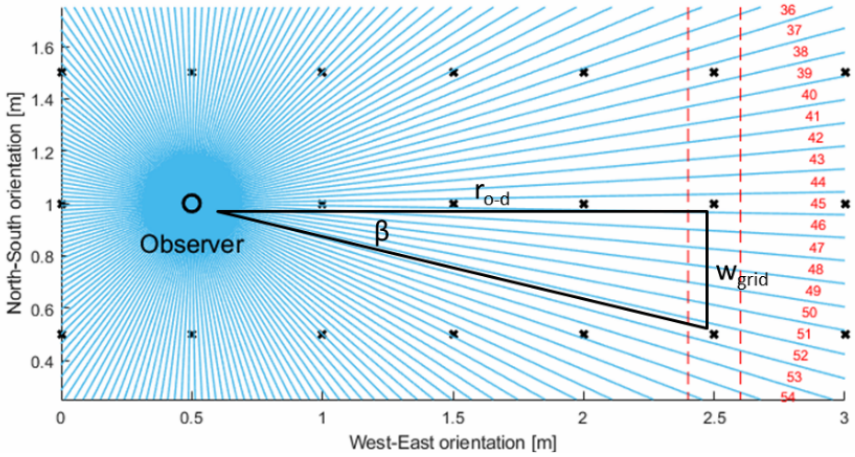

Figure G.1: An illustrative example of a slice not enclosing a height data point, where the solution is the red, dashed line illustrating the close wall effect using the angle correction range (ACR) [65].

The Angle Correction Range (ARC) determines the number of slices on either side of a grid data point that should be given the same value. The ARC equation is given as:

$$ACR = ROUND(\frac{\beta}{\Delta\theta \cdot 2}) = ROUND(\frac{tan^{-1}(w_{grid}/r_{o-d})}{(360/n) \cdot 2}) \tag{G.2}$$

The ACR is essential for height maps with larger grid distances, as a small angular step size has a high chance of filtering out data points. In addition, the larger the value of *n* (indicating the number of slices), the more this effect will occur as well.

The smoothing is controlled by the *smooth_amp* parameter, which determines the strength of the smoothing. The values in the *horizon_alti_raw* array are smoothed and stored in the *horizon_alti_smooth* array.
After having obtained the 2D array, it is converted and reshaped into a 1D array in the *horizon_alti_smooth* array, where it is converted from radians into degrees. The final section of the code creates an *output list* with two different arrays, the azimuth horizon and altitude horizon (*horizon_alti_smooth* array). Where each value in the first array corresponds with the other matter in the second array, by way of example, *azi_4* corresponds to *alti_4*. These two arrays containing the obtained horizon scanner values can be plotted against each other to visually represent the skyline at the XY-coordinate.

As the horizon scanning principle is now established for an individual XY-coordinate (using a singular input of latitude and longitude), a panda data frame code creates a repeating algorithm which continues the operation for a set of coordinates (for a specific route). By linking to an Excel sheet, in this work named $'Coordinates - multiplesheet.xlsx'$, essential inputs such as the longitude, latitude, and coordinate identification can be easily extracted.

H
Verification of the Web Coverage Service (WCS)

The horizon scanning algorithm, explained in Section 3.4.1, retrieves data directly using the Web Coverage Service (WCS) followed by performing necessary scanning calculations in a step-wise manner for a 90-degree altitude and 360-degree azimuth. The scanning algorithm is in the format of a code, which obtains LiDAR height data directly using the WCS server. As the height data is contained in a 0.5x0.5 m^2 grid, it cannot accurately determine if the scanning procedure is correctly executed. Therefore, a verification has been performed using Google Maps to confirm the alignment of a few points. An example of such verification is shown below.
A first data point with GPS coordinates (51.10534, 5.874985) in the residential area of Echt, The Netherlands, is chosen and analysed in ArcGIS. By visualising a 100-meter radius buffer around the coordinate of interest, the surrounding obstructions within this buffer can be analysed. This is visually shown in Figure H.1 in the left image. By using the "Distance & Direction" tool in ArcGIS, the length and angle to a visible obstruction can be determined. In this example, the starting point is in the north direction, where the azimuth is known as 0°. A visible obstruction, which is a townhouse, is visible at a distance of 6 meters for an azimuth of 287°. The distance and direction of this obstruction are presented in the right image in Figure H.1.

(1) Scanning radius of 100m

(2) Distance and direction to a visible obstruction

Figure H.1: The verification of the horizon scanning approach using an example data point with GPS coordinates (51.10534, 5.874985) in Echt, The Netherlands, where ArcGIS is used to (1) scan the surroundings using a radius of 100 meters and (2) obtain the distance and direction to a visible obstruction.

The next step for verification is an estimate of the height of the house in order to determine what the maximum altitude angle will be. Given the geometry calculation in Equation (H.1), the maximum altitude angle in this case can be calculated. The geometry for this Equation is illustrated in H.2.

$$a_{skyline} = \tan^{-1}\left(\frac{h_{\text{obs}} - h_{\text{offset}}}{r_{\text{obs}}}\right) \tag{H.1}$$

The height of the obstruction, given as h_{obs}, in this example, a townhouse with 2 floors and a pointed roof with a chimney, is estimated at 8 meters. The distance from the calculation point to the obstruction is measured 6 meters, r_{obs}, and the height offset of the vehicle is 1.5 metres, h_{offset}. Performing this calculation, the maximum altitude angle at an azimuth of 287° is 49.4°. By looking into the skyline generated by the horizon scanner, the maximum altitude is 59°. The error between these values is 19.4%, which is relatively large. By looking into different causes of this deviation, it is concluded that a large tree is present in front of the house.

The tree is shown in Figure H.3, where it has been derived from a Google Street View image. Due to the changing environmental conditions of vegetation, the irregularity of the tree can be reflected in the generated skyline. This is known as the LiDAR discrepancy.

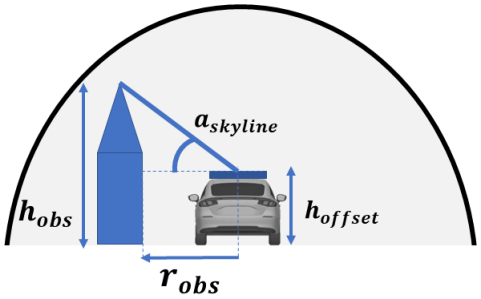

Figure H.2: Horizon scanning geometry relation.

Figure H.3: Google Street View image, where a (seasonally) varying obstruction is shown, a tree, in front of a house in Echt, The Netherlands.

Continuing the verification with obstructions which do not differ seasonally, a similar calculation is performed for a different XY-coordinate on the road. Figure H.4 shows the distance and direction to the house, which has, in contrast to the previous data point, no trees or other differing objects in front. The examination of spaces to and from this obstruction is conducted using ArcGIS. It reveals that at 285°, measured from 0° north, there is an approximate distance of 8 meters to the house. Using the horizon scanning geometry relation, given in Equation (G.1), the altitude of the obstruction at an azimuth of 285 degrees can be determined.

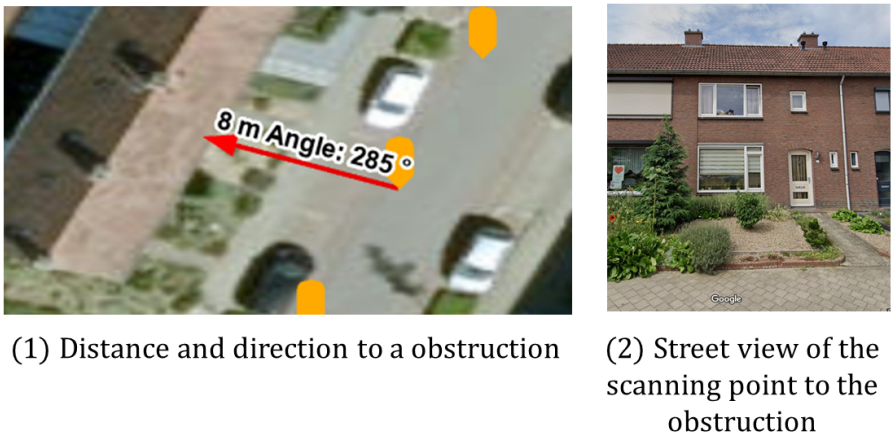

(1) Distance and direction to a obstruction

(2) Street view of the scanning point to the obstruction

Figure H.4: (1) Distance and direction from the example data point to a nearby obstruction, (2) Point of view from the data point to the obstruction using Google Street View.

$$a_{skyline} = \tan^{-1}\left(\frac{8-1.5}{8}\right) = 39.1° \tag{H.2}$$

This calculation results in an altitude of approximately 39.1°. To verify this geometry calculation and the horizon scanning method using a Web Coverage Service (WCS), the generated skyline profile is checked to see if the maximum generated altitude aligns with this calculation. At an azimuth of 285 degrees, the maximum generated altitude is 40 degrees. This is shown in Figure H.5. The percent error between the two values is 2.25%, which is relatively accurate as the small differences are within the discrete LiDAR grid data and rounded altitude height angle in the skyline profile.
In summary, the difference is mainly due to obstructions which change seasonally, such as trees, or differences in the retrieval year of the data sets which are compared together. Overall, the skyline profile aligns with the surroundings for other points. Therefore, the horizon scanning method and extraction of DSM data using a WCS are verified.

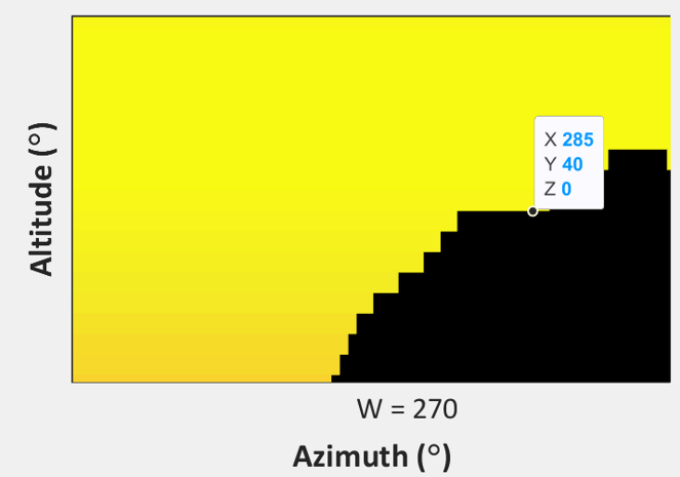

Figure H.5: Clipped skyline representation to identify the maximum altitude (40°) for an azimuth of 285°, for verification of the horizon scanning approach.

I

Measurement uncertainty calculation

The uncertainties of measurements from the dynamic validation dataset have been presented in this Appendix. The uncertainties and errors have been calculated and combined following the procedures given by Cook in the 'Assessment of Uncertainties of Measurement for calibration and testing Laboratories' book, as well as the PhD thesis work performed by Carr [83, 85].

I.1. Sensor specifications

The specifications of the sensors for the dynamic VITS validation and static pyranometer validation are given in this Section.

I.1.1. Dynamic validation dataset specifications

The measurement uncertainty values of the irradiance sensor (Si-V-10C-T), the data acquisitions logger (IMC CANSAS SC18), and the GPS receiver sensor (Garmin GPS 18x 5Hz™) are presented in Table I.1 [84, 97, 86].

	Measurement uncertainty	
Irradiance sensor (Si-V-10C-T)	Temperature dependence Non-linearity Measurement uncertainty Factory calibration error	+/- 0.4% +/- 0.1% +/- 2.5% of reading +/- 0.75%
Data acquisition monitoring system (IMC CANSAS SC18)	Offset (current/voltage)	+/- 0.02%
GPS receiver (Garmin GPS 18x 5Hz™)	Accuracy	<15 meters, 95% typical

Table I.1: Measurement uncertainties from the irradiance sensor, data logger and GPS specification sheets [84, 86, 97], for the dynamic dataset.

I.1.2. Static validation dataset specifications

For the static pyranometer installed in Den Bosch, The Netherlands, the pyranometer EKO MS-802 is used to measure irradiance. The pyranometer (EKO MS-802) has the following specifications [98]:

- Temperature dependence: $\pm$ 1%
- Non-linearity: $\pm$ 0.2%

The measurement uncertainty and factory calibration error are not presented in the technical specification sheets of the pyranometer [98]. Furthermore, the data logger used in the static dataset is unknown. Therefore, similar specifications for the data logger used in the dynamic VITS experiment (IMC CANSAS SC18) are assumed.

I.2. Determination of the combined uncertainty

The limits and uncertainties of the sensors are quantified in percentages in the specification sheets. However, the value of the measurand is still likely to be anywhere in the stated range [83]. This represents a *rectangular distribution*, and the standard deviation formula for this distribution quantifies the standard uncertainty (u_i), which is given as:

$$u_i = \frac{a}{\sqrt{3}}$$

Where a is the semi-range of the limits of the uncertainty component. The rectangular distribution is used if there is no knowledge on what the dispersion or distribution of values may be. As this is unknown for the

measured datasets, this distribution type is used for determining the u_i [83]. After having obtained the standard uncertainty for the sensor components, the combined uncertainty can be estimated [83].
The combined uncertainty (u_c) calculation consists of a sensitivity coefficient, c_i, and standard uncertainty of each input component, u_i. The sensitivity coefficient is set to 1 and used as a baseline, as this comparison is focused on the changes and uncertainties that come across with the measurements [85]. The formula for determining the combined standard uncertainty is shown in Equation (I.1). This formula applies only if the parameters are independent of each other. The independence depends on the specific characteristics and how they relate. In this case, the non-linearity and factory calibration error are often treated as independent sources of uncertainty [83]. Furthermore, the measurement uncertainty is based on the sensor's reading, which does not rely on the measured value. In this uncertainty analysis, the components are generally considered and assumed as independent and, therefore, the combined uncertainty (u_c) using these components can be determined.

$$u_c = \sqrt{\sum_{1}^{i} [c_i u_i]^2} \tag{I.1}$$

The error analysis for the dynamic validation dataset is summarized in Table I.2, where the computation of the combined standard uncertainty for the dynamic irradiance sensor and data logger is given for the validation route.

Component	**Units**	**a**	**u_i**	**c_i**	**(c_i*u_i)^2**
Si-V-10C-T Temperature dependence	%	0.4	0.23	1	0.0529
Si-V-10C-T Non-linearity	%	0.1	0.06	1	0.0036
Si-V-10C-T Measurement uncertainty	%	2.5	1.44	1	2.0736
Si-V-10C-T Factory calibration error	%	0.75	0.43	1	0.1849
IMC CANSAS SC18 Accuracy	%	0.02	0.01	1	0.0001
Total summation					2.3151
Combined standard uncertainty (u_i)					1.5215
Rounded u_i					**1.52%**

Table I.2: Error analysis and the combined standard uncertainty computation for the irradiance sensor and data logger used in the dynamic VITS data, using the procedures given by R.R. Cook [83].

This Table calculates a combined standard uncertainty (u_c) of **1.52%** for the irradiance sensor and data logger in the measured VITS data and does not include the GPS measurement accuracy, which is $\leq$15 meters for 95% typical, due to potential obstructions blocking the GPS signal causing random position errors. Such GPS offsets can result in significant differences in the obtained SVF using the horizon scanner. To obtain the standard uncertainty for the GPS sensor, the following formula can be applied [83]:

$$u_i = \frac{U_{95}}{2}$$

Where U_{95} is the expanded uncertainty at a 95% confidence limit and the factor 2 may be used when the value of U_{95} is given, which is the case for the GPS sensor accuracy [83]. This results in 7.5 meters. The exact GPS offset is unknown for the validation route, as presented in Section 4.3.3. The numerical inaccuracy for GPS offsets is therefore beyond the scope of this work.
Finally, The same procedure is applied for the combined standard uncertainty for the static pyranometer data. Using the presented specification values and similar conditions for c_i, the combined standard uncertainty (u_c) is calculated as **0.59%** for the irradiance sensor and data logger in the static pyranometer data. The difference in values is due to the usage of different irradiance sensors.

J
Characteristics and results for all bus routes of Amsterdam

The 27 bus lines of Amsterdam, with different bus routes, route lengths, durations, and different public transport operators, are shown in Table J.1. The bus operators are presented in the acronyms: CXX is Connexxion, EBS is Egged Bus Systems, and GVB is Gemeente Vervoer Bedrijf [91, 107, 108].
This Table J.1 states the characteristics and results. The average SVF, in the column, stated as 'SVF [-],' is determined for each bus route, and the corresponding annual average irradiation, presented in the column as 'Irradiation' in [kWh/m^2/year], is calculated for each route. The irradiation value is based on the irradiance potential, which would be incident on the bus if it was driving for a full year. These calculated values give an estimate of what the annual PV potential for the bus route is.

Bus route *(St = Station)	Bus operator	Bus line	Bus length [km]	Bus duration [hour:min]	SVF [-]	Irradiation [kWh/m2/yr]
KNSM Eiland - St. Zuid	GVB	65	8.6	00:39	0.73	742.02
St. Holendrecht - St. Bijlmer ArenA	GVB	47	9.1	00:28	0.85	886.76
St. Sloterdijk - St. Zuid	GVB	15	6.2	00:23	0.71	718.61
Slotervaart - Centraal St.	GVB	18	9.5	00:29	0.73	730.56
Amstelstation - Muiderpoortstation	GVB	40	5.7	00:15	0.80	836.42
Gelderlandplein - Zuidas	GVB	461	1.3	00:06	0.62	711.64
St. Holendrecht - Muiderpoortstation	GVB	41	13.3	00:40	0.79	835.08
Amsterdam Noord - Purmerend	EBS	301	11.8	00:23	0.94	975.13
Amstelstation - St. Noord	GVB	37	10	00:27	0.69	717.57
St. Sloterdijk - Muiderpoortstation	GVB	22	10.8	00:34	0.76	791.08
Amsterdam CS - Purmerend	EBS	306	21.7	00:28	0.89	923.11
Amsterdam Noord - Marken	EBS	315	20	00:28	0.93	969.26
Amsterdam Sloterdijk - Purmerend	EBS	309	20.8	00:42	0.86	902.04
Amsterdam Noord - Landsmeer	EBS	319	3.5	00:10	0.86	883.24
Olof Palmeplein - Molenwijk	GVB	35	9.9	00:27	0.81	858.63
Amsterdam ZO - Purmerend	EBS	375	22.9	00:50	0.91	946.36
Aalsmeer - Amsterdam Bijlmer ArenA	CXX	171	16.8		0.87	896.43
St. Sloterdijk - Buikslotermeerplein	GVB	36	11.8	00:26	0.86	887.77
Centraal Station - Geuzenveld	GVB	21	10.9	00:23	0.69	723.77
Abcoude - Amsterdam CS	CXX	612	14.2	00:48	0.86	901.37
Amsterdam CS - Zaandam Station	CXX	394	14.7	00:36	0.80	844.85
Olof Palmeplein - Noorderpark	GVB	34	6.3	00:20	0.78	834.81
Gelderlandplein O - De Boelelaan/ Klencke	GVB	464	1	00:05	0.11	116.10
Station Noord - Buiksloterham	GVB	38	7.5	00:25	0.80	841.41
Centraal Station - Borneo Eiland	GVB	43	4.5	00:14	0.72	685.53
Centraal Station - Houthavens	GVB	48	3.1	00:10	0.79	824.96
St. Sloterdijk - Zaandam ZMC	CXX	395	9.8	0:28	0.82	864.93

Table J.1: Summary of characteristics and annual average irradiation results for the 27 bus routes of Amsterdam, given as a color scale [91, 107, 108].